Title
Climate, clouds, and convection on Earth and Titan

Author
Spaulding-Astudillo, Francisco Eduardo

Publication Date
2023

Peer reviewed|Thesis/dissertation

UNIVERSITY OF CALIFORNIA

Los Angeles

Climate, clouds, and convection on Earth and Titan

A dissertation submitted in partial satisfaction
of the requirements for the degree
Doctor of Philosophy in Geophysics and Space Physics

by

Francisco Eduardo Spaulding-Astudillo

2023

ABSTRACT OF THE DISSERTATION

Climate, clouds, and convection
on Earth and Titan

by

Francisco Eduardo Spaulding-Astudillo
Doctor of Philosophy in Geophysics and Space Physics
University of California, Los Angeles, 2023
Professor Jonathan L. Mitchell, Chair

The planets and moons in the solar system present a unique opportunity for enriching our understanding of Earth. The remarkable diversity of atmospheric compositions, dynamics, and weather patterns requires us to move beyond Earth-centric paradigms and search for more general theories that can explain the similarities and differences between them. In this work, Saturn's moon Titan is chosen as the point of comparison with Earth for its compositional similarity, active hydrological cycle, and distinct atmospheric dynamics. We investigate the governing physics of climate, clouds, and convection on both bodies with the goal of learning general truths that broadly apply to most, if not all, moist planetary atmospheres. We focus, in particular, on the effects of low to high moisture concentration in the atmosphere. First, it is found that Earth's climate is remarkably stable to significant changes in atmospheric moisture content. In Earth-like climate states, the vapor pressure path at the anvil cloud level is fixed due to spectroscopic properties of water vapor. The largest changes in Earth's climate occur at tipping points that involve transitions from multi-layered to single-layered convective clouds. Second, we demonstrate that the height

of congestus cloud-top formation in the tropics is driven by a mid-tropospheric decline in the water vapor emissivity in clear-sky regions, which causes clouds to detrain preferentially between 5-6 km. This clear-sky theory of cloud formation is derived from basic assumptions of mass and energy balance and so should generalize well to other locations on Earth or to other planets and different atmospheric compositions. Third, we show that the transition from steady, quasi-equilibrium (QE) precipitation on Earth to non-steady, relaxed oscillator (RO) precipitation on Titan is predicted by the breakdown of a heat engine model of convection with increasing surface temperature and/or atmospheric moisture content. The breakdown of quasi-equilibrium dynamics occurs due to an imbalance between the work performed by the convective heat engine and the heat of condensation released by the convective motions themselves. The heat engine perspective offers a robust point of comparison between the atmospheres of Earth and Titan based on the first and second laws of thermodynamics, which are system invariant. The heat engine model is, in fact, agnostic of the working fluid and the condensing substance and, arguably, is the best framework to explain why dynamical similarities between present day Titan and a much warmer Earth exist.

The dissertation of Francisco Eduardo Spaulding-Astudillo is approved.

Jonathan M. Aurnou

Marcelo Chamecki

David A. Paige

Jonathan L. Mitchell, Committee Chair

University of California, Los Angeles

2023

To my parents

who taught me how to wonder

and to wander where I am called

TABLE OF CONTENTS

LIST OF FIGURES

LIST OF TABLES

ACKNOWLEDGMENTS

There are many people who have inspired, motivated, encouraged, and helped me in my academic career, to whom I have an enduring, profound gratitude. I am indebted to my Ph.D. advisor at UCLA, Jonathan Mitchell, for his endless support, patience, and guidance. It has been a joy to learn from and work alongside you in the pursuit of solutions to interesting scientific questions, and to be encouraged to think deeply about subjects that I care deeply about. I gratefully acknowledge my past mentors - Beth Orcutt and David Fields (Bigelow Laboratory for Ocean Sciences), Ivana Cerovecki, Matthew Mazloff, Sarah Gille, and Lynne Talley (Scripps Institution for Oceanography), Malte Jansen and Dorian Abbot (University of Chicago) and Eli Tziperman (Harvard University) - and my colleagues far and wide that have enriched my academic experience. In no particular order, they are Daven Khana, Halley McVeigh, Evie Fachon, Phoebe Thompson, Olivia Pardo, David Plotkin, Daniel Koll, Jade Checlair, Navah Farahat, Jonah Bloch-Johnson, Minmin Fu, Wanying Kang, Olivia Pardo, Molly James, Anna Lea Albright, Andrea Salazar, Mark Hubbert, Will Misener, Leslie Insixiengmay, Taylor Dorn, Akash Gupta, Bowen Fan, Namrah Habib, Cheng Li, Or Hadas, Juan Lora, Matthew McKinney, Tersi Arias-Young, Spencer Hill, Hung-I Lee, Rebecca Lewis, David Moore, Gavin Madakumbura, Wyatt Arnold, Sam Taira, and Lauri Holbrook. I thank all the members of my committee - Jonathan Mitchell, Dave Paige, Marcelo Chamecki, and Jon Aurnou - for overseeing my progress and for their helpful comments and constructive criticism. I extend my gratitude to Max Popp, who kindly provided me with the version of the ECHAM6 climate model that I used in the majority of my Ph.D. work and, in addition to Ben Winjum, contributed technical assistance along the way. This work was supported by NSF Grant 1912673 and an Early-Career Fellowship from the Center for Diverse Leadership in Science at UCLA. In addition, I thank CDLS and, in particular, Aradhna Tripati (UCLA) for funding the summer I spent writing my dissertation. Finally, I thank my family and friends for their unconditional support.

VITA

2017	B.S. (Geophysical Sciences), University of Chicago, Chicago, Illinois.
2017–2018	Post-baccalaureate researcher, University of Chicago, Chicago, Illinois.
2018–2023	Teaching Assistant, Deparment of Earth, Planetary, and Space Sciences, UCLA.
2018–2023	Graduate Student Researcher, Deparment of Earth, Planetary, and Space Sciences, UCLA.
2021	M.S. (Geophysics and Space Physics), UCLA, Los Angeles, California.

PUBLICATIONS

Spaulding-Astudillo, F. E., and J. L. Mitchell, 2023a: Effects of Varying Saturation Vapor Pressure on Climate, Clouds, and Convection. *J. Atmos. Sci.*, 80, 1247–1266, https://doi.org/10.1175/JAS-D-22-0063.1.

Spaulding-Astudillo, F. E., and J. L. Mitchell, 2023b: The emergence of relaxation-oscillator convection on Earth and Titan. *Planetary Science Journal*. (in revision).

Spaulding-Astudillo, F. E., and J. L. Mitchell, 2023c: Clear-sky convergence and the origin of tropical congestus clouds. (submitted).

CHAPTER 1

Introduction

This dissertation considers three fundamental questions in climate science. The first question may be stated: (Q1) How does the abundance of moisture in the atmosphere influence climate, clouds, and convection? Because Q1 is so broad, we limit ourselves to a comparative study of two bodies in the Solar System with moist atmospheres for which we have observational data: Earth and Saturn's moon Titan. The remaining questions lie within the broad umbrella of Q1 but are more limited in scope: (Q2) Why do tropical congestus clouds on Earth form at a height of 5-6 km?; (Q3) Why do Earth and Titan have distinct patterns of precipitation? The spirit of scientific exploration embodied by the approach taken in this work is to reduce the complexity of the climate system to its essential elements and identify driving physics that are general to most, if not all, planetary atmospheres. In so doing, we may also simultaneously push outward the boundaries of our understanding of the planet that we live on. In the remainder of this introduction, we shall define various climatological concepts that will be important to the understanding of the work as a whole and elaborate on the phenomenology that motivates Q1, Q2, and Q3.

The atmosphere of a planet is a mixture of multiple gases that occur at various concentrations over a specific range of temperatures and pressures. A constituent that undergoes phase change within the atmosphere is known as a *condensable* (Pierrehumbert & Ding, 2016). *Clouds* are the condensed phases (liquid or solid) of a condensable that are suspended in the atmosphere (Moran et al., 2018). A constituent that always remains in a gaseous state is a *non-condensable*. The atmosphere of Earth, for example, is composed of

multiple non-condensables including, but not limited to, nitrogen, oxygen, carbon dioxide, and methane and a single condensable: water. Whether or not a molecule such as water or nitrogen may also exist as a liquid or as a solid is determined by its melting and/or boiling point and the thermodynamic state of the atmosphere. The atmosphere of the Saturnian moon Titan, for example, is so cold that methane and, sometimes, nitrogen are condensables (Mitchell & Lora, 2016; Tokano, 2017) and water is part of the icy bedrock of the planet's surface (Griffith et al., 2003). A *moist atmosphere* is one where a gaseous condensable is present in radiatively- and/or thermodynamically-significant quantities. Under this definition, Earth, Titan, and Mars (where carbon dioxide and water vapor readily condenses) have moist atmospheres. In fact, there are no planets in the solar system with substantial atmospheres that do not qualify.

In thermodynamic equilibrium, the concentration of a condensable in the atmosphere is primarily determined by its *volatility* (McKay et al., 1991). Volatility is here defined as the saturation vapor pressure of a condensable at the typical temperature of the planetary surface. The unique relationship between the temperature of the system and the partial pressure of the condensable is given by the integrated Clausius-Clapeyron equation:

$$e^*(T) = e_0 \exp\left(\frac{-L_v}{R_v}\Big(1/T - 1/T_0\Big)\right), \tag{1.1}$$

where e^* is the saturation vapor pressure (SVP), L_v is the latent heat of vaporization of the condensable, R_v is the specific gas constant of the condensable, and e_0 is the SVP at some reference temperature T_0. In the Clausius-Clapeyron equation, the ratio L_v/R_v controls how quickly the SVP of a condensable increases in response to increases in temperature, and e_0 quantifies its intrinsic volatility (Pierrehumbert, 2010). The intrinsic volatility depends on the strength of the inter-molecular bonds of the condensable. The inter-molecular attraction of water molecules is higher than, for instance, molecules of methane and, for this reason, methane is more volatile than water.

Water is involved in almost every aspect of Earth's climate. In the atmosphere, it read-

ily condenses, forming clouds and precipitation that collects over land in lakes and rivers and in deep oceans. The atmosphere loses energy over time through a process known as radiative cooling. Water vapor is the dominant contributor to radiative cooling in the troposphere - the lowermost layer of Earth's atmosphere - much more so than, for instance, carbon dioxide, methane, or ozone (Harrop & Hartmann, 2012). The properties of water vapor that make it an effective emitter of infrared radiation are also the reason why it is an important greenhouse gas. Greenhouse gases have a warming effect on the surface by absorbing infrared radiation before it can escape to space and re-radiating it downward (Held & Soden, 2000). Although Earth's atmosphere effectively absorbs infrared radiation, the vast majority of sunlight passes through Earth's atmosphere without being absorbed (Wallace & Hobbs, 2006). Water condensation warms the troposphere, partially or entirely offsetting the infrared cooling due to water vapor (O'Gorman et al., 2012). In Earth's tropics, there is an approximate balance between radiative cooling, condensational heating, and surface sensible heat (Jakob et al., 2019) known as *radiative-convective equilibrium* (RCE). Outside the warm tropics where water exists in insufficient quantities, local energy balance requires equator-to-pole advective heat transport and RCE breaks down (Miyawaki et al., 2022).

Water clouds are ubiquitous on Earth (King et al., 2013), and their radiative effect is significant (Ramanathan et al., 1989). The net cloud radiative effect (CRE) is typically expressed as the sum of two deltas:

$$\mathrm{CRE} = \Delta\mathrm{SW} + \Delta\mathrm{LW} \tag{1.2}$$

$\Delta\mathrm{SW} \leq 0$ is the difference in absorbed shortwave radiation between a cloudy and cloud-free atmosphere. In general, the absolute value of ΔSW is larger when clouds are more reflective. Similarly, $\Delta\mathrm{LW} \geq 0$ is the difference in emitted longwave radiation to space between a cloudy and cloud-free atmosphere. ΔLW is larger when clouds are more effective at absorbing and re-emitting atmospheric radiation. ΔSW and ΔLW are computed at the same instant in time, where reality is typically represented by the cloudy state and the cloud-free state is a hypothetical one. The height at which a cloud forms is a key determinant in the sign of

its CRE (Yuan & Oreopoulos, 2013). Low-level clouds have the advantage of forming in relatively warm conditions close to their surface moisture supply. For this reason, low clouds have high concentrations of cloud condensate, which makes them very reflective and hence they have large ΔSW. Since low clouds form at the base of the troposphere, they block little of the outgoing longwave radiation to space and as a result have small ΔLW. The reverse is true of high clouds, which form at lower temperatures where water vapor is more scarce but are are positioned effectively to prevent radiation emitted from warmer, underlying layers from escaping to space. For these reasons, the sign of CRE tends to be negative (cooling) for low clouds and positive (warming) for high clouds. There is a gradual transition in the sign of CRE at intermediate levels because of these competing longwave and shortwave effects. These basic rules of CRE are thought to generalize well to other planets and cloud compositions, such as carbon dioxide and water clouds on Mars (Colaprete & Toon, 2003; Kite et al., 2021).

Water vapor is an important driver of convection on Earth. Convection is the vertical displacement of air as a result of density gradients in an atmosphere (Lin et al., 2022). There are two types of convection: dry and moist. Dry (moist) convection is the vertical displacement of air without (with) condensation. When an air parcel rises through the atmosphere, the background pressure decreases, causing the air parcel to expand and cool as it does work against its surroundings (Wallace & Hobbs, 2006). Latent heat release in a moist air parcel causes the temperature to decrease less rapidly with height than a dry air parcel displaced from the same initial location. If the parcel rises without exchanging mass or heat with its surroundings, it is said to do so *adiabatically*. If the parcel mixes with its surroundings as it ascends, it does so *non-adiabatically*. The vertical rate of change of temperature associated with adiabatic or non-adiabatic moist convection is broadly defined as the *moist lapse rate*. A saturated parcel ascending along the moist lapse rate is usually warmer than the sub-saturated environment in which it is embedded, and therefore it experiences an upward buoyant force. The vertical integral of the positive buoyancy force along the upward

trajectory of an adiabatic parcel is known as the *convective available potential energy*, and quantifies the work done by the environment to lift the adiabatic parcel from its initial height to the level of neutral (zero) buoyancy. On Earth, convective motions are aided by the low molecular weight of water vapor relative to the non-condensable background gases (Seidel & Yang, 2020). The lightness of water vapor implies that a parcel of air at the same temperature and pressure as its environment but that is enriched in water vapor will be positively buoyant and ascend (Yang & Seidel, 2020).

Like any other trade, climate scientists require specialized tools to perform their work. We require observations of nature, which remote sensing devices such as satellites provide, and we require a laboratory to run experiments and test hypotheses. While nature itself is the ultimate laboratory, it need not conform to our specific experimental requirements. Models are a virtual laboratory in which the relevant calculations are performed by a computer, and research institutions across the world invest substantial resources in their development, aiming to accurately simulate natural processes (Eyring et al., 2016). A *climate model* is a numerical code that solves the physical equations governing the conservation of mass, energy, and momentum within a connected land-ocean-atmosphere system (Balaji et al., 2022; Stute et al., 2001). To run a climate model on a computer, the physical equations are discretized and integrated forward in time on a gridded spatial mesh of the system (Kajishima & Taira, 2017). The spatial and the temporal resolution of the model refers to the size of the horizontal and vertical grid spacing and of the time step. The computational cost of a climate model increases as the spatial and/or temporal resolution increases (Grundner et al., 2022). For this reason, an increase in spatial resolution or domain size usually comes at the expense of the other. There are, at least, three types of climate model that are differentiated by domain size and spatial resolution. As we shall learn, these differences make them valuable in distinct contexts. Known as as a cloud- or convection-resolving model (CRM; Satoh et al., 2019), the first type is a regional climate model with a limited horizontal domain of 10-1000 km and a fine horizontal and vertical resolution of around 1 km and 10-100

m, respectively. CRMs are aptly named because they resolve the vertical motions associated with convective clouds (Guichard & Couvreux, 2017). For this reason, CRMs are the model of choice for cloud studies. Simulating the regional climate faithfully with a CRM typically requires boundary conditions that are representative of the large-scale forcing on that region due to non-local mass, energy, and momentum transports (e.g., Salathé et al., 2010). Known as a general circulation model (GCM), the second type is a global climate model with a spherical, Earth-sized domain, a coarse horizontal resolution of several degrees latitude and longitude, and a vertical resolution of 100-1000 m (Balaji et al., 2022). GCMs prove invaluable when comprehensive insight into the global climate is necessary. GCMs that incorporate real-time observations at each time step to enhance the realism of climate simulations are referred to as *re-analysis models* (Gelaro et al., 2017). A disadvantage of the coarse spatial resolution of GCMs is that many physical processes are not resolved. To address this, many GCMs employ parameterizations or "schemes", which are statistical approximations to the unresolved physics (e.g., Stevens et al., 2013; Tiedtke, 1993; Sundqvist et al., 1989). Parameterizations compute the unresolved, sub-grid scale variability of a climate variable in terms of resolved, grid scale quantities (Smith, 1990). Even cloud-resolving models (CRMs) employ parameterizations for processes that occur at spatial scales below the model resolution, such as cloud microphysics (e.g., see Grundner et al., 2022). It is a well known phenomenon that GCMs initialized with the same initial conditions diverge in their predictions of future climate outcomes (Lambert et al., 2020). The largest source of inter-model spread in GCM projections of, for example, climate sensitivity stems from the predicted changes in cloud cover (Meehl et al., 2020; Schneider et al., 2017; Stauffer & Wing, 2022), a process that is parameterized in most, if not all, GCMs. Institutions that maintain GCMs often develop their own parameterizations, and this has led to a proliferation of parameterizations among models (Tompkins, 2005). To mitigate the inherent bias introduced by parameterization in a single model, a common approach in climate prediction is to use a large number of climate models (i.e. a model ensemble) which together provide a better

prediction than just one model alone (e.g., Eyring et al., 2016). This ensemble approach recognizes that individual models excel in certain aspects while falling short in others, and aggregating their predictions yields a consensus that approximates reality more closely (Raju & Kumar, 2020). Due to these persisting challenges, climate models with fewer parameterizations and higher spatial resolution are usually considered more robust (Satoh et al., 2019). The third model type is a *single-column model* (SCM), which is a GCM evaluated at a single grid cell over which resides a single column of atmosphere (Christensen et al., 2018). SCMs are often energetically-isolated from neighboring grid cells (e.g., Popp et al., 2015), thereby isolating the local response to changes in surface temperature, moisture content, or other forcings. Consequently, SCMs serve as valuable tools for evaluating GCM parameterizations by enabling exploration of local parameterized processes independently of the resolved, large-scale physics (Gettelman et al., 2019). A drawback of SCMs is that, like GCMs, they have a coarse resolution relative to CRMs, which necessitates the use of parameterizations for many processes including convection, cloud microphysics, and eddy diffusion (Somerville & Iacobellis, 1999; Stevens et al., 2013; Möbis & Stevens, 2012). The simplest type of climate models are *analytical*, which refer to steady-state solutions of the governing physical equations of the atmosphere (Romps, 2014, 2017). To find an analytical solution, in most cases, requires a series of simplifying assumptions. The simplest models yield results that are straightforward to interpret and serve as valuable tools for understanding the behavior of more complex models (Jeevanjee et al., 2017). A common aphorism is that "all models are wrong, but some are useful". This adage applies also to climate models, which have furthered our understanding of the climate system in significant ways but also have certain advantages and disadvantages that must be carefully considered. We will discuss studies that utilize GCMs and CRMs - requiring the reader to possess basic knowledge of them - though we do not directly employ them in our work. Instead, we begin at the simpler end of the modeling hierarchy, starting with analytical models and single-column models, and lay the groundwork for future research involving more complex models such as GCMs and CRMs.

This approach is advantageous for the study of climate, clouds, and convection, which is the focus of this work, because it allows us to easily identify how these processes are impacted by local forcings. The disadvantage of this approach is that we have to put our faith in the model parameterizations, which are often "tuned" to replicate Earth's current climate conditions (Mauritsen et al., 2012). When perturbing Earth's climate from its current state, these parameterizations may no longer accurately represent reality. This makes it difficult to make robust predictions on the basis of a single model alone. For this reason, we intend to verify our published findings in Chapter 2 - in which we used the ECHAM6 SCM (Stevens et al., 2013) - with a high-resolution climate model with fewer parameterizations (e.g., a CRM) in future work.

Cloudiness is often quantified in terms of *cloud fraction* (Kay & Gettelman, 2009), which is the ratio of the surface area covered by clouds to the total surface area. We categorize clouds on Earth into three main types or "modes" depending on their cloud top height. Clouds that form and/or terminate between 0-4 km, 4-7 km, and 7-15 km are referred to as low-level/"low" clouds, mid-level clouds, and upper-level/"high" clouds, respectively. The vertical distribution of cloudiness, which largely determines the magnitude and sign of the local CRE (Hartmann et al., 2018), has a strong dependence on latitude (Sassen & Wang, 2008). In Figure 1.1b, we show the spatially-averaged cloud fraction observed over low-latitude, mid-latitude, and high-latitude regions by combined radar and lidar measurements from the CloudSat and CALIPSO satellites from 2006-2019 (Bertrand et al., 2023). At low latitudes (0-23.5°N/S), there are three distinct cloud populations. The peaks in cloudiness associated with these three modes occur approximately at 1 km, 5 km, and 13 km. Cloudiness is bimodal at mid-latitudes (23.5-35°N/S), with well-separated low clouds and high clouds peaking at 1km and 9km, respectively. At high-latitudes (50-80°N/S), there is a relatively low abundance of high clouds and no clear separation between low and mid-level clouds. One possibility is that these significant variations in cloud modality are controlled by the concentration of water vapor through the equator-to-pole temperature gradient created by

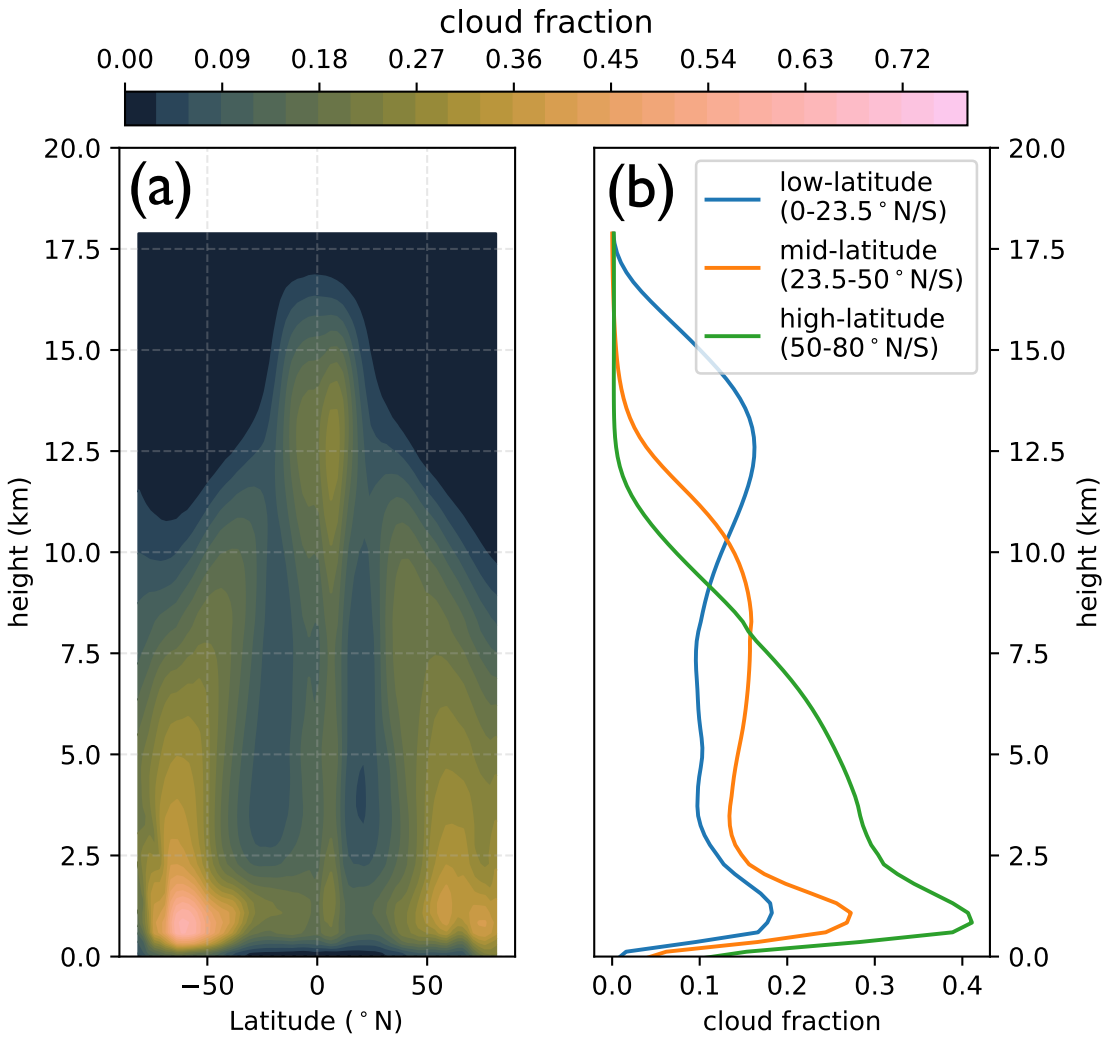

Figure 1.1: Combined CloudSat/CALIPSO observations from 2006-2019 (Bertrand et al., 2023) of (a) zonal-mean cloud fraction and (b) meridional averages of zonal-mean cloud fraction at low-, mid- and high-latitudes.

the unequal absorption of shortwave radiation at the Earth's surface. In Chapter 2, we investigate the hypothesized connection between the vertical separation of cloud modes and water vapor concentration, and carry out experiments with the ECHAM6 SCM (Stevens et al., 2013) where we artificially vary the amount of water vapor in the atmosphere.

The zonal-mean cloud fraction from CloudSat-CALIPSO satallite observations between 2006 and 2019 is given in Figure 1.1b as a function of latitude. The convective cloud populations that are dominant at low latitudes are shallow cumulus, mid-level congestus, and deep cumilonimbus (Johnson et al., 1999). Shallow cumulus are fair-weather clouds that form in horizontally-separated cells at the top of the atmospheric boundary layer (Albrecht et al., 2019). Cumilonimbus are deep convective and precipitating clouds that rise out of the boundary layer and detrain near the tropopause (Hartmann et al., 2018). Congestus clouds rise above shallow cumulus but are less vertically developed than deep cumilonimbus, and therefore detrain at intermediate heights (Wall et al., 2013). Deep cumilonimbus and congestus clouds are both associated with the formation of thin, sheet-like clouds through anvil-shaped convective outflow of condensed water at the detrainment level (Sassen et al., 2009; Bourgeois et al., 2016). Interestingly, the cooling effect of thin, mid-level clouds is thought to partially or entirely-offset the greenhouse warming effect of the upper-level cirrus clouds (Bourgeois et al., 2016). A minimum in mid- and upper-level cloudiness is seen in the descending branch of the Hadley cell at roughly 25°N/S. Descending air in this region is adiabatically warmed and produces a stable capping inversion over the boundary layer that inhibits deep convection (Schubert et al., 1995). In the subtropical zone (23.5-35°N/S), stratocumulus clouds are abundant (Sassen & Wang, 2008). They cover approximately 20% of the Earth's oceans, and are most common over cool waters off the western boundaries of continents (Wood, 2012). Stratocumulus clouds differ from fair-weather cumulus in that they form extensive, unbroken sheets. Both populations of low clouds are sustained by radiatively-driven shallow circulations that couple them to their surface moisture supply (Albrecht et al., 2019). The higher area coverage of stratocumulus clouds, however, causes

the shallow circulation to be driven by longwave cooling at the cloud top rather than shortwave absorption at the surface as in the case of cumulus clouds (Stevens, 2006; Schneider et al., 2019). At high latitudes, low- and mid-level stratus are the most abundant populations (Sassen & Wang, 2008) and they produce the continuous distribution in Figure 1.1b.

Since it was realized that tropical (0-23.5°N/S) convection is trimodal (e.g., Malkus & Riehl, 1964; Johnson et al., 1999), a debate has persisted regarding the formation height of congestus cloud tops (Redelsperger et al., 2002). This mode exclusively manifests in the tropics (Figure 1.1b), suggesting the potential importance of local warm and wet conditions. The congestus mode terminates at an altitude of 5-6 km (Figure 1.1b), with the spread here representing typical values of ocean and land, respectively (Wall et al., 2013). The prevalence of deep convection, where convection ascends from the surface to the tropopause, in the tropics implies that some mechanism decelerates rising air parcels through buoyancy reduction, causing them to detrain preferentially at the 5-6 km level. Two explanations for the formation height of congestus clouds are most prominent: the weak stability theory and the dry entrainment theory (Jensen & Genio, 2006). Both explanations rely on buoyancy arguments. The weak stability theory posits that transient and/or semi-permanent areas of weak stability in the mid-troposphere act as barriers to convective cloud development. Various mechanisms that generate weak stability have been proposed, including melting of stratiform cloud ice crossing the 0°C freezing level that occurs at 4-5 km in typical tropical conditions (Johnson et al., 1996), re-evaporation of detrained cloud condensate (Nuijens & Emanuel, 2018), and sublimation cooling as a result of dry air intrusions (Zuidema et al., 2006). In contrast, the dry entrainment theory asserts that dry air is entrained into ascending clouds, thereby curbing their vertical growth through dilution (Redelsperger et al., 2002). As a consequence of moist convection, tropical relative humidity has a "C"-shaped vertical distribution with maxima in the lower and upper-troposphere, respectively, and a minimum in the mid-troposphere (Romps, 2014). A common assumption in climate modeling is that cloudiness is positively correlated with the ambient relative humidity (Tompkins, 2005).

The existence of the congestus mode defies the conventional logic of cloud formation because it peaks in the dry mid-troposphere. In fact, a limitation of these prior theories is that, individually, they fail to account for a wide range of observations related to congestus clouds. In addition to the congestus peak at 5-6 km (Figure 1.1b), it is well established that congestus clouds are more prevalent when the mid-troposphere is *drier* (Brown & Zhang, 1997; Takemi et al., 2004; Sokol & Hartmann, 2022). Although the dry entrainment theory implies why congestus clouds are more common in dry conditions, it does not explain why congestus clouds should form at 5-6 km when the absolute minimum in tropospheric humidity is at 7.5 km. Similarly, the weak stability theory associated with the 0°C freezing level indicates why convective clouds may preferentially detrain in the mid-troposphere, but not why mid-level cloud cover is enhanced by increasing dryness. In Chapter 3, we propose a novel explanation for the typical height of congestus cloud tops that is based on simple arguments of mass and energy conservation in an idealized tropical atmosphere. We investigate the radiative properties of two greenhouse gases - water vapor and carbon dioxide - with a line-by-line radiative transfer model and find that water vapor alone can explain (1) the preference for congestus outflow at 5-6 km and (2) the enhanced outflow when the mid-troposphere is drier.

We now shift our focus from Earth to Titan, Saturn's largest moon. Titan exhibits intriguing parallels with Earth. The atmospheres of both planets are predominantly composed of nitrogen, and each has a condensable that participates in an important hydrological cycle involving clouds and precipitation (Dhingra et al., 2019; Frierson et al., 2006). Methane on Titan and water on Earth are known to coexist in liquid and gasesous states at the mean surface temperature of each planet. Comparisons are often drawn between these two planets because of the similar role that these condensables play in shaping their planetary environments (Coustenis & Raulin, 2011; Lorenz, 2005; Rannou et al., 2006). In other aspects, Earth and Titan are entirely dissimilar. Take, for example, the volatility of their condensables, defined as the saturation vapor pressure of each condensable at the typical surface temperature of each planet. Methane on Titan has a volatility approximately ten

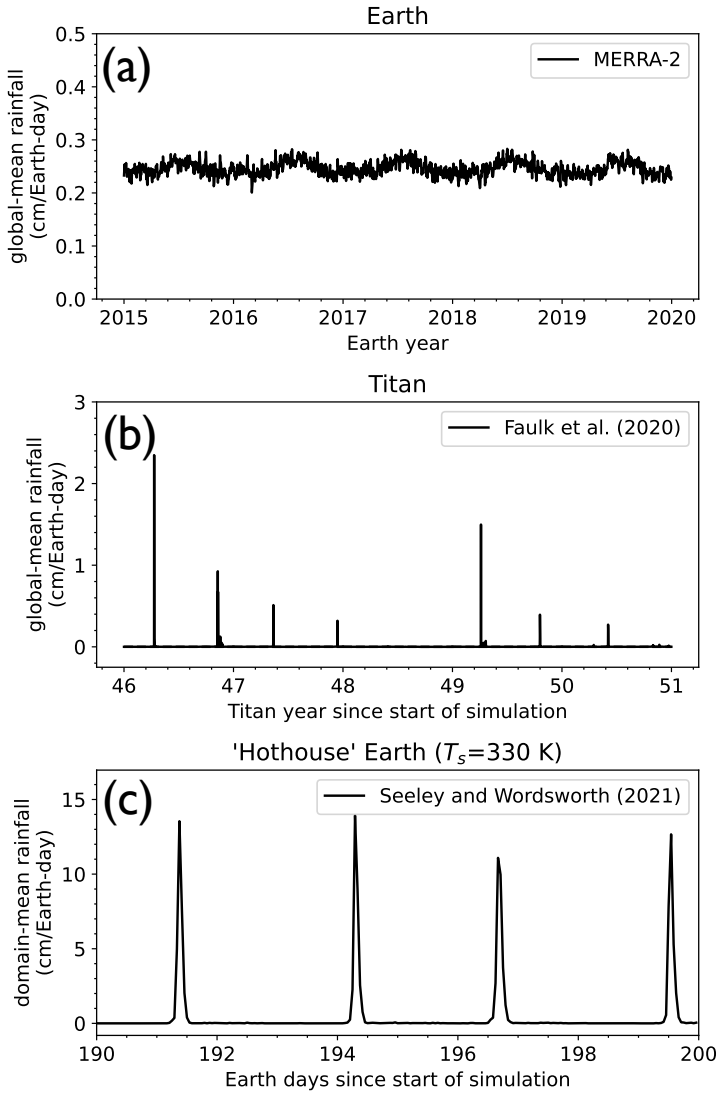

Figure 1.2: Comparison of global-mean precipitation on (a) Earth and (b) Titan from the MERRA-2 Earth climate reanalysis and Titan Atmospheric Model aquaplanet simulations from Faulk et al. (2020), respectively. In (c), we show the domain-averaged precipitation in cloud-resolving model aquaplanet simulations of the "Hothouse Earth" for a surface temperature of 330 K from Seeley & Wordsworth (2021).

times higher than that of water on Earth (Griffith et al., 2008). This significant difference in volatility explains in large part why Titan's atmospheric moisture content is over 100 times larger than Earth's (Hartmann, 2016a; Mitchell & Lora, 2016), despite Titan's surface being around 200 K cooler. In addition, 70% of the Earth's surface is covered by oceans that are several kilometers deep; in contrast, Titan's surface is mostly arid, except for methane lakes at high latitudes that collectively span just 1% of the global surface area (Mitchell & Lora, 2016). If the liquids in Titan's lakes were distributed over the entire planet, it would produce a shallow ocean of 1 m depth (Hayes, 2016). Conversely, if all the methane present in Titan's atmosphere were to condense onto its surface, it would form a global ocean of 5 meters depth (Tokano et al., 2006). This suggests the atmoshere of Titan stores more methane than is directly accessible at its surface. Therefore, Titan's atmosphere serves as a substantial reservoir of methane, distinct from Earth, where the primary reservoir of water is situated at the surface. Cloud formation on Earth is sensitive to the amount of moisture at the surface and in the atmosphere, as indicated by Earth's latitudinal variations in cloudiness (Figure 1.1b), and we suspect that this holds true for Titan as well. Although Earth's cloud cover is globally ubiquitous (King et al., 2013), Titan's cloud cover is sparse and frequently observed near high latitude lakes (Griffith et al., 2008), perhaps, because clouds require an abundant source of moisture to persist. On the other hand, the scarcity of clouds on Titan is surprising because methane vapor in the atmosphere is so plentiful (Tokano et al., 2006). Serendipitously, clouds and surface liquids cover approximately the same percentage of Earth's surface as they do on Titan over observationally-relevant timescales (Griffith et al., 2000; Hörst, 2017). At present, there is no general theory that can explain this striking difference in global cloudiness, and we flag it as a question deserving future study.

Due to observational limitations, no time-resolved global climatology of cloud fraction on Titan exists. For this reason, much about Titan's clouds remains uncertain. Regardless, there has been extensive effort to understand the factors that drive cloud formation in Titan's atmosphere (Griffith et al., 2000; Charnay & Lebonnois, 2012; Rafkin et al., 2022). Titan

has been described as an "all tropics" planet (Mitchell et al., 2006), owing to its effectively global Hadley cell and small pole-to-equator temperature contrast of 5 K. Methane clouds follow the seasonal migration of the inter-tropical convergence zone (Turtle et al., 2011a), which transits between poles and back in a single Titan year (roughly equivalent to 29 Earth years). Clouds form through local convection initiated by seasonal changes in temperature (Brown et al., 2002). During the CASSINI mission, various cloud system morphologies were observed including convective clusters in polar (summer) regions, elongated streaks in the zonal direction at mid-latitudes (Porco et al., 2005), and arrow-shaped clouds over low-latitudes organized by planetary-scale waves (Turtle et al., 2011a; Mitchell et al., 2011). High latitude clouds on Titan are often observed in convectively-unstable regions of the mid- and upper-troposphere (Griffith et al., 2000; Hörst, 2017). There is also evidence of boundary layer clouds forming over the poles on Titan (Charnay & Lebonnois, 2012), akin to cumulus clouds on Earth. While Titan does not seem to form the layered convective clouds that are so common on Earth (Yuan & Oreopoulos, 2013), Titan may have at least 2 quasi-permanent, non-convective cloud layers (Tokano et al., 2006). These stratiform clouds should form in the slowly-rising, saturated layers above 12 km with a gap in the cloud layer across the freezing level of methane where phase changes occur. It was argued that these stratiform clouds haven't been directly observed because they are optically-thin.

Though clouds are scarce on Titan from an annually-averaged perspective, no region is left untouched by Titan's extreme methane weather. As seen from Earth, the largest storms cover up to 10% of Titan's disk (Griffith et al., 1998; Schaller et al., 2009), which is equivalent to several million square kilometers. Titan is likely subject to heavy rains during these stormy episodes (Dhingra et al., 2019), during which vigorous fluvial erosion carves out channels and valleys and discharges the sediments into alluvial fans (Hörst, 2017). Titan's alluvial fan distribution is, in fact, positively correlated with the regions of heaviest precipitation (Faulk et al., 2017). Three-dimensional simulations of Titan reveal that precipitation can occur globally with a strong dependence of the size and frequency of events on latitude

(Faulk et al., 2017). For instance, precipitation less than 1 cm/day is much more common at high latitudes, but the most intense storms with rates higher than 1 cm/day occur over the mid-latitudes. This has helped to explain why alluvial fans are more common at mid- to high-latitudes. Storms have been observed directly on multiple occasions over Titan's low-latitude deserts (Schaller et al., 2009; Turtle et al., 2011b), far from Titan's polar methane lakes. In the breakup of a large low-latitude cloud system in 2010, an area of a half-million square kilometers appeared darker at multiple wavelengths, indicating significant methane precipitation (Turtle et al., 2011b). Surface "smoothing" at high latitudes after a cloud outburst has similarly been attributed to rainfall (Dhingra et al., 2019). Over the low-latitude desert regions, downward propagating winds associated with extreme weather are known to set the orientation of extensive dune fields (Charnay et al., 2015).

One of the most intriguing differences between Earth and Titan is the pattern of global-mean precipitation, given in Figure 1.2. On Earth, it is continuously raining such that, on any given day, the precipitation rate may be slightly above or below 2.5 mm/day (Figure 1.2a). There is some seasonal variability in global-mean precipitation with an amplitude $\leq 10\%$ of the total rate. The steady balance in the present-day Earth climate is known as *quasi-equilibrium* (QE; Emanuel, 2008; Arakawa & Schubert, 1974). Strictly speaking, QE refers to a statistical balance between radiative generation of potential energy and its conversion to kinetic energy by convection. The steady precipitation rate on Earth merely reflects that convection is continuously ongoing. On Titan, however, rain is the exception, rather than the rule (Figure 1.2b). Extended dry spells on Titan are interrupted by intense, short-lived storms with rainfall rates of several cm/day (Battalio et al., 2022). An analogy can be drawn between the quasi-periodic nature of precipitation on Titan and the canonical *relaxation oscillator* (RO) circuit (Pederson & Mayaram, 2008). The basic building blocks of a RO circuit are an energy source, a capacitor to store potential energy, and a threshold device that discharges the capacitor when the stored energy exceeds a threshold value. The periodic signal in a RO circuit is produced by charging and discharging the capacitor. In the

analogy between Titan's atmosphere and the RO circuit, the loss of radiant energy to space can be thought of as charging the capacitor. The "capacitor" is the store of potential energy that convection uses to drive atmospheric motion. In climate science, we refer to this store of energy as *convective available potential energy* (CAPE; Jkg^{-1}). Technically, CAPE is the maximum work done by the environment on a surface air parcel lifted adiabatically between the level of free convection (LFC[1]) and the level of neutral buoyancy (LNB[2]) (Wallace & Hobbs, 2006). In this simple analogy, the threshold device must be something that supresses convection for an extended period of time. In large storms, deep convection releases latent heat at all levels, returning them to neutral stability. If the amount of latent heat released in overturning convection is much larger than the amount of CAPE typically stored in the atmosphere, it would imply significant time delays between convective events. It is conceivable therefore that the "threshold device" is convective (latent) heating. Interestingly, Titan has similar values of CAPE to the modern-day tropics of Earth of 1000-3000 kJ/kg (Tokano et al., 2006; Seeley & Wordsworth, 2023), indicating the potential for large storms. However, convection can release far higher quantities of latent energy on Titan because Titan's atmosphere holds over 100 times more moisture than Earth's. We speculate that the generation and destruction of CAPE through radiative cooling and convective (latent) heating is in a steady balance on Earth (consistent with the QE hypothesis of Arakawa & Schubert (1974)), thus leading to the steady precipitation in Figure 1.2a. On Titan, we hypothesize that the fast process of moist convection destroys CAPE more efficiently than the slow process of radiative cooling can generate it. The slow generation and rapid destruction of CAPE could conceivably lead to extended dry spells interrupted by intense, convective storms, as is presently the case on Titan.

We have proposed that the difference in precipitation patterns on Earth and Titan is due to the differing concentrations of water vapor and methane vapor in their atmospheres.

[1]The LFC is the first height at which this air parcel is positively buoyant with respect to the environment.

[2]The LNB is the first height above the LFC at which the buoyancy force on the parcel returns to zero.

One way to test our hypothesis would be to raise the surface temperature of a planet with abundant surface liquids.[3] In a recent study of Earth's tropics, Seeley & Wordsworth (2021) did just that. They ran a high-resolution CRM over a small region of the Earth's tropics and increased the surface temperature. At surface temperatures above 320 K, they discovered that the Earth enters a "hothouse" climate state with extended dry spells lasting 2-3 days and periodic deluges lasting a few hours (Figure 1.2c). The point here is that RO states are possible in Earth's tropics at high surface temperatures. A consequence of these high temperatures is that the total precipitable water in Earth's atmosphere increases from a few centimeters to a few tenths of a meter, which is closer in magnitude to the total precipitable methane in Titan's atmosphere (Tokano et al., 2006). Returning to Figure 1.2b, we see that in simulations of Titan large storms are rare. Crudely estimating the recurrence interval in Figure 1.2b as 0.5 Titan years, we find that this is approximately 15 Earth years. Observations indicate that the period of the formation of large cloud systems on Titan is 3-18 months (Roe, 2012); however, it is not known how many of the cloud systems visible to observers actually generate precipitation that reaches the surface. Recent modeling studies have found that the number of large precipitation events per Titan year is greater than 1 and less than 10 (Battalio et al., 2022), which comes out to several Earth years between large precipitation events. The difference in timescales is intriguing, and we flag it as an unresolved problem that requires further study. Notably, Seeley & Wordsworth (2021) found that increasing water vapor in Earth's atmosphere produced lower-tropospheric radiative heating (LTRH). LTRH occurs when the flux of radiation into the lower troposphere is greater than the emitted flux. This occurs on Earth at high temperatures because the "water vapor window" closes (Koll & Cronin, 2018). The water vapor window is a region of the infrared over which the present-day atmosphere is transparent to infrared radiation (Pierrehumbert, 2010). As temperatures rise, water vapor becomes increasingly effective at absorbing within the win-

[3]Recall that, in thermodynamic equilibrium, the vapor pressure of a condensable increases monotonically with increasing temperature (Equation 1.1).

dow region and the lower atmosphere cannot directly cool to space (Wolf & Toon, 2015). Seeley & Wordsworth (2021) carried out a series of experiments in which they swapped out the interactive radiation scheme in their climate model for a fixed radiative profile with and without LTRH. In cases with imposed LTRH, RO states emerged at temperatures close to the modern-day tropics. In cases without LTRH, no RO states emerged. On the basis of these experiments, they concluded that LTRH is essential to the emergence of the RO state.

However, there are several reasons to favor a mechanism of RO emergence that is based on a comparison of CAPE and the latent heat released by moist convection over one based on LTRH. First, the hothouse Earth is not the only planetary environment in which RO behavior has been observed and/or simulated. For example, Figure 1.2b shows that simulations of Titan exhibit analogous behavior. On Titan, the atmosphere is close to *radiative equilibrium*, where the net radiative cooling rate at each height is zero due to a balance between upwelling, downwelling, and emitted radiative fluxes (Pierrehumbert, 2010). Radiative equilibrium is distinct from radiative-convective equilibrium (Jakob et al., 2019), where net raditive cooling is balanced by surface latent and sensible heat fluxes, which are vertically distributed through the atmosphere by convection. It is important to point out also that a hypothetical atmosphere in pure radiative equilibrium is convectively unstable, and therefore in reality such an atmosphere would inevitably convect when disturbed by a finite amplitude perturbation (Siebesma, 1998). Therefore, while LTRH may be a sufficient criterion for RO emergence on Earth, it is an insufficient criterion for RO emergence on Titan where the net radiative cooling is approximately zero. Quasi-periodic storm activity has also been observed and/or simulated in the atmospheres of Jupiter and Saturn (Sugiyama et al., 2014; Li & Ingersoll, 2015), in which the period between outbursts in Jupiter's atmosphere was found to be proportional to the assumed abundance of water vapor at the model's lower boundary. The recent discovery of RO dynamics in the gas giant atmospheres underscore the importance of latent heating for moist convection. On Jupiter and Saturn, water vapor is heavy relative to the abundant background gases of hydrogen and helium. Because of

molecular-weight effects, moist parcels of air tend to be negatively buoyant (Yang & Seidel, 2020). The release of latent heat is crucial for the moist parcel to attain sufficient buoyancy to overcome the molecular weight effect (Sugiyama et al., 2014). There is also the question of a forcing mechanism to lift moist parcels to the height where they become positively buoyant, which has been explained as penetrative downdrafts driven by evaporative cooling in a paradigm of convection in deep atmospheres that operates top-down rather than bottom-up (Sugiyama et al., 2014; Li & Ingersoll, 2015).

The motivation to construct a mechanism of RO emergence based on a comparison of CAPE and latent energy release by moist convection stems from the extensive literature on *convective heat engines*. A heat engine is a device that converts heat into mechanical work (Singh & O'Neill, 2022), in which heat is transferred to a hot reservoir and lost from a cold reservoir. Since solar radiation is deposited at the warm surface at temperature T_H and longwave radiation is emitted to space from colder air at temperature T_C, the atmosphere is a natural heat engine. If we define the system to be a parcel of moist air, then work is done on the system by its surroundings to move the parcel from its initial position at the surface to the top of the convecting layer (e.g., the tropopause). There is, however, a theoretical upper limit on the amount of heat that can be converted into work by the system (Singh & O'Neill, 2022). The so-called efficiency η of the heat engine is defined as the ratio of heat supplied at the hot reservoir to the work performed by the system. In a Carnot (ideal and reversible) heat engine, this ratio is

$$\eta = \frac{T_H - T_C}{T_H}. \tag{1.3}$$

For reference, a hypothetical atmosphere with a surface temperature of 300 K and a radiating temperature of 200 K would have a Carnot efficiency of 33%. In a real atmosphere, however, irreversible processes such as dissipation through surface friction and turbulent mixing, phase changes, and diffusion reduce the efficiency below that predicted by Equation 1.3 (Singh & O'Neill, 2022). In the convective heat engine model of Emanuel & Bister (1996), the link between CAPE and latent heat release by moist convection is made clear. In equilibrium,

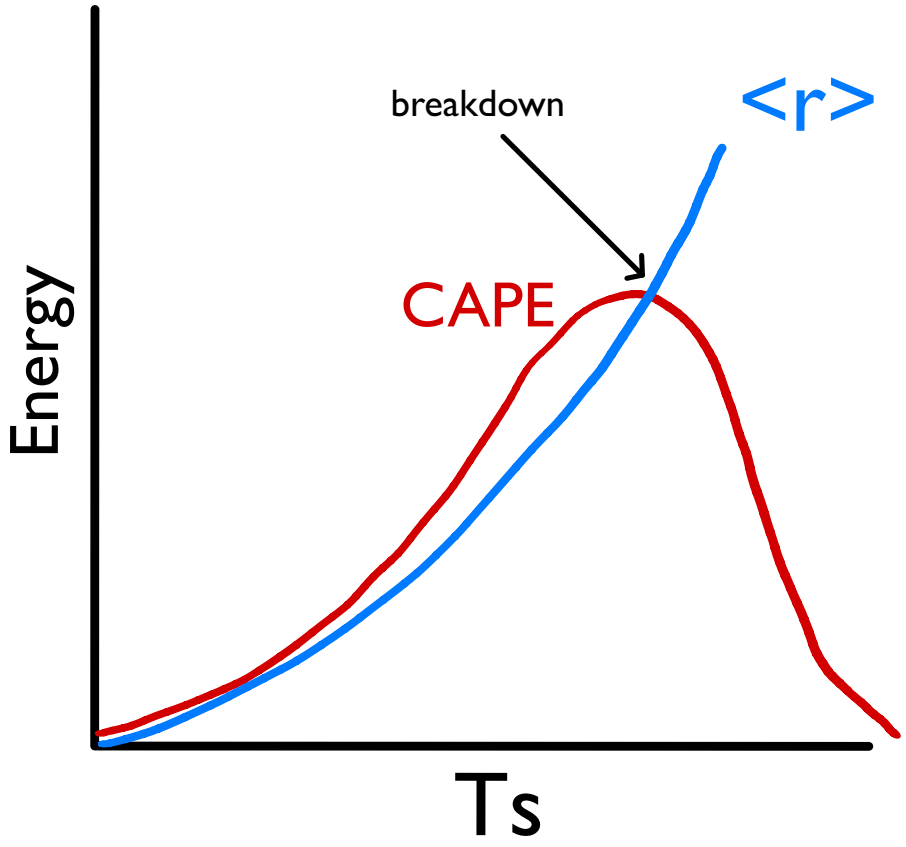

Figure 1.3: Comparison of convective available potential energy (CAPE; Jkg^{-1}) and latent heat released per unit mass of convecting atmosphere ($\langle r \rangle$; Jkg^{-1}) as a function of surface temperature. The breakdown of the zero-buoyancy heat engine model of convection is predicted by the divergence of CAPE and $\langle r \rangle$ (black arrow).

the entropy of any closed system is constant, requiring a balance between sources and sinks of entropy. Assuming that absorption and emission of radiation is a reversible sink of entropy and that the dominant irreversible source is dissipation of convective turbulence, it follows that the convective mass flux M ($\mathrm{kgm^{-2}s^{-1}}$) times CAPE is equal to the efficiency of the heat engine η times the mass-integrated radiative cooling of the atmosphere Q ($\mathrm{Wm^{-2}}$).

$$M \times \mathrm{CAPE} = \eta Q \tag{1.4}$$

Equation 1.4 relates the *rate of work* ($M\times$CAPE, which is approximately equal to the irreversible frictional dissipation) to the *rate of cooling* Q at an efficiency $\eta \equiv -\overline{T}_{irr}(1/T_s - 1/\overline{T}_{rad})$, where $\overline{T}_{irr}$ is the mean temperature at which dissipation occurs, $\overline{T}_{rad}$ is the mean temperature at which the planet radiates to space, and T_s is the surface temperature. Mass exchange between the sub-cloud layer[4] and the cloud layer[5] in the overturning circulation within the heat engine implies a net upward transport of energy that is released in the cloud layer as latent heat $\langle r \rangle$. The energy flux is proportional to the mass flux out of the sub-cloud layer M_{sc}, which in equilibrium must equal M (Equation 1.4). We refer to the requirement of no net vertical transport of mass in equilibrium ($M \approx M_{sc}$) within the heat engine as the "equilibrium condition". We show in Chapter 4 that an equivalent statement of the equilibrium condition is

$$M \approx M_{sc} \rightarrow \mathrm{CAPE} \approx \eta \langle r \rangle, \tag{1.5}$$

where $\langle r \rangle \approx L_v q_s^*$ is the release of latent heat per unit mass of convecting cloud ($\mathrm{Jkg^{-1}}$) and q_s^* is the surface saturation specific humidity. Interestingly, Equation 1.5 implies a breakdown of equilibrium at high surface temperatures for two reasons. First, it has been demonstrated in convection-resolving simulations that CAPE is a single-peaked function of surface temperature (Seeley & Wordsworth, 2023). As illustrated in Figure 1.3, CAPE increases/decreases with increasing surface temperature less/greater than 330 K on Earth

[4]The sub-cloud layer is the dry convective layer below the lifting-condensation level.

[5]The cloud layer is the moist convective layer above the lifting-condensation level.

and 105 K on Titan (Seeley & Wordsworth, 2023). The 6-7% increase in CAPE per degree Kelvin of surface warming on Earth is generated by the commensurate increase in the partial pressure of water vapor given by the Clausius-Clapeyron relation (Romps, 2016; Held & Soden, 2006). The peak in CAPE occurs on Earth at the surface temperature where the troposphere becomes *water-dominated*, here defined in terms of heat capacity where the contribution to the latter from the moist components exceeds that from the dry components (Romps, 2016). Second, $\langle r \rangle$ in a zero-buoyancy model of convection is proportional to the surface saturation specific humidity q_s^* (Romps, 2016), which increases *without bound* with increasing surface temperature at the same Clausius-Clapeyron rate. This unchecked growth of $\langle r \rangle$ with surface warming is illustrated in Figure 1.3. Therefore, if η remains roughly constant, the left-hand and right-hand sides of Equation 1.5 are likely to diverge with increasing surface temperature at or near the peak in CAPE (Figure 1.3), which would violate the equilibrium condition. We emphasize that the variables of interest in the heat engine model - CAPE and $\langle r \rangle$ - are largely determined by the concentration of condensable in the atmosphere, which may be increased or decreased as a function of the surface temperature. We therefore hypothesize that the violation of the equilibrium condition in the heat engine model is predictive of the transition between QE and RO states in a numerical climate model. In Chapter 4, we explore the qualitative difference in precipitation patterns on present-day Earth and Titan (Figures 1.2a,b) and the hothouse Earth (Figure 1.2c) using the zero-buoyancy heat engine perspective.

We have shown in numerous ways that Earth and Titan represent different planetary archetypes, which we now delineate. An *Earth-like* climate is one with limited condensable vapor, abundant surface liquids, partial cloud cover, and steady precipitation; a *Titan-like* climate is one with abundant condensable vapor, limited surface liquids, scarce cloud cover, and bursty precipitation. In Chapter 2, we investigate a question motivated by these planetary archetypes: (Q1) How does the abundance of moisture in the atmosphere influence climate, clouds, and convection? Q1 is also motivated by the significant variations in cloud

cover between Earth's equator and its poles, depicted in Figure 1.1b. The results of this study have been published in Spaulding-Astudillo & Mitchell (2023a). We vary the volatility of water vapor in Earth aquaplanet simulations conducted with the MPI ECHAM6 single-column model (Stevens et al., 2013). We find that varying the concentration of water vapor in Earth's atmosphere changes the properties of water clouds, including their height, abundance, radiative forcing, and horizontal area fraction. The most abrupt changes in cloudiness occur at climate tipping points (rather than in the stable "in-betweens"), which are explained using parameters that quantify cloud instability. Our volatility experiments lend insight to how an Earth-like climate transitions into a Titan-like climate. Notably, the vapor-rich climate states with several meters of precipitable moisture exhibit relaxed-oscillator precipitation patterns, which we follow up on in Chapter 4.

In Chapter 3, we investigate the origin of tropical congestus clouds, which produce the middle peak in low-latitude cloud fraction in Figure 1.1b. This cloud type is poorly represented even in state-of-the-art GCMs (Miao et al., 2019; Bodas-Salcedo et al., 2008). Many climate models, including the ECHAM6 SCM used in Chapter 2, do not generate this cloud mode likely because they employ parameterizations that assume a positive correlation between cloudiness and relative humidity (Sundqvist, 1988; Tompkins, 2005), the latter of which has a minimum in the mid-troposphere. Using a line-by-line radiative transfer model, we show that congestus clouds tops form preferentially at a height of 5-6 km due to a decline in radiative cooling with height that, in turn, drives convective detrainment. This decline in radiative cooling is linked to a sharp drop in the emissivity of water vapor in the mid-troposphere. Furthermore, we find that a drier mid-troposphere enhances the radiatively-driven outflow at 5-6 km. Our results imply that the representation of mid-level clouds could be improved by adding a positive correlation between cloudiness and *clear-sky convergence*, which refers to the horizontal transport of condensed water from convective clouds into clear-sky regions. This study has been submitted for publication.

In Chapter 4, we investigate why the climates of Earth and Titan have distinct patterns

of precipitation, which are depicted in Figure 1.2. This study is currently in revision at *PSJ*. What we present in Chapter 4 is a version of the revised manuscript. Joining a heat engine model of convection (Emanuel & Bister, 1996) with an analytical zero-buoyancy model of convection (Romps, 2016), we demonstrate that the combined model predicts an inevitable breakdown in quasi-equilibrium (QE) dynamics with increasing temperature and/or atmospheric moisture content. We find that the transition from QE- to RO-type precipitation is described by the surface temperature and/or moisture content of QE breakdown. Our investigation of the dynamical similarity between the hothouse Earth and Titan (Figure 1.2c) demonstrates that quasi-periodic storm activity is linked to atmospheric moisture content.

CHAPTER 2

The effect of varying saturation vapor pressure on climate, clouds, and convection

We investigate how climate, clouds, and convection change as the amount of water vapor in the atmosphere is varied by altering the saturation vapor pressure (SVP) by a constant in a one-dimensional climate model. We identify four effects of altering SVP on clouds in an Earth-like climate with distinct layers of low and high clouds. First, the anvils of high clouds get higher as SVP is increased (and vice versa) because they are bound by radiative constraints to occur at a lower temperature. The vapor pressure path above the cold anvils does not change in Earth-like climates. Second, low clouds get lower as SVP increases (and vice versa) because they are coupled to a convective boundary layer (CBL) that shallows primarily from an increase in the tropospheric static stability. The third and fourth effects follow from the first two, namely that single-layer cloud states exist both in vapor-poor states with a merged cloud deck and vapor-rich states with an elevated cloud deck. We identify two cloud instability parameters that determine the transitions between single- and double-layer cloud regimes. Qualitatively, sufficiently vapor-poor states have a deep, diffusive layer that overlaps with a weaker convective layer (topping out at the tropopause) that cannot maintain low relative humidity in the mid-troposphere through the drying of descending air, thus causing the cloud layers to merge. Sufficiently vapor-rich states lose their low clouds as the shallowing CBL drops below the lifting condensation level.

2.1 Introduction

Water vapor is essential to all aspects of Earth's climate, clouds, and convection. This is most obvious, perhaps, in the Earth's tropics where to good approximation a balance is struck between radiative cooling and condensational heating (O'Gorman et al., 2012). Water vapor is not only a latent source of energy, but it also controls the flow of radiation to space, as water is the strongest gaseous emitter of infrared radiation in the Earth's troposphere (Harrop & Hartmann, 2012). Clear-sky radiative cooling generates convective motions that, in turn, control the vertical distribution of water vapor and thereby the cloud distribution (Hartmann & Larson, 2002). In regions of high relative humidity, water vapor readily condenses into clouds (Slingo, 1980), introducing competing shortwave and longwave cloud radiative effects. Because its density is less than that of dry air at the same temperature, water vapor in sufficient, near-surface abundance is also a trigger of convection (Yang & Seidel, 2020). If the atmosphere has much more or much less water vapor, any and all of these processes are affected. This is evident in, for instance, the latitudinal variations in Earth's cloud phenomenology (Sassen & Wang, 2008).

Titan, Saturn's largest moon, has an active weather cycle involving evaporation and condensation of methane, and offers the only present-day point of comparison with Earth's weather. Like water, methane is a greenhouse gas with a positive climate feedback, transports heat horizontally and vertically, and triggers moist convection that is associated with precipitation and cloud formation (Mitchell & Lora, 2016). In other ways, Earth and Titan are quite distinct. Take, for example, the volatility of their condensables, which we define as the vapor pressure of water at Earth's conditions and that of methane at Titan's conditions. There is $\sim$100 times more precipitable methane in Titan's atmosphere ($\sim$5 m) than water in Earth's ($\sim$5 cm) (Tokano et al., 2006; Hartmann, 2016b). At the same time, Titan is weakly irradiated and far colder than Earth. Titan's atmosphere is optically thick at most infrared wavelengths, which along with frigid conditions ($\sim$70-90 K) makes it challenging

for the atmosphere to cool radiatively. Perhaps because of this, deep convection on Titan appears to be much rarer than on Earth (Lorenz, 2005) and clouds cover $< 1\%$ of Titan's global surface area, compared to almost 70% of the Earth's in the annual mean (Griffith et al., 2000; King et al., 2013).

The rarity of clouds and deep convection on Titan could be due to a number of other effects, for example, the differences in the microphysics of methane and water cloud formation. A fruitful approach to studying these differences is to develop separate weather/climate models for Earth and Titan (Rafkin et al., 2022; Lora et al., 2015). Adapting Earth climate and weather models to Titan necessarily involves changing many components simultaneously, which can obscure the causes behind any differences. In addition, the interesting physics that distinguish climate, clouds, and convection on Earth and Titan may occur in the parameter space between the two, where a climate tipping point or "regime change" occurs. An idealized experiment that accesses the parameter space between the end members is needed to identify whether a climate regime change is present.

Motivated by this, we ask a simple question: what would Earth's climate, clouds, and convection be like if water vapor were much more (or less) abundant? And relatedly, are there sharp regime changes (tipping points) in the equilibrium climate states? We carry out a numerical experiment varying a single parameter that controls water vapor abundance with a one-dimensional climate model built with the column physics of the ECHAM6 GCM (Popp et al., 2015, henceforth, P15). A scaling parameter for the saturation vapor pressure (SVP) put forward in a series of papers studying water vapor's role in an idealized GCM (Frierson et al., 2006, 2007),

$$e_{sat} = \xi e^*_{sat}(T), \tag{2.1}$$

is varied over states that are vapor-poor ($\xi < 1$) and vapor-rich ($\xi > 1$), where e_{sat} and e^*_{sat} are the altered and true SVP, respectively. The use of a 1D model facilitates the exploration of a wide parameter space, but comes at the expense of a number of approximations and parameterizations. Our goal with this paper is to identify the climate regime changes and

understand their behavior in 1D. We intend to follow up with a three-dimensional cloud-resolving model (CRM) in future work to test our findings.

Many other studies are focused on understanding the response of an Earth-like climate to significant changes in surface temperature due to some climate forcing, e.g. large changes in non-volatile greenhouse gases (Caballero & Huber, 2010; Schneider et al., 2019) or changes in sunlight (Wolf & Toon, 2015, P15). Our work is complementary, in that we independently vary Earth's volatile greenhouse gas (which can be regarded as a hypothetical climate forcing). We thus expect the effect of water vapor on the climate to be more clearly identifiable in our approach. We might also expect to find the same climate states as in P15, for instance, and their presence in our experiments would provide some validation of our approach.

In Section 2.2, we develop four hypotheses about the response of clouds to variations in moisture. In Section 2.3, we describe the climate model used in this study and our experimental method. In Section 2.4, we give an overview of our results and we evaluate our hypotheses. We characterize 3 cloudy climate states that emerge and explain the underlying cause of each climate transition with the help of two cloud-instability parameters. In Section 4.5, we discuss our results and compare them to previous work. Finally, in Section 2.6, we summarize our main conclusions.

2.2 How do climate, clouds, and convection respond to changing ξ?

The Earth's tropics are characterized by several distinct cloud populations in the vertical (Johnson et al., 1999). The two dominant modes in cloud fraction are located in the lower and upper troposphere (e.g., see Figure 1 from Seeley et al., 2019a), respectively, which we will refer to as low clouds and high clouds. Each mode consists of multiple cloud types. The main low cloud types are cumulus (Cu) and stratocumulus (Sc) (Cesana et al., 2019; Albrecht et al., 2019; Johnson et al., 1999), which cool the climate by increasing the planetary

albedo. An important way in which Cu and Sc are differentiated is by their fractional area coverage. Sc often form in sheets with a high area coverage that promotes strong radiative cooling from the cloud top (Wood, 2012), producing a turbulent circulation that couples the cloud layer to its source of moisture near the surface (Stevens, 2006). In contrast, Cu have moderate cloud fractions because the individual clouds are horizontally scattered. Surface heating primarily drives the turbulent circulation that resupplies moisture to Cu (Cesana et al., 2019). Whether conditions favor Sc or Cu depends on numerous factors. For instance, Sc (Cu) are more common over cold (warm) sea surface temperatures (SST) (Cesana et al., 2019). Where SSTs spatially vary, transitions between the main low cloud types naturally occur (Albrecht et al., 2019), for example, from Sc to Cu or vice versa. The main high cloud type is cumulonimbus (Johnson et al., 1999). A peak in detrainment is observed in the upper troposphere as a result of these deep convective clouds (Johnson et al., 1999), which are associated with convergence of cloudy air into clear-sky regions (Seeley et al., 2019a). The spreading anvils produce tropical cirrus that then persist for hundreds of kilometers away from the convective tower (Sokol & Hartmann, 2020; Sassen et al., 2009) and warm the climate by a greenhouse effect. In this study, we use a single-column GCM that through the parameterizations described in Section 2.3 produces low clouds and high (cirrus-like) clouds in simulations of Earth's present climate.

As we've pointed out, low clouds and high (cirrus-like) clouds have opposite effects on climate and are well separated vertically, but need they be? And are the two modes always present? We develop four hypotheses aimed at answering these questions. In Section 2.2.1, we form the first hypothesis – high clouds get higher as SVP increases – by making an assumption about anvil temperatures in altered climates. In Section 2.2.2, we form the second hypothesis – low clouds get lower as SVP increases – by considering how the height of a cloud-topped convective boundary layer depends on ξ. In Section 2.2.3, we form a third hypothesis – there exist vapor-poor states with single-layer clouds – that emerges intuitively from the first two. Finally, in Section 2.2.4, we form a fourth hypothesis – there exist vapor-

rich states with single-layer clouds – by considering an important constraint on low cloud formation. Later, in Section 2.4, we will test how varying water vapor through ξ affects the basic physics that account for the existence and vertical separation of low and high clouds in an atmospheric column.

2.2.1 Hypothesis 1: High clouds get higher

We hypothesize that high clouds get higher in more vapor-rich states. Our hypothesis is based on the Fixed Anvil Temperature (FAT) hypothesis put forward by Hartmann & Larson (2002). FAT links the decreases in longwave cooling near the tropopause to the height of the convective anvil clouds (Seeley et al., 2019b). Jeevanjee & Fueglistaler (2020a, henceforth, JF20b) recently showed that longwave cooling can be approximated as direct cooling-to-space from optical depth unity ($\tau_{\tilde{\nu}} = 1$) surfaces integrated over all wavenumbers, $\tilde{\nu}$, in the water vapor rotational band. The spectrally-integrated cooling rate is effectively the product of three parts: (1) Planck's law, (2) an emissivity gradient that depends on the thermodynamic state of the atmosphere, and (3) a spectral width that represents how many wavenumbers contribute to the total emission at each height. The key finding of JF20b is that part (3) controls the height where the cooling rate decreases because part (1) and part (2) cancel out over much of the troposphere. JF20b identified that at lower pressures fewer wavenumbers contribute to the spectrally-integrated cooling rate and this causes the cooling rate to drop. The drop happens at a characteristic value of the spectral absorption coefficient, κ_{ref}.

Interestingly, the theory of JF20b predicts that radiative cooling decreases at a fixed vapor pressure path (VPP $= \int_0^p e \, dp$, where e is the partial pressure of water vapor and p is total pressure). The dependence of cooling rates on VPP is covered in detail by Hartmann et al. (2022).

$$\text{VPP} = \frac{g \, p_{ref}}{D \, \varepsilon \, \kappa_{ref}} \approx 1.2 \times 10^4 \text{ PaPa}_v, \tag{2.2}$$

where $D = 1.66$ is the two-stream diffusivity factor, ε is the ratio of the specific gas constants

of dry air and water vapor, RH is relative humidity, and g is gravity. $\kappa_{ref} = 40$ m^2/kg is the absorption coefficient at which cooling rates are expected to drop (JF20b). JF20b obtain their absorption coefficient distribution from a reference pressure of $p_{ref} = 500$ hPa. Equation (2.2) is obtained by setting the spectrally-resolved optical depth to unity at κ_{ref} and solving for VPP. For those interested, a full derivation of Equation (2.2) is provided in Appendix 2.7. The units of VPP are pressure of air (Pa) times partial pressure of water vapor (Pa$_v$). Note that Equation (2.2) depends only on fixed spectroscopic and thermodynamic properties of water vapor.

Our ξ experiment perturbs the thermodynamic state of the atmosphere, but has no effect on the spectral properties of water vapor (which constrain the VPP). Therefore, we expect that the VPP where the clear-sky longwave cooling rate decreases and the high cloud forms should not vary as ξ increases. If this constraint holds, we expect that increasing ξ requires the cloud pressure to decrease to offset the moisture increase at each height. We also expect that the cloud temperature decreases with increasing ξ. If the cloud forms at roughly the same vapor pressure as we move from ξ_1 to ξ_2 where $\xi_1 < \xi_2$, then by this assumption $\xi_1 e_{sat}(T_1) = \xi_2 e_{sat}(T_2)$ and therefore $T_2 < T_1$. If both the cloud temperature and environmental lapse rate decrease, then the cloud should rise. In complementary work, Harrop & Hartmann (2012) vary the radiative effect of water vapor in the upper troposphere by specifying the water vapor amount fed into their model's radiative transfer scheme. When the partial pressure of water vapor was increased, the cloud maximum moved upward to a lower temperature.

2.2.2 Hypothesis 2: Low clouds get lower

Heating of the surface by shortwave absorption generates turbulence that sustains Cu clouds. From prior work (e.g., Figure 2 from P15) and knowledge of the shallow convection scheme (Tiedtke, 1989) in the 1D GCM used in this study (ECHAM6), one confidently expects the low-level clouds in 1D simulations of the present-day climate to fall into a Cu-like regime.

We assume that the simulated low clouds are coupled to the convective boundary layer (CBL), and therefore that their heights are coupled. Based on this assumption, we derive an equation for the equilibrium height of a cumulus-topped CBL from the model of Neggers et al. (2006, henceforth, N06) and then develop a hypothesis regarding how ξ changes the height of the low clouds.

For an isolated column in which there is no large-scale mass transport, the cumulus-topped boundary layer height, h in m, depends on the entrainment mass flux, E in m/s, and the convective mass flux, M in m/s, at the top of the boundary layer,

$$\frac{\partial h}{\partial t} = E - M. \tag{2.3}$$

Given expressions for E and M, one can solve for the h in steady state, $E = M$. E represents the change in boundary layer height from turbulent entrainment of free-tropospheric air while M represents the change in boundary layer height from the loss of air that reaches the LCL in rising thermals and is made positively buoyant by the release of latent heat. The entrainment mass flux is

$$E = \frac{-\overline{w'\Theta'_v}|_h}{\Delta\Theta_v} = \frac{0.2\overline{w'\Theta'_v}|_s}{\Delta\Theta_v}, \tag{2.4}$$

where $\overline{w'\Theta'_v}|_h$ and $\overline{w'\Theta'_v}|_s$ are the eddy heat fluxes at h and the surface, respectively, w' and Θ'_v are the vertical velocity and virtual potential temperature anomalies of buoyant plumes, and $\Delta\Theta_v$ is the moist tropospheric stability, which is proportional to the difference in virtual potential temperature between the boundary layer and the free troposphere. In CBLs, $\overline{w'\Theta'_v}|_h$ is of opposite sign and proportional to $\overline{w'\Theta'_v}|_s$ by a factor of 0.2 (Driedonks & Tennekes, 1984), which we assume is independent of ξ. $\overline{w'\Theta'_v}|_s$ can be written in terms of the surface turbulent fluxes (Deardorff, 1972),

$$\overline{w'\Theta'_v}|_s = \frac{\overline{SH}}{\rho c_p} + 0.61\Theta|_s\frac{\overline{LH}}{\rho L_v}, \tag{2.5}$$

where $\overline{SH}$ and $\overline{LH}$ are the sensible and latent heat fluxes at the surface (in units of Wm^{-2}), L_v is the latent heat of vaporization, c_p is the specific heat of dry air, ρ is the air density,

and $\Theta|_s$ is the potential temperature at the surface. The Δ symbol preceding a variable denotes a difference between its average value in the boundary layer and the overlying free troposphere:

$$\Delta\Theta_v = \Delta\Theta + 0.61\Delta(q\Theta); \tag{2.6a}$$

$$\Delta\Theta = C_\Theta^h(\Theta^{FT} - \Theta^{BL}); \tag{2.6b}$$

$$\Delta(q\Theta) = C_\Theta^h(q^{FT}\Theta^{FT} - q^{BL}\Theta^{BL}); \tag{2.6c}$$

$$\Delta q = C_q^h(q^{FT} - q^{BL}); \tag{2.6d}$$

where Θ is potential temperature, q is specific humidity, and $C_\Theta^h = 0.03$ and $C_q^h = 0.1$ are empirical transfer coefficients from the large-eddy simulations of N06, which we assume to be independent of ξ. Variables with the superscripts of ^{BL} or ^{FT} are pressure-weighted averages over the boundary layer or free troposphere, respectively. M is obtained by multiplying the convective velocity, w^*, by the convective area fraction, a_c,

$$M = a_c w^*. \tag{2.7}$$

$w^* = (\frac{gh}{\Theta_v}\overline{w'\Theta_v'}|_s)^{1/3}$ is the typical vertical velocity of eddies in the CBL. a_c is the fraction of eddies that reach the LCL and then leave the boundary layer, and is parameterized following Neggers et al. (2006, 2007) (see Section 2.4.3). Combining Equations (2.4)-(2.7) and setting $E = M$,

$$h_{cbl} = \left(\frac{0.2}{a_c\Delta\Theta_v}\right)^3 \left(\overline{w'\Theta_v'}|_s\right)^2 \frac{\Theta_v|_s}{g}. \tag{2.8}$$

Note that this is an implicit equation for h_{cbl} because a_c is a function of the CBL height. It is evaluated numerically by iterating over a series of guesses for h_{cbl} and finding where the equality holds within an acceptable margin of error (we arbitrarily choose ± 1 m).

It is not obvious how Equation (2.8) should vary as ξ increases. Mathematically, one reasonably expects that the terms raised to higher exponents will dominate Equation (2.8).

Assuming that this is the case, we focus on a_c and $\Delta\Theta_v$. We are unable to offer a simple explanation for how a_c will change, as this depends on the boundary layer turbulence, which has never been studied in varying-ξ experiments. $\Delta\Theta_v$, on the other hand, is a measure of the static stability of the atmosphere, which was found by Frierson et al. (2006) to increase with increasing ξ. The static stability is given by the vertical gradient in potential temperature. Through the effect of moist convection as ξ increases, the environmental lapse rate will relax towards a smaller moist adiabatic lapse rate, and thus enhance the static stability. An increase in tropospheric stability would curb the entrainment of free-tropospheric air into the boundary layer as given by Equation (2.4), and would, in turn, cause the CBL to shallow (N06, Wood, 2012). Furthermore, Frierson et al. (2006) found that at low ξ the troposphere essentially becomes a dry boundary layer, indicating that turbulence is increasingly restricted near the surface with increasing ξ. The implication is that low clouds could get lower if they remain coupled to the CBL. Therefore, we hypothesize that low clouds get lower in response to increases in tropospheric stability. We acknowledge that this hypothesis may be incorrect if the other terms in Equation (2.8) dominate unexpectedly. In Section 2.4.3, we will evaluate Equation 2.8 using the data from our varying-ξ experiments and compare it to the depth of the simulated boundary layer.

2.2.3 Hypothesis 3: There exist vapor-poor states with single-layer clouds

In Section 2.2.1, we hypothesized that high clouds get lower as ξ decreases (and vice versa) if they obey the basic physics behind the FAT hypothesis (Hartmann & Larson, 2002). This is in part because the cloud temperature should increase as ξ decreases. In addition, the environmental lapse rate should steadily converge on the dry adiabatic lapse rate as ξ decreases. Combining the high cloud temperature change with the lapse rate change, the implication is that high clouds should get lower with decreasing ξ. We can only expect a decrease in high cloud height with decreasing ξ up to a point: latent heat release in convective motions as $\xi \to 0$ will become negligible and here the physics behind the FAT hypothesis

breaks down. In Section 2.2.2, we hypothesized that low clouds get higher as ξ decreases (and vice versa) if the decrease in tropospheric stability (associated with the lapse rate change) facilitates more boundary layer entrainment and deepens the CBL. If both hypotheses are correct, there will be less separation between cloud layers as the atmosphere becomes more vapor-poor. Moreover, the top of the boundary layer is likely to reach the tropopause in the most vapor-poor states (Frierson et al., 2006). It follows that the high and low cloud layers could merge as the atmosphere becomes more vapor-poor. We thus hypothesize that there exist single-layer clouds in some vapor-poor states.

2.2.4 Hypothesis 4: There exist vapor-rich states with single-layer clouds

We hypothesize that increases in atmospheric moisture lead to a low cloud breakup event. In a series of papers, Popp et al. (2015, 2016) showed that the transition from an Earth-like climate with two-layer clouds to a moist greenhouse[1] climate with elevated, single-layer clouds is facilitated not only by increases in insolation but also by increases in the concentration of greenhouse gases. The climate transition is triggered by the breakup of low clouds. Here, we explore a pathway for low clouds to break up that has not been considered elsewhere: namely, if Hypothesis 2 is correct, then it follows that the LCL may eventually come to lie outside of the shallowing CBL. In this scenario, moist surface parcels no longer reach the height where they can condense, precluding cloud formation altogether. Thus, we hypothesize that the breakup of low clouds in more vapor-rich atmospheres is due to the CBL moving below the LCL.

[1]The moist greenhouse is a warm climate state found in multiple studies that is more proximal to the modern-day Earth climate than the runaway greenhouse, and within which surface liquids are thermodynamically stable and the cold trap at the tropopause is weakened, allowing water vapor to seep into the stratosphere.

2.3 Model and Method

We now test the four hypotheses in climate simulations with varying ξ. We use a version of the ECHAM6 climate model in single-column mode with modifications where water is allowed to be a major constituent (P15 Stevens et al., 2013). We run full-sky simulations at a time step of 180 s using the default setup from P15 with one exception. We include a seasonal cycle to make the control simulation as Earth-like as possible. Since our focus is on the equilibrium climate of the simulations, we temporally-average the data (unless otherwise specified) over the last 5 years to remove seasonal- and annual-biases. We leave it to future work to quantify the effect of seasonality on the simulated clouds. In the simulations, we alter the volatility of water vapor by multiplying the true SVP of water by the parameter ξ as shown in Equation (2.1).

The simulations begin in the year 2001 and are run almost 200 years. The column is located at 38°N, where the average annual insolation is equal to the global mean. The surface is a mixed layer ocean with a fixed depth of 50 m, an initial temperature of 289 K, and an albedo of 0.07. The surface temperature is determined prognostically. We use an Earth-like solar constant of 1360 W/m^2, an obliquity of 23.4 degrees, and zero eccentricity. Water vapor and cloud condensates are determined prognostically. Greenhouse gas concentrations are specified from a climatological distribution that extends from the pre-industrial to the year 2500. CO_2=550 ppmv, CH_4=1550 ppbv, N_2O=380 ppbv, CFC-11=10 pptv, and CFC-12=100 pptv have uniform volume mixing ratios; only the concentrations of CH_4 and N_2O decay above the tropopause. The concentrations cited above are reached roughly by the year 2125, and are fixed at these levels until the end of the simulation. In each simulation year, the vertical profile of O_3 is set to a monthly-averaged CMIP5 climatology of the year 2000. The atmospheric column is resolved into 95 vertical layers. Radiative transfer is carried out by the Rapid Radiative Transfer Model for General Circulation Models (RRTMG) (Iacono et al., 2008). ECHAM6 resolves the shortwave and longwave into 14 and 16 bands, respectively,

and accounts for changes in water vapor and clouds in the radiation calculation.

Cloud formation is described by a large-scale cloud scheme (Sundqvist et al., 1989). In the large-scale scheme, cloud droplet growth begins when the relative humidity exceeds a critical value (Stevens et al., 2013). Condensates are also produced by a mass-flux convection scheme (Tiedtke, 1989; Giorgetta et al., 2013; Möbis & Stevens, 2012) that parameterizes the mixing between updrafts and downdrafts with environmental air and transports heat, water vapor, and cloud condensate vertically through the column. The large-scale scheme includes the condensate detrained into the environment by the convection scheme as an additional source term (Giorgetta et al., 2013). Vertical turbulent mixing in ECHAM6 is described by a prognostic TKE scheme in which the production terms are wind shear and buoyancy (Giorgetta et al., 2013). The mixing strength is determined using K-theory coefficients that are functions of a turbulent mixing length, the static stability, and the TKE. To summarize, there are 3 separate schemes for large-scale evaporation/condensation, convection, and turbulent diffusion, each associated with their own moisture and temperature tendencies. Diabatic cooling by radiation must be balanced in equilibrium by some combination of these three processes. Our definition of radiative-convective equilibrium (RCE) requires that the temperature tendency from the convection scheme balance that from the radiative transfer scheme. RCE is satisfied in our simulations of the present-day climate (Section 2.4.1), but non-RCE states can also exist where moist convection contributes less to the atmospheric heat and moisture budget than the other two processes.

The mode of convection (i.e., shallow or deep) is determined by the strength of the large-scale moisture convergence (Möbis & Stevens, 2012). In the column model, there is no large-scale, lateral transport, so only shallow convection occurs. Following P15, we specify an entrainment rate typical for deep convection of 0.1 km^{-1} (Tiedtke, 1989) in the shallow convection scheme to facilitate the formation of deep clouds without artificially specifying the surface convergence required for deep convection. This represents only a moderate change in the entrainment rate over the range for which ECHAM6 has been tested and tuned

(Mauritsen et al., 2012).

2.4 Results

We perform simulations for the range of $0.01 \leq \xi \leq 1.85$. We use a handful of diagnostics to characterize the climate states: surface temperature; vertical cloud profiles; cloud radiative forcing (CRF), defined as the difference between the full-sky and inferred cloud-free radiative fluxes at the top of the atmosphere; and vertically-integrated relative humidity (RH),

$$\langle RH \rangle = \frac{\int_{p_1}^{p_2} RH \, dp}{\int_{p_1}^{p_2} dp}, \tag{2.9}$$

where the brackets denote a pressure-weighted average and p_1 and p_2 are the pressure values at the boundaries of the atmospheric layer under consideration. The inferred cloud-free radiative fluxes used in determining the CRF at each model time step of the full-sky simulations are obtained, in practice, by making the clouds transparent in a separate radiation calculation.

Figure 2.1 shows the simulated cloudy climate states as ξ is varied. Climate states with similar patterns of cloud formation are classified as a group. These groupings are G1, G2, and G3 and correspond respectively to $0.01 \leq \xi \leq 0.14$, $0.16 \leq \xi \leq 1.63$, and $1.65 \leq \xi \leq 1.85$. Our description of G3 will be brief, as it is the subject of a companion work. The terms "low clouds" and "high clouds" pertain only to Earth-like states with two-layer clouds (i.e., G2).

2.4.1 The G2 climate

G2 extends through most of our parameter space, representing a continuum of vapor-poor and vapor-rich states with two-layer clouds (Figure 2.1a,b) that have a negative net CRF (Figure 2.2) and therefore cool the surface relative to a cloud-free atmosphere. G2 states are the most Earth-like and indeed most G2 states ($0.5 \leq \xi \leq 1.63$) are in RCE (Figure 2.3a). The G2 low clouds are similar to cumulus clouds on the basis that their cloud fraction is

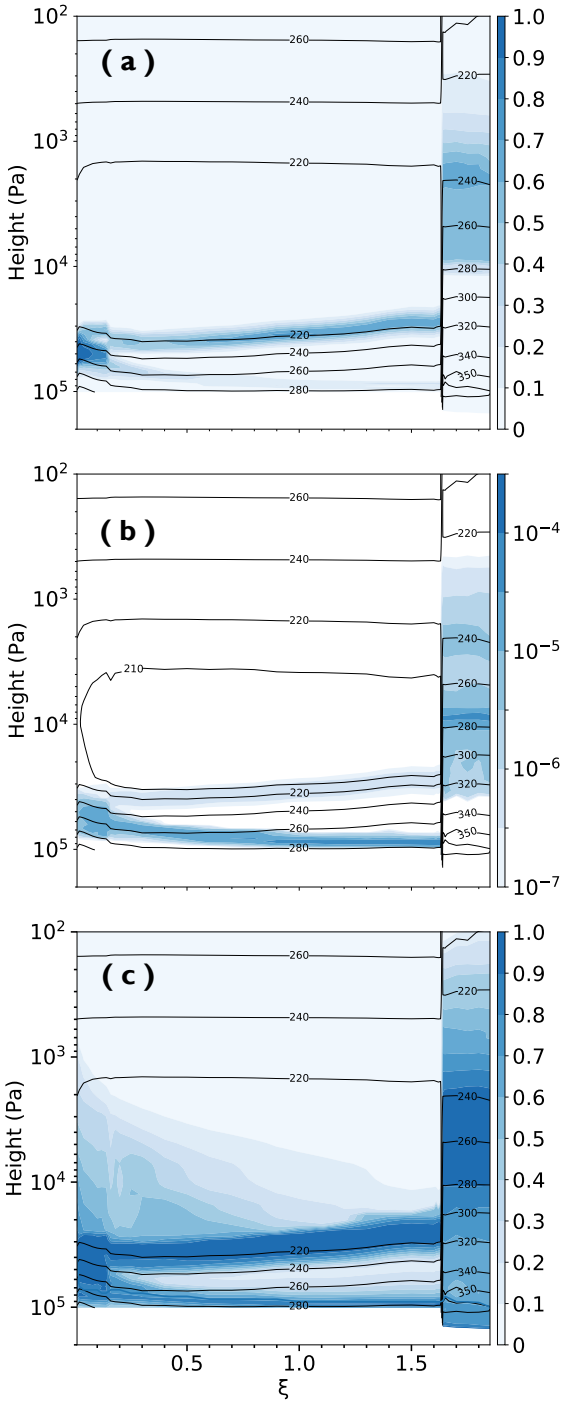

Figure 2.1: Vertical profiles of (a) fractional cloud cover, (b) cloud condensate density in kgm^{-3}, and (c) relative humidity. All variables are given as an average over the last 5 years of the simulation (this statement applies to all plots in the paper, unless otherwise specified). Vertical axis is total pressure. Black contours denote temperature.

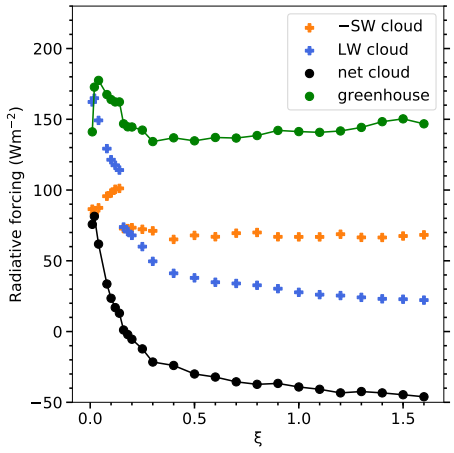

Figure 2.2: Longwave (LW), Shortwave (SW), and Net Cloud Radiative Forcing (CRF). The CRF is calculated as the difference between the cloudy and inferred clear-sky radiative fluxes at the top of the atmosphere. The clear-sky greenhouse forcing is calculated as the difference between the inferred clear-sky OLR and the surface emission.

$\sim$20% (Figure 2.3c) and the longwave flux divergence (LFD) at their cloud-tops is typically several 10s of Wm^{-2} less than the surface latent heat flux (LHF) (Figure 2.4a,b), suggesting that these low clouds are generally maintained by turbulence from surface heating rather than cloud top cooling (Figure 2.5).

Across G2, the column water vapor increases from 0.2 cm to 2 cm (Figure 2.6a). Remarkably, the column relative humidity ($\langle RH \rangle = 65\%$), the albedo ($\alpha = 0.31$) and the surface temperature ($T_s = 290$ K) are mostly invariant as ξ increases over the subset of G2 states in RCE (Figures 2.3a, 2.6, and 2.7). One naturally wonders whether the tendency of RCE states to maintain fixed $\langle RH \rangle$, α, and T_s as moisture increases is because ECHAM6 is tuned to reproduce Earth's modern-day climate. If this behavior is observed in simulations with another climate model, it would point to robustness. We leave this to future work. For now, we offer a brief explanation for each invariant property of the G2 climate. First, the boundary layer is more humid than the free troposphere (Figure 2.7), and this vertical contrast in relative humidity becomes more pronounced with increasing ξ. Based on Figure 2.7,

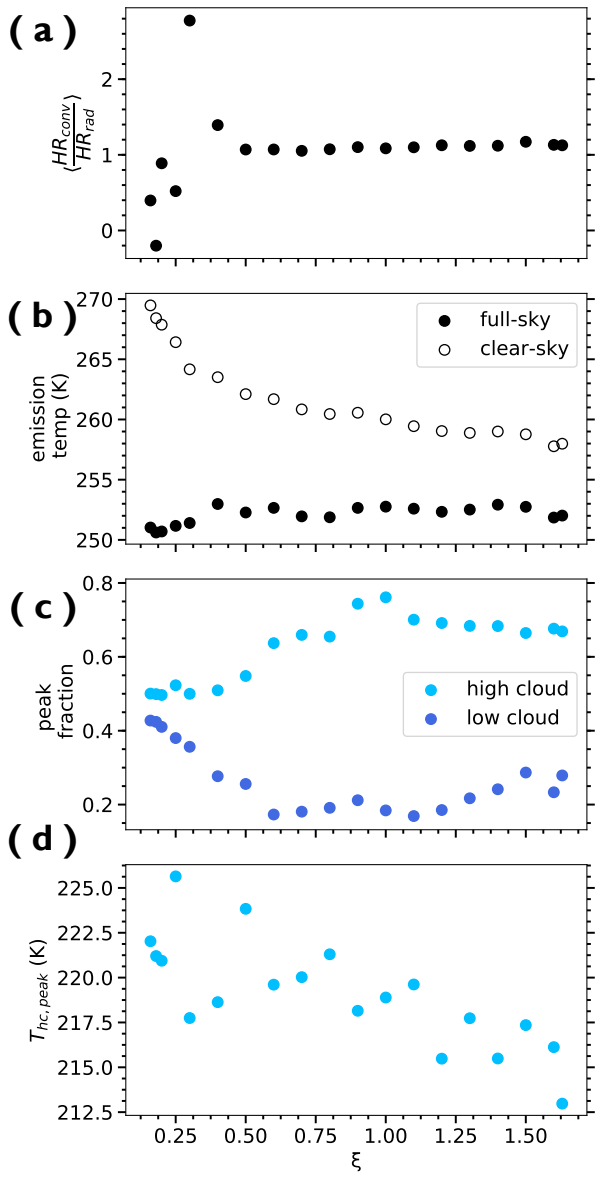

Figure 2.3: (a) Pressure-weighted average of the ratio of the convective heating rate (HR_{conv}) to the radiative heating rate (HR_{rad}) both in units of K/day taken over the free troposphere. HR_{conv} is the temperature tendency from the convection scheme. By definition, RCE states possess a value of 1. (b) Full-sky and clear-sky emission temperature. The latter is inferred from the full-sky simulations in which clouds are made transparent in a separate radiation calculation. (c) Peak fraction of high and low clouds. (d) Temperature at the peak high cloud fraction, $T_{hc,peak}$.

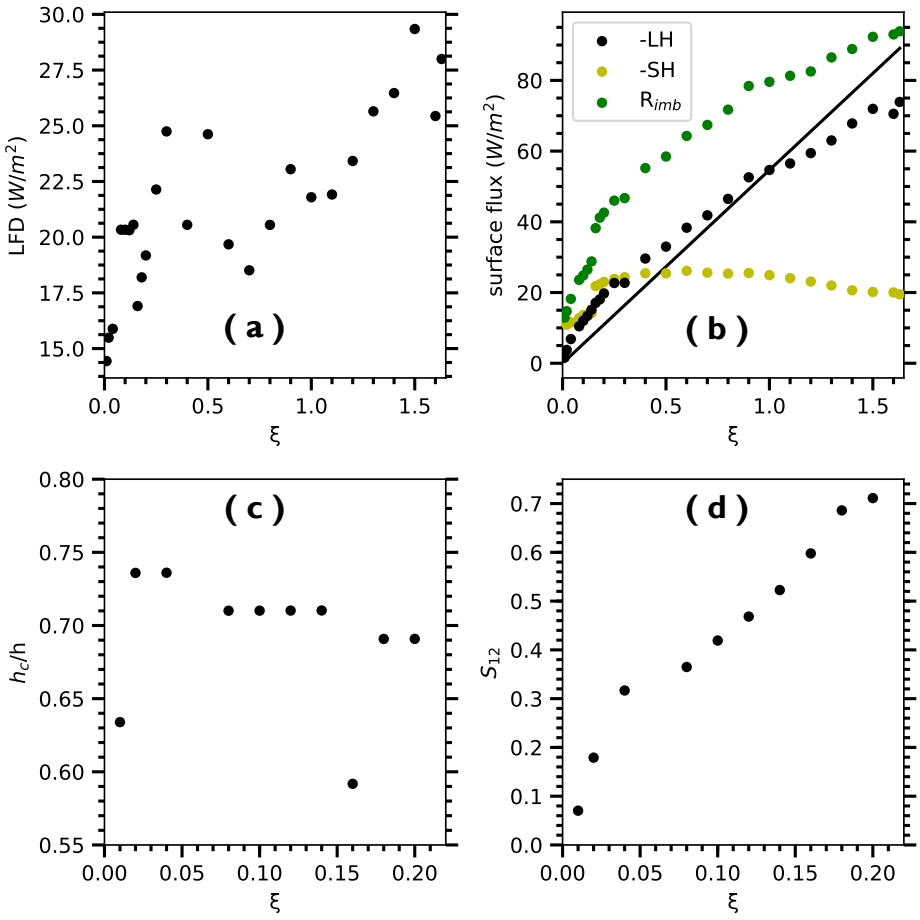

Figure 2.4: (a) Longwave flux divergence (LFD) at the cloud top, (b) surface latent heat flux (black), sensible heat flux (yellow), and net radiative imbalance (green), (c) ratio of cloud thickness h_c to cloud top height h, and Sc instability parameter S_{12}. Note the x-axis is different in each row. In (a), the values in G2 are from the *low* cloud top. The line in (b) is $y = \xi\text{LHF}(\xi{=}1)$. Figure adapted from S19.

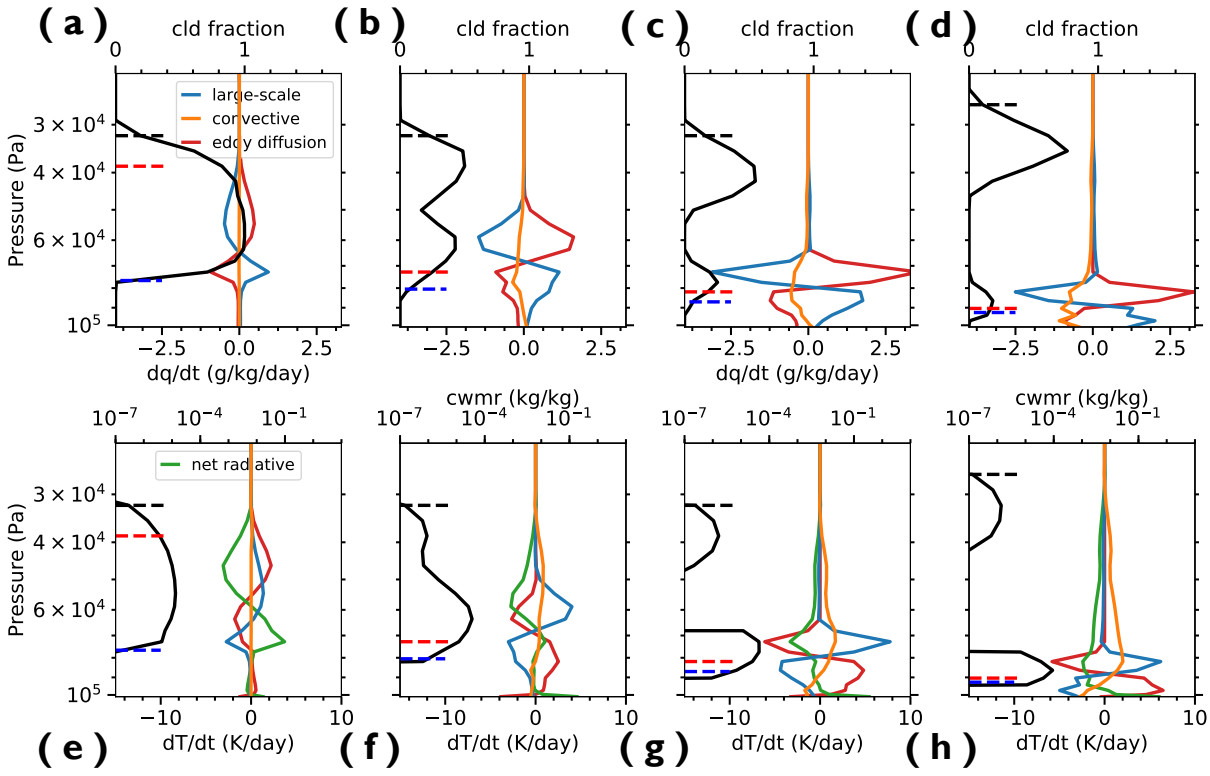

Figure 2.5: Top row: moisture tendencies in color and cloud fraction in black. Bottom row: temperature tendencies in color and cloud water mixing ratio (cwmr) in black. Profiles correspond, left-to-right, to (a, e) $\xi = 0.01$, (b, f) $\xi = 0.16$, (c, g) $\xi = 0.5$, and (d, h) $\xi = 1.0$. Horizontal dashed lines on the left margins correspond to heights of the radiative tropopause (black), boundary layer (red), and lifting condensation level (blue).

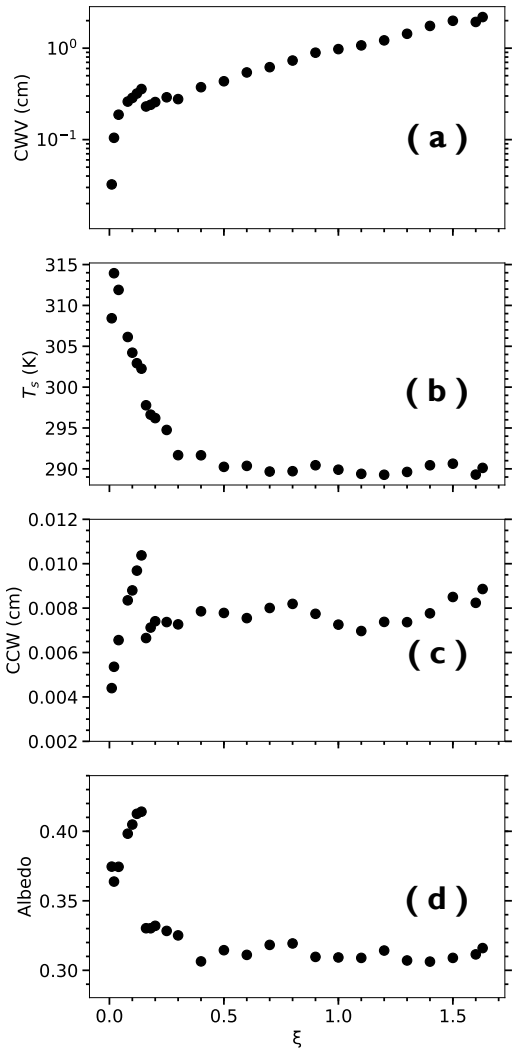

Figure 2.6: (a) Column water vapor (CWV), (b) surface temperature T_s, (c) column cloud water (CCW), and (d) albedo. Albedo is computed as the ratio of upwelling shortwave over downwelling shortwave at the top of the atmosphere.

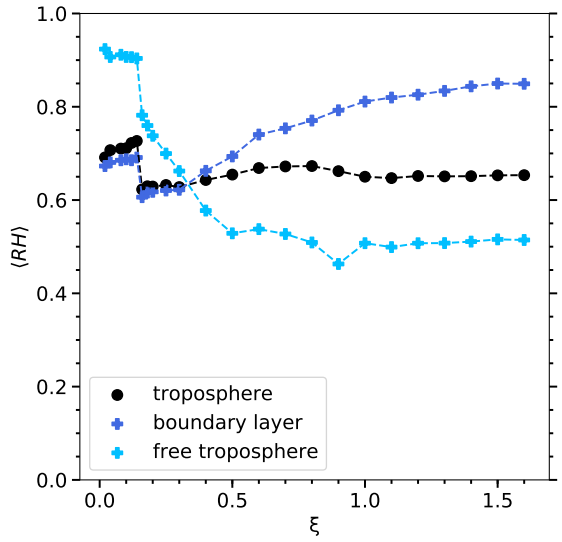

Figure 2.7: Column-integrated relative humidity, $\langle RH \rangle$, of the troposphere (black), boundary layer (dark blue), and free troposphere (light blue). Variables calculated using Equation (2.9).

a consistent interpretation of the constant $\langle RH \rangle$ in G2 is the cancellation of a deeper and drier free troposphere and a thinner, wetter boundary layer. Second, α is constant because the SW cloud forcing is constant (Figure 2.2), which can be traced back to relatively small variations in column cloud water and low cloud peak fraction (Figures 2.3c and 2.6c). Third, over the range of ξ where T_s is roughly invariant, the magnitude of the change in the clear-sky greenhouse forcing and the net CRF are equal ($\sim$15 Wm^2) and opposite (Figure 2.2), and thus cancel out. G2 clouds cool more with increasing ξ because the high clouds warm *less* (Figure 2.2). Figure 2.3b shows that high clouds warm less because the clear-sky emission temperature drops, presumably from an increase in the infrared opacity of the atmosphere below the high clouds.

Not all properties of G2 climate are invariant, however. We find that the lapse rate decreases following the moist adiabat up from the lifting-condensation level (Figure 2.8), low clouds get lower and high clouds get higher (Figure 2.1a,b), and the height of the boundary

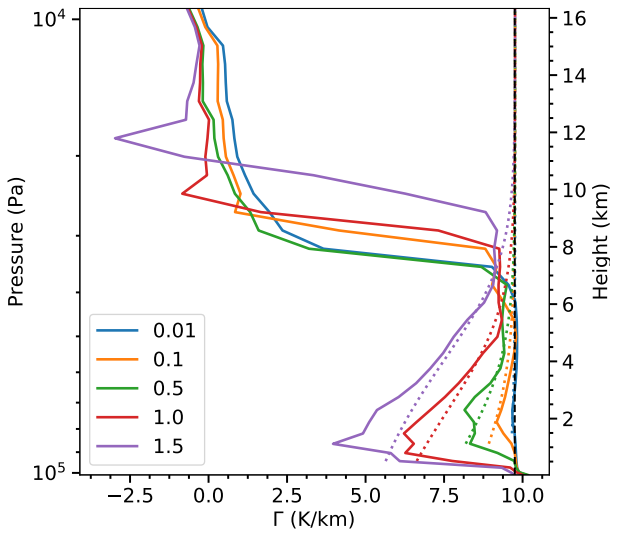

Figure 2.8: Lapse rate (Γ) as a function of height for a range of ξ. Dotted lines give the respective moist adiabatic lapse rate from the lifting-condensation level (Romps, 2017). For reference, the dry adiabatic lapse rate is plotted as a dashed black line.

layer decreases between $\xi = 0.16$ and $\xi = 1.0$ but levels out between $\xi = 1.0$ and $\xi = 1.63$ (Figure 2.9a).

Water vapor, and its relative humidity (RH) in particular, governs the presence of two-layered clouds in the G2 states. In a convecting column, the RH has a "C-shaped" profile with local maxima at the outflow level and near the surface and low RH between. The mid-tropospheric RH minimum in the Earth's tropics is a consequence of environmental subsidence that balances outflow of detraining plumes at their equilibrium level, which is in competition with detrainment of moist plumes in the middle troposphere (Romps, 2014). Note that this process is captured in entraining/detraining plume models of convection, in which case the relevant physics of upwelling plumes and environmental air is modeled in a single column, albeit as a parameterization (e.g., Tiedtke, 1989). As a test of convection-controlled, C-shaped RH profile, we performed full-sky simulations with convection turned off, such that moisture is only affected by turbulent diffusion and condensation. This mechanism-denial

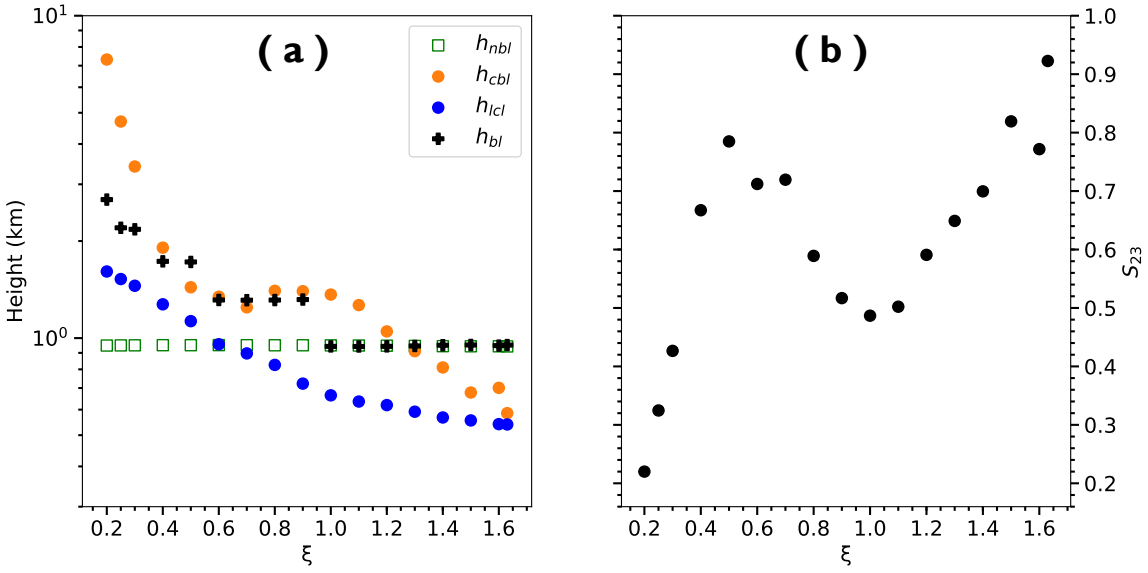

Figure 2.9: (a) Estimated equilibrium convective boundary layer height (orange dots) and neutral boundary layer height (square). Plus-signs (+) mark the actual boundary layer height. The height of the lifting condensation level (blue dots) is determined analytically (Romps, 2017). (b) Low cloud instability parameter S_{23}, calculated from the data in (a) with Equation (2.16).

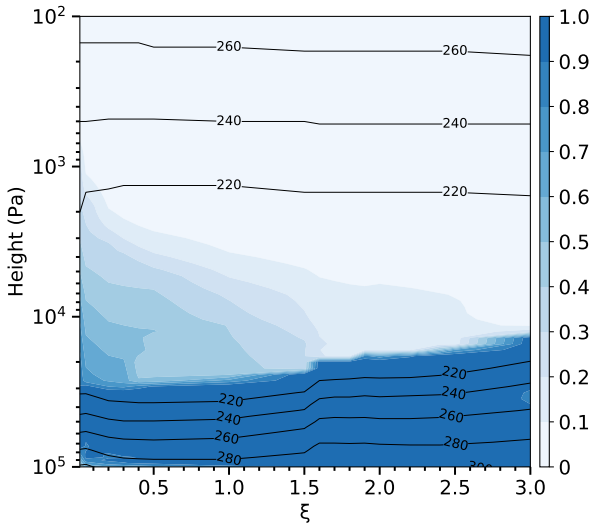

Figure 2.10: Vertical profile of relative humidity in full-sky simulations where convection is disabled. Vertical axis is total pressure. Black contours denote temperature.

experiment clearly lacks the mid-tropospheric RH minimum that is characteristic of the C-shaped profile (Figure 2.10). Clouds are present in these full-sky simulations, but they no longer have distinct layers. We thus confirm that drying of the mid-troposphere requires convection to induce environmental subsidence[2], as analytically shown by Romps (2014).

2.4.2 Evaluating Hypothesis 1: how high clouds get higher

In Section 2.2.1, we predicted that increasing ξ should cause high clouds to rise and cool. We also predicted from a theory of radiative transfer that the vapor pressure path (VPP) where high clouds form and longwave cooling rates decrease would take on a characteristic value of 1.2×10^4 PaPa$_v$. Here, we evaluate those predictions, focusing on the location of the cloud maximum ("cloud level").

[2]In a higher dimensional model like a GCM, large-scale downwelling and/or horizontal advection of air masses could also produce local minima in the vertical profile of RH.

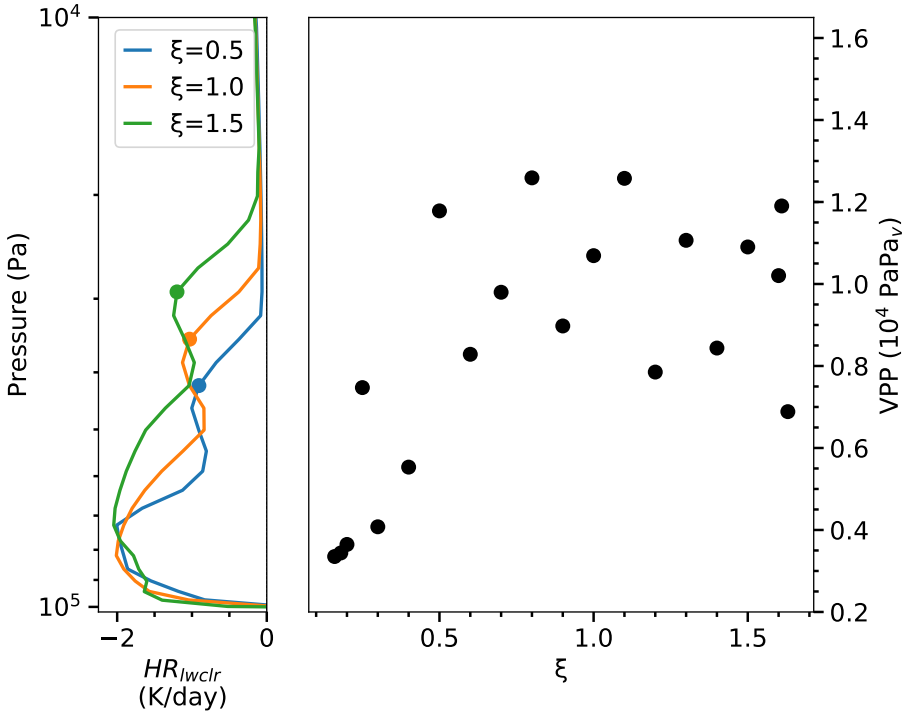

Figure 2.11: (a) Clear-sky longwave heating rate (HR_{lwclr}) in K/day and (b) vapor pressure path (VPP) in $PaPa_v$ between the top of the atmosphere and cloud level for a range of ξ. The heating rates at cloud level are marked by dots in (a).

Most G2 states ($0.5 \leq \xi \leq 1.63$) are in RCE (Figure 2.3a), and in RCE one generally expects the physics of FAT to hold (Hartmann & Larson, 2002). We thus restrict our analysis to the subset of G2 states in RCE. Figure 2.8 demonstrates that the lapse rate decreases as expected, relaxing towards the decreasing moist adiabatic lapse rate with increasing ξ. Figure 2.3d shows that the high cloud temperature decreases by 11 K. Is this quantitatively consistent with our ξ-modified FAT hypothesis? A crude estimate for the change in cloud temperature is obtained from a Taylor expansion of the Clausius-Clapeyron relation as:

$$\Delta T \approx (\xi - 1)\frac{R_v}{L_{hc}} T_{hc,\xi=1}^2, \tag{2.10}$$

where R_v is the specific gas constant of water, $T_{hc,\xi=1} = 219$ K is the cloud temperature at $\xi = 1$, and L_{hc} is the enthalpy of vaporization at 200 hPa. Evaluating Equation (2.10) from $\xi = 0.5$ to $\xi = 1.63$, a combined ΔT of $\approx$-11 K would fix the SVP at cloud level. This estimate matches the actual temperature change in Figure 2.3d. A reasonable conclusion is that the decrease in cloud temperature required by the physics of FAT coordinates with a decrease in the lapse rate to produce an upward shift of the high cloud, as observed in Figure 2.11a.

The upward shift of the high cloud is consistent with the connection between clear-sky longwave cooling and high cloud formation (JF20b). In Figure 2.11a, the cloud maximum is located in between a mid-tropospheric region where the clear-sky longwave cooling rate is relatively uniform and an upper-tropospheric region where the cooling rate drops towards zero. In general, increasing ξ causes the cooling rate above the lower troposphere to increase at each height (Figure 2.11a). Figure 2.11b shows that the vapor pressure path (VPP) between the top-of-atmosphere and cloud level is $\approx 10^4$ PaPa$_v$ in the RCE G2 states. The VPP varies by many orders of magnitude between the radiative tropopause ($\sim 10^3$) and the surface ($\sim 10^6 - 10^7$), so it is noteworthy that the upper-tropospheric decrease in longwave cooling occurs so close to its theoretically predicted value. The link between decreases in radiative cooling and cloud height in RCE is therefore supported by the data in Figure 2.11.

Our observation of a roughly uniform VPP between the top-of-atmosphere and cloud

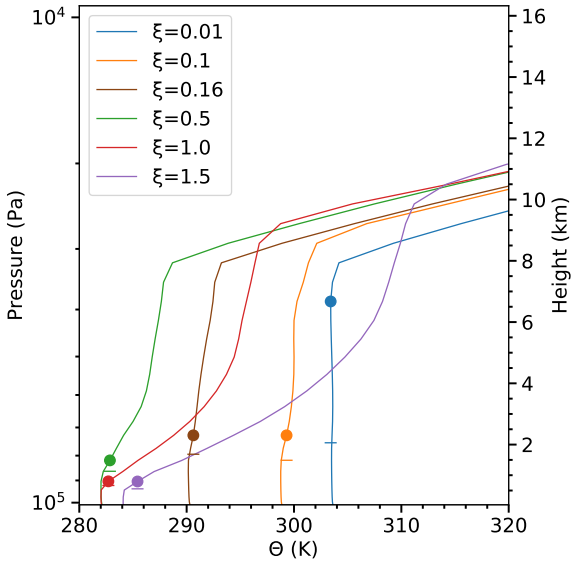

Figure 2.12: Vertical profile of potential temperature (solid lines), boundary layer height (circles), and lifting-condensation level (horizontal ticks) for a range of ξ.

level in experiments that vary the SVP is perhaps the clearest demonstration to date in a numerical model of the key result of JF20b that the spectral properties of water vapor control the decrease in radiative cooling and thereby the cloud height. It would be desirable to test these ideas further in CRM simulations where the relevant physics are treated with greater fidelity than our 1D climate model.

2.4.3 Evaluating Hypothesis 2: how the height of the cloud-topped boundary layer decreases

In Section 2.2.2, we hypothesized that low clouds get lower because the height of the cloud-topped convective boundary layer (CBL) decreases as the tropospheric stability increases with increasing ξ. Here, we test that hypothesis.

Figure 2.5 shows that turbulent diffusion mixes heat and moisture in the G2 boundary layers and couples the low clouds to the surface. There are two fundamental sources of

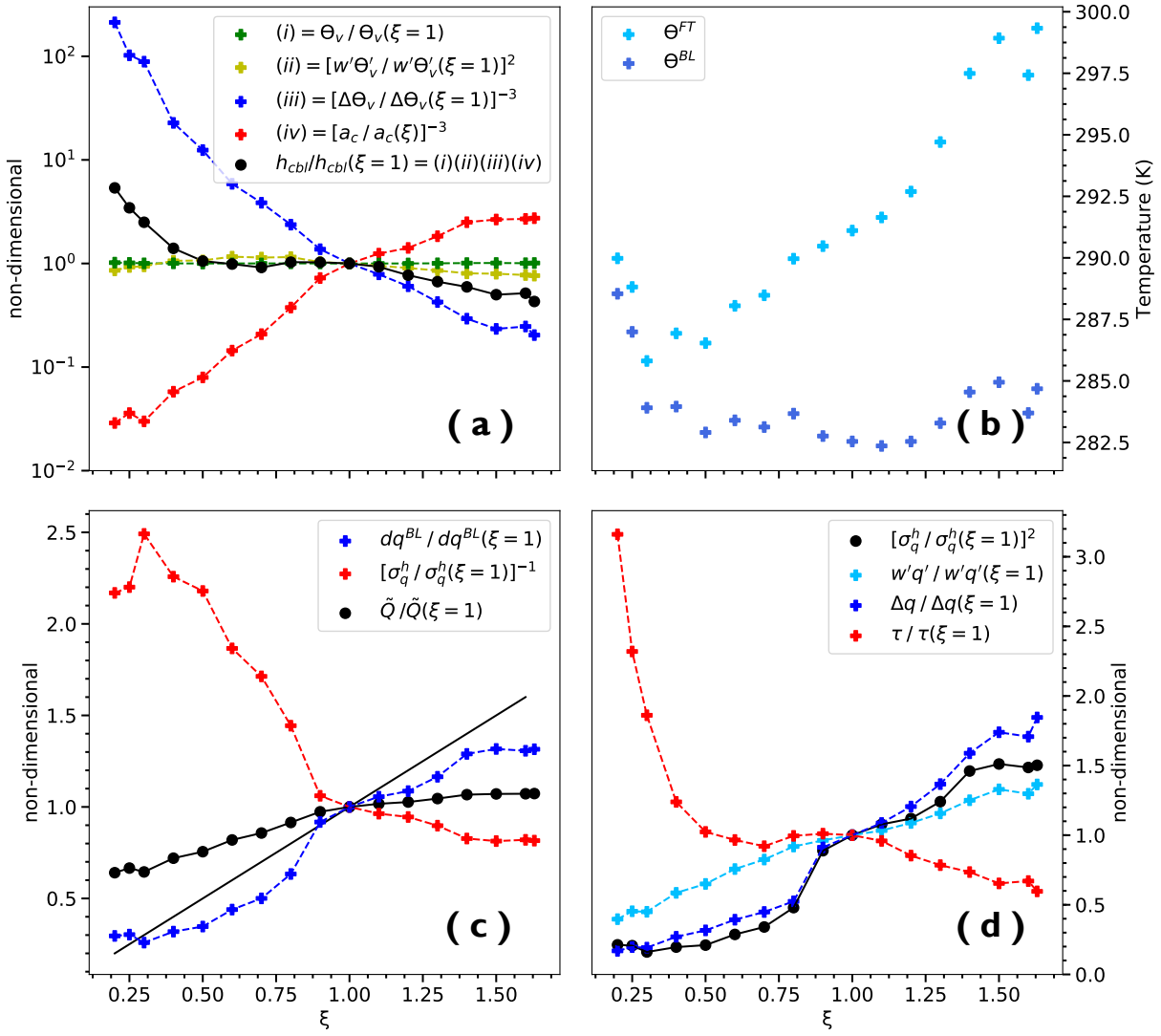

Figure 2.13: (a) Key terms from Equation (2.8) normalized by their value at $\xi = 1$. (b) Average potential temperature of the free troposphere Θ^{FT} and boundary layer Θ^{BL}, respectively, from Equation (2.6b). (c) Key terms from Equation (2.12) normalized by their value at $\xi = 1$. The black line in (c) is y = ξ. (d) Key terms from Equation (2.14) normalized by their value at $\xi = 1$. See the text for more details.

turbulence in any boundary layer: buoyancy and wind shear. Note that the vertical wind shear in the single-column model is predetermined and does not vary between experiments. The boundary layer height in ECHAM6 (h_{bl}) is set to be the largest of the convective boundary layer (CBL) and the neutral boundary layer (NBL), $h_{bl} = \max(h_{cbl}, h_{nbl})$ (Stevens et al., 2013). The NBL is synonymous with the Ekman layer, which is always present on a rotating planet and where frictional dissipation of winds at the surface combines with Coriolis acceleration to aid in vertical mixing (Stull, 1988). By estimating the depth of each boundary layer type, h_{cbl} and h_{nbl}, and comparing it to h_{bl}, we will show why h_{bl} drops when $\xi < 1$ and levels out when $\xi > 1$ (Figure 2.9a).

h_{nbl} is the height where the effect of surface friction on the flow becomes negligible, which we estimate (Stevens et al., 2013; Stull, 1988; Arya, 1988),

$$h_{nbl} = 0.3\frac{u^*}{f}. \tag{2.11}$$

This height primarily depends on the friction velocity $u^* = \sqrt{C_D}U$, where U is the prescribed wind speed above the surface and C_D is a momentum transfer coefficient, and the Coriolis parameter f. In Figure 2.9a, we show h_{nbl} evaluated with a typical roughness length for a calm ocean surface of 1 mm, a wind speed of 6 m/s at a height of 10 m, and the Coriolis parameter corresponding to Earth's rotation rate at a latitude of 38°N. Both h_{nbl} and h_{bl} are approximately fixed at a height of 1 km when $\xi \geq 1$ (Figure 2.9a), indicating that shear- rather than buoyancy-driven turbulence is deeper in the vapor-rich G2 states.

h_{cbl} represents the maximum height reached by positively-buoyant eddies rising from the surface (Equation (2.8)). Estimating h_{cbl} requires information about the bulk thermodynamic state of the boundary layer and free troposphere in G2. Pressure-weighted averages are carried out over two atmospheric slabs corresponding to 1000-700 hPa and 700-400 hPa when $\xi < 0.9$ and 1000-850 hPa and 850-400 hPa when $\xi \geq 0.9$, which is found to give the best agreement between h_{cbl} and h_{bl}. Both are plotted in Figure 2.9a. To understand why h_{cbl} decreases over G2, we normalize each term on the RHS of Equation (2.8) by their reference value at $\xi = 1$. The non-dimensionalized terms are

$$(i) \quad \Theta_v|_s \,/\, \Theta_v|_s(\xi{=}1),$$

$$(ii) \quad [\overline{w'\Theta'_v}|_s \,/\, \overline{w'\Theta'_v}|_s(\xi{=}1)]^2,$$

$$(iii) \quad [\Delta\Theta_v \,/\, \Delta\Theta_v(\xi{=}1)]^{-3},$$

$$\text{and } (iv) \quad [a_c \,/\, a_c(\xi{=}1)]^{-3}.$$

Terms (i)-(iv) are plotted in Figure 2.13a, revealing that a partial cancellation between (iii) and (iv) mostly explains the change in h_{cbl}. The decrease in (iii) is facilitated by the decrease in the lapse rate (Figure 2.8), which causes the potential temperature in the free troposphere to increase more rapidly than in the boundary layer (Figure 2.13b). The increase in (iv) can be understood from Equation (2.12), which is an empirical fit to LES experiments of cloud-topped mixed layers (Cuijpers & Duynkerke, 1993):

$$a_c = 0.5 + 0.36 \tan^{-1}\left(1.55\,\tilde{Q}\right). \tag{2.12}$$

Equation (2.12) diagnoses the (moist) convective area fraction as a function of a single parameter, the normalized saturation deficit (Cuijpers & Bechtold, 1995)

$$\tilde{Q} = \frac{dq^{BL}}{\sigma_q^h}, \tag{2.13}$$

where $dq^{BL} = q^{BL} - q_{sat}^{BL}$ is the boundary layer saturation deficit and σ_q^h (Equation 2.14) is the square root of the moisture variance at the top of the boundary layer. $\tilde{Q}$ is a statistical measure of the potential for turbulent moisture fluctuations at the top of the boundary layer to meet the requirements for latent heat release. More negative values of $\tilde{Q}$ indicate that moisture fluctuations, σ_q^h, are less likely to overcome the boundary layer saturation deficit. We evaluate Equation (2.13) over G2 and find that increasing ξ causes $\tilde{Q}$ to become more negative. To understand why, we normalize each term in Equation (2.13) by their value at $\xi = 1$, and plot the result in Figure 2.13c. The moisture variance at the top of the boundary layer (Neggers et al., 2006, 2007),

$$(\sigma_q^h)^2 = \overline{w'q'}\frac{\Delta q}{\Delta z}\tau, \tag{2.14}$$

is the product of three parts: the absolute moisture gradient across it ($\Delta q \uparrow$ as $\xi \uparrow$), the eddy moisture flux from the surface ($\overline{w'q'} \uparrow$ as $\xi \uparrow$), and the large-eddy turnover timescale ($\tau = \frac{h_{cbl}}{w^*} \downarrow$ as $\xi \uparrow$) (Figure 2.13d). Ultimately, increasing ξ amplifies σ_q^h (Figure 2.13c). However, this amplification of σ_q^h is insufficient to close the widening saturation deficit, dq^{BL}. Why does increasing ξ widen the saturation deficit (Figure 2.13c)? Consider a perturbation scenario where ξ is increased in a parcel of BL air initially at $\xi = 1$ while its RH and temperature are conserved. The specific humidity of the parcel must increase and after the perturbation is given by $q = \xi q^*$ where $q^* = \mathrm{RH} q^*_{sat}$. The parcel's "distance" from saturation is increased from $dq^* = q^* - q^*_{sat}$ (before the perturbation) to $dq = q - q_{sat} = \xi dq^*$ (after the perturbation). If this scenario applied, on the whole, to the boundary layer in our experiments, $dq^{BL}/dq^{BL}(\xi = 1)$ would vary linearly with ξ. This is found roughly to be the case in Figure 2.13c, even though the requirements (that would align the experiments with this hypothetical scenario) of fixed RH and temperature do not strictly hold. Therefore, $\tilde{Q}$ becomes more negative as SVP increases (Figure 2.13c) because the saturation deficit grows faster than the moisture fluctuations at the top of the boundary layer, fewer rising thermals meet the requirements for latent heat release, and (*iv*) increases (Figure 2.13a).

Summarizing this result, the decrease in h_{cbl} is driven by the dependence of the thermodynamic variables, T and q, on ξ. T depends on ξ because moist convection mixes along the moist adiabat, so increasing moisture reduces the vertical gradient in temperature and (*iii*) in turn. (*iv*) increases because the mean-state saturation deficit increases faster than the moisture fluctuations at the top of the boundary layer. (*iii*) and (*iv*) have opposite effects on the height of the CBL, so an increase in tropospheric stability ultimately drives the decrease in h_{cbl}.

Assembling all the pieces, we have a consistent story for why low clouds get lower. Low clouds get lower because they are coupled to the height of the CBL. Increases in tropospheric static stability ($\Delta\Theta_v$) are the primary driver of the decrease in h_{cbl} (as ξ increases, the vertical length scale of buoyancy-driven turbulence decreases). An important correction to

Hypothesis 2 is that low clouds get lower only when the deepest mixing occurs through buoyancy- rather than shear-driven turbulence as ξ increases. Indeed, low clouds level out when $h_{nbl} > h_{cbl}$.

2.4.4 The G1 climate

G1 is a vapor-poor, warm and humid regime with single-layer clouds that stretch from 800 to 300 hPa. The phenomenology of the G1 cloud supports an analogy to unbroken Sc clouds under an inversion. Peak cloud fraction decreases from 100% to 80% over G1 (e.g., Figure 2.1a), values that are 20-40% greater than the extensive Sc that form off the western coast of Earth's continents (Wood, 2012) but comparable to the coverage observed in limited-domain CRM simulations of Sc (Tan et al., 2017; Schneider et al., 2019) over SSTs of 290 K. The longwave flux divergence (LFD) at the cloud top in units of Wm^{-2} is larger than surface latent heat fluxes (LHF) (Figure 2.4a,b), resembling a Sc-like regime where buoyancy fluxes at the cloud top rather than at the surface are most important to the production of boundary layer turbulence. Unlike Sc on Earth, the G1 cloud spans most of the troposphere so that the cloud top rests under a resolved (stratospheric) temperature inversion. In addition, the G1 cloud warms, rather than cools, the climate, producing surface temperatures as high as 315 K (Figure 2.6b). How is this possible? The free troposphere has higher RH than the boundary layer in this regime (Figure 2.7), and this produces a thick, quasi-permanent cloud that cools to space in the upper troposphere (Figure 2.5e). As ξ decreases, the environmental lapse rate converges on the dry adiabatic lapse rate, thus maximizing the temperature contrast across the cloud. With these factors combined, the G1 cloud generates a LW CRF that greatly exceeds its SW CRF. This is somewhat surprising because G1 states have about a 30% higher albedo than G2 states (Figure 2.6d). The fact that both G1 and G2 have similar amounts of column-integrated cloud water (Figure 2.6c) but the G2 low cloud fraction is up to 75% lower (Figure 2.5 and 2.3c) likely explains the overall difference in albedo.

In Figure 2.5a,e, we show the cloud fraction, cloud water mixing ratio, and temperature

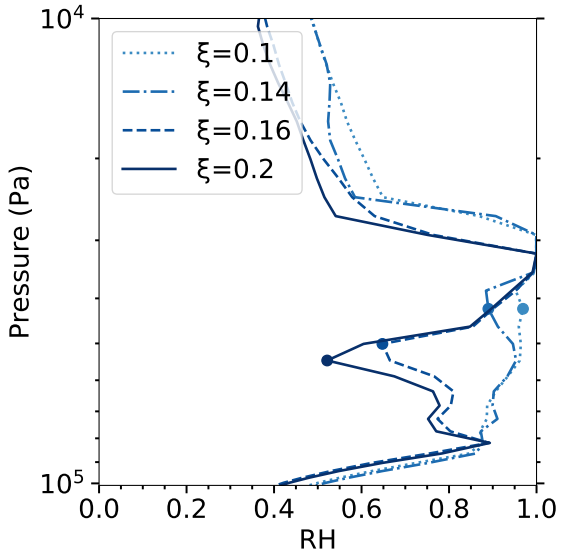

Figure 2.14: Profiles of relative humidity across the G1 to G2 transition for $\xi = 0.1, 0.14, 0.16, 0.2$. Filled circles correspond to the location where the positive diffusive moisture tendency (as in Figure 2.5) moving upwards goes to zero.

and moisture tendencies for the end-member G1 state, $\xi = 0.01$. Interestingly, convection contributes little to the atmospheric heat and moisture budget relative to diffusive and large-scale processes. A consistent interpretation is as follows. Radiative cooling at the cloud top facilitates large-scale condensation that is communicated to lower layers through re-evaporation, radiative heating balances the evaporative cooling, and boundary layer diffusion resupplies the precipitated moisture. Radiative cooling raises the upper-tropospheric RH, triggering cloud formation through large-scale condensation. Lower-tropospheric radiative heating is the result of a cloud greenhouse effect and keeps the air there sub-saturated.

2.4.5 Evaluating Hypothesis 3: how single-layer G1 clouds break up

In Section 2.2.3, we hypothesized that there exist vapor-poor states where there is no vertical separation between cloud layers. This hypothesis emerges intuitively from the prediction that

low clouds get higher and high clouds get lower as the moisture content of the atmosphere is reduced. Here, we test that hypothesis through analysis of the simulations and show that the transition from single-layer to two-layer clouds can be interpreted through a cloud instability parameter.

Figures 2.5 and 2.14 tell most of the story. To aid our description, we define two distinct mixing layers. The "diffusive layer" and "convective layer" extend from the surface and the LCL, respectively, to the height where their respective moisture and temperature tendencies in Figure 2.5 drop to zero. In G1, the diffusive and convective mixing layers overlap. As ξ increases, the shallowing diffusive layer separates from the convective layer which continues to top out at the radiative tropopause (Figure 2.5f-h). An important consequence of this separation is that control over the heat and moisture budget of the upper troposphere shifts to moist convection. The competition between convective detrainment and environmental subsidence in this region produces a RH minimum that first emerges around 400 hPa at $\xi = 0.14$ and then descends (Figure 2.14), tracking the separation level. When the upper troposphere becomes decoupled from surface turbulence, moist convection maintains a thin high cloud by transporting condensed water into this region.

In Section 2.4.3 and 2.4.1, we extended an analogy between G1 clouds, G2 low clouds, and two different types of boundary layer clouds on Earth, Sc and Cu, respectively. Is G1 to G2 an Sc to Cu transition? To determine whether this is the case, we evaluate a Sc instability parameter, here denoted S_{12}, adapted from Bretherton & Wyant (1997, henceforth, BW97) that represents the minimum requirements for the decoupling of a Sc cloud from the surface.

$$S_{12} = \frac{\text{LHF}}{\text{LFD}} \frac{h_c}{h}, \tag{2.15}$$

where h_c is the cloud thickness and h is the height of the cloud top. Entrainment (a process that mixes dry air downward and moist air upwards) dries the cloud layer in an absolute sense. Radiative cooling at the top of Sc clouds causes air to be negatively buoyant, driving a turbulent circulation within the boundary layer that resupplies moisture to the cloud. In BW97's minimal model of a non-precipitating Sc deck, entrainment warming and radiative

cooling balances the energy budget while entrainment drying and convective moistening (proportional to the surface LHF) balances the moisture budget.

BW97 predict that Sc clouds risk decoupling from the surface and breaking up when $S_{12} > 0.55$, and this was reproduced in LES simulations by Schneider et al. (2019, henceforth, S19). To calculate the LFD in Wm^{-2} (Figure 2.4a), we take the peak longwave heating rate in Wm^{-3} at the cloud top and then multiply this peak value by the average distance (500 m due to numerical resolution) between the cloud top and the next vertical level. Following S19, we assume the cloud base is where the fractional cloudiness goes above 5%. S_{12} increases between $\xi = 0.01$ and $\xi = 0.14$ because the surface LHF increases five-fold (500% increase) from 3-15 Wm^{-2}, the cloud-top LFD increases by 40% from 14 to 20 Wm^{-2}, and $\frac{h_c}{h}$ varies by 14% (Figure 2.4). A theoretical prediction for the change in LHF with increasing ξ is given in Figure 2.4d using the bulk-aerodynamic formula for LHF where RH and T at the surface are fixed. The theoretical prediction agrees reasonably well with the actual change in the LHF. Judging by Figure 2.4d, the G1 cloud splits when $S_{12} \approx 0.55$ (or equivalently $0.14 < \xi < 0.16$). We conclude that the instability parameter predicts when the G1 cloud splits in our simulations, lending support to the idea that G1 to G2 is an Sc to Cu transition.

S19 increased CO_2 concentrations in LES simulations of Sc clouds, and found that all terms in Equation (2.15) play a relatively important role in driving S_{12} sufficiently high that the cloud deck becomes unstable. In this study, we vary water vapor and find that the quasi-linear dependence of the surface LHF on ξ is by far the dominant factor destabilizing the G1 cloud. Interestingly, our result is qualitatively similar to BW97's LES experiments where, instead, increasing SSTs caused the surface LHF to increase by a factor of 5. We find a 50% reduction in maximum cloud fraction from 0.8 to 0.4 crossing from G1 and G2 (or a 75% reduction from 1.0 to 0.25 if comparing the driest G1 state to the low cloud in the wettest G2 state). The liquid water path decreases as the G1 cloud breaks up in our simulations (Figure 2.6c), which we attribute a reduction in cloud water content due to mid-tropospheric subsidence drying (Figure 2.5e,f) and less efficient transport of moisture

by convection relative to turbulent diffusion. Contrary to what one would expect from a Sc to Cu transition, the temperature change across the transition is negative. The G1 cloud deck has a positive net CRF so that when it breaks up the cloud warming effect is *diminished* and the surface temperature *decreases*.

In summary, our simulations confirm Hypothesis 3: that vapor-poor states have a single- rather than double-layer cloud structure. We conclude that the effect of increasing ξ is to reduce the influence of turbulent diffusion in the troposphere from the top down, handing off the role of cloud formation in this region to moist convection through its well-studied effect on the moisture budget (Romps, 2014). As the diffusive mixing layer shallows with increasing ξ and separates from the convective mixing layer, moist convection produces a RH minimum at the separation level and maintains a thin high cloud at its top. The G1 cloud fractures when it meets the minimum requirements for a Sc deck to decouple from the surface (BW97). The breakup of this surface-warming cloud generates a sharp, 5 K *drop* in surface temperature (Figure 2.6b). From these considerations, we argue that G1 to G2 is an atypical Sc to Cu transition.

2.4.6 The G3 climate

G3 is a hot, vapor-rich regime with a surface temperature of 360 K. In the annual mean, the G3 atmosphere has the characteristic structure of the moist greenhouse (P15, Wolf & Toon, 2015) with a humid inversion layer near the surface, a sub-saturated middle troposphere, and a cloudy upper troposphere (Figure 2.1). The G3 states hold approximately 5 m of precipitable water in the atmospheric column (not shown), or over 100 times more water than at $\xi = 1$. This magnitude of atmospheric moisture makes the G3 states the most Titan-like (Tokano et al., 2006). We will explore connections between G3 and Titan's climate in a companion paper.

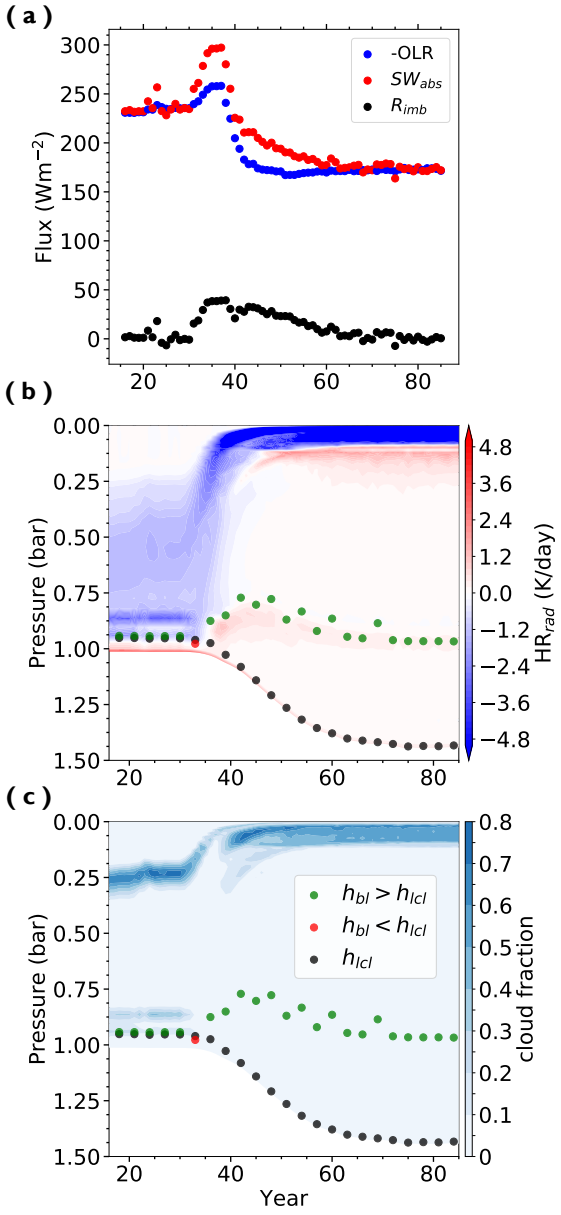

Figure 2.15: Visualization of the G2 to G3 transition for $\xi = 1.65$. (a) Outgoing longwave radiation (OLR), absorbed shortwave radiation (SW_{abs}), and radiative flux imbalance (R_{imb}) at the top of the atmosphere in Wm^{-2}. Hovmöller of the (b) radiative heating rate (HR_{rad}) in K/day and (c) fractional cloud cover with the height of the boundary layer (h_{bl}) and the lifting condensation level (h_{lcl}) overlain. The data are time averages over each year of the simulation. h_{bl} and h_{lcl} are given every third year in (c) to minimize overcrowding. The horizontal axis is the time in years since the start of the simulation. The vertical axis in (b) and (c) is total pressure and the legend is the same. Low clouds disappear in year 33 of the simulation when $h_{bl} < h_{lcl}$.

2.4.7 Evaluating Hypothesis 4: how a cloud instability causes low G2 clouds to break up

Our simulations confirm Hypothesis 4, that there exist vapor-rich states with elevated, single-layer clouds (Figure 2.1a,b). This result is consistent with many previous studies, which report the partial to total destruction of low clouds when the concentration of greenhouse gases in the atmosphere rises beyond a threshold value (Leconte et al., 2013; Popp et al., 2015; Wolf & Toon, 2015; Schneider et al., 2019; Seeley & Wordsworth, 2021). In the parameter space that we examine, low clouds disappear when $\xi \approx 1.65$. Low clouds are the largest source of planetary albedo in G2. Figure 2.15a,c shows that their disappearance produces an energy imbalance at the top of the atmosphere. This energy imbalance generates warming and an influx of water vapor into an expanding troposphere. Enhanced concentrations of water vapor then close the infrared windows to space, which causes radiation to converge in the lower troposphere (Figure 2.15b). It has been argued that an inability of the lower atmosphere to radiatively cool in vapor-rich atmospheres elevates the cloud profile (Leconte et al., 2013), and prevents low clouds from (re-)forming. We also adopt this perspective. High clouds thicken and brighten, bringing the column back into energy balance (Figure 2.15a,c).

Convergence of radiation into the lower troposphere likely explains the lack of low clouds in G3, but not why they disappear in the transition from G2. The solution is to examine another fundamental constraint on low cloud formation - one that has not been considered elsewhere. It is clear that moisture is resupplied to G2 low clouds by turbulent diffusion. The height reached by positively-buoyant eddies in the boundary layer is given by h_{cbl} (Equation (2.8)). The height to which a surface parcel must be lifted in order to saturate is h_{lcl} (Romps, 2017). Low clouds cannot form if the LCL comes to lie outside of the convective boundary layer, or in other words if boundary layer turbulence cannot lift moist parcels to the height where they condense. We quantify this effect with an instability parameter,

$$S_{23} = \frac{h_{lcl}}{h_{cbl}}. \tag{2.16}$$

If this parameter adequately describes when low clouds can form, then low clouds should break up when $S_{23} > 1$. We compute S_{23} using the values for h_{cbl} and h_{lcl} from Figure 2.9a. Figure 2.9b confirms that low clouds disappear when S_{23} approaches 1. What causes the non-monotonic trend in S_{23}? First, h_{lcl} drops as ξ increases, presumably due to an increase in near-surface RH (Figure 2.7) associated with the shallowing CBL (Rieck et al., 2012) and enhanced surface LHF (Figure 2.4b). However, h_{cbl} decreases more rapidly than h_{lcl} for increasing $\xi < 0.5$ and $\xi > 1$ and less rapidly in between, and this is sufficient to explain the non-monotonic behavior of S_{23} and thus the eventual destabilization of the low clouds.

Our simulations confirm that the breakup of low clouds triggers a climate transition into a state with elevated, single-layer clouds. We offer a constraint for low cloud formation, S_{23}, at the onset of this transition that combines only two basic ingredients, the depth of the CBL and the height of the LCL. We find that S_{23} is consistent with a low cloud breakup event at $\xi \approx 1.65$ where it crosses a critical value. Figure 2.15c confirms that low clouds disappear in the same year of our $\xi = 1.65$ simulation that the boundary layer drops below the LCL. This destabilizes the G2 low clouds by starving them of their supply of surface moisture.

2.5 Discussion

In our G2 simulations, the climate is insensitive to ξ over a wide range. A possible explanation for this is that ξ is varied by a single order of magnitude, whereas the SVP varies by many orders of magnitude over the depth of Earth's troposphere. The climate could be more sensitive to ξ as the change in temperature between the surface and the tropopause decreases (typical estimates for Earth and Titan differ by about a factor of 1/3). Titan's climate could also be less sensitive to ξ because the ratio L_v/R_v in the Clausius-Clapeyron relation for

water at 290 K is greater than methane at 90 K by a factor of 5 (here neglected). These thermodynamic differences are likely to be important in any modeling effort to bridge the space between Earth's and Titan's respective climates.

Our numerical experiment varying ξ showed that the vapor pressure path at the high cloud level in RCE states is close to its theoretically predicted value and therefore in support of the theory of JF20b that the spectral properties of water vapor control the decrease in longwave cooling at the top of the troposphere. Our result that high clouds rise and cool is broadly consistent with the physics behind the FAT hypothesis and a previous study that artificially increased the radiative effect of water vapor in the upper troposphere of a CRM (Harrop & Hartmann, 2012). By identifying a constant VPP across a broad range of ξ, our study provides strong support of the FAT hypothesis.

We tested fundamental concepts about cloud heights in atmospheres much different than our own by varying ξ. As demonstrated by JF20b, spectroscopic studies can offer deep insight into cloud formation. We raise the possibility that cloud heights in any atmosphere in RCE with a dominant condensing absorber might be inferred from the unique distribution of its absorption coefficient. Future modeling studies could consider a Titan-like atmosphere with methane as the dominant absorber and radiatively infer the cloud height. The radiative cloud height could then be readily compared to observations of cloud heights on Titan.

The response of the G2 low clouds to increasing ξ is consistent with prior work. In the tropics, the vertical potential temperature gradient is known to increase as the climate warms because the lapse rate is close to moist adiabatic, Γ_m (Wood & Bretherton, 2006). Bretherton et al. (2013) carried out two different sets of LES experiments of Sc- and Cu-topped boundary layers in which they increased the temperature of the free troposphere (FT) while keeping the surface temperature fixed (or warming it less than the FT). In both cases, they found a reduction in boundary layer entrainment and low cloud height. In our simulations, the CBL ultimately drops with increasing ξ because the FT warms faster than the boundary layer (because of invariant surface temperatures in G2 states) as Γ_m decreases (Figure 2.13b).

This is qualitatively similar to the outcome of "inversion strength" experiments detailed in Bretherton et al. (2013).

The CBL framework of N06 assumes that the cloud-top buoyancy fluxes that induce entrainment are proportional to the surface fluxes (see Equation 2.4), and therefore is of limited use outside Cu-like regimes where cloud-top radiative cooling is of greater importance. The inability to account for changes in cloud-top buoyancy fluxes associated with radiation is a limitation of the N06 framework (note that this framework is interpretative and is *not* part of ECHAM6). Figure 2.4a shows that longwave cooling at the top of the low clouds generally increases with increasing moisture, and this should promote boundary layer entrainment. The diagnosed decrease in CBL height suggests that radiative changes at the cloud-top are, at best, of secondary importance to stability changes in our simulations. The N06 estimate for CBL height is only diagnostic, and therefore it would be desirable to test this behavior in a CRM.

The simulations presented in this study could be interpreted as representing a range of cloud regimes over pole-to-equator conditions on Earth. For context, consider the change in surface temperature that represents the surface vapor pressure change over $0.01 \leq \xi \leq 1.85$. Adapting Equation 2.10 to the surface environment, one finds that this range of ξ corresponds to a 32 K change in temperature, from 273 K to 305 K. We extended an analogy in this study between G1 clouds and Sc as well as G2 low clouds and Cu. In nature, these cloud types are correlated with different SSTs (Cesana et al., 2019). Interestingly, the transition from G2 low clouds to G1 clouds occurs at low ξ, which may correspond to cooler and drier conditions on Earth.

Our simulations may be analogous to Earth's past, present, and future climates, of which we offer two examples. First, CRM simulations initiated at 305 K with a solar constant 10% higher than the modern day are climatologically unstable and slide into a hothouse climate in which water vapor radiatively heats the lower troposphere and low level clouds are far less common (Seeley & Wordsworth, 2021). Our G3 simulations share both of these

characteristics of the hothouse climate, which we intend to explore in future work. Second, Abbot (2014) used a CRM to study the behavior of clouds in a glaciated, "Snowball Earth" climate. Like previous studies (Abbot et al., 2012, 2013), Abbot (2014) found a troposphere-filling layer of surface-warming clouds peaking in the tropical mid-troposphere that they also likened to Sc under an inversion. In a GCM-intercomparison of Snowball Earth clouds, Abbot et al. (2012) found that the net CRF in the tropics of the summer hemisphere rose to 40 Wm^{-2}, which is close to the net CRF of our G1 states. G1 states are vapor-limited, and yet the G1 clouds possess similar, if not more, cloud condensate than the G2 states. Abbot et al. (2012, 2014) likewise found that cloud condensate densities in Snowball states (with tropical surface temperatures around 265 K) are comparable to reference simulations of modern-day low clouds. It is unclear why condensate densities are insensitive to large changes in ambient vapor pressure and temperature, and this should be further explored. The process that supplies moisture to the cloud in Abbot (2014) is dry convection and in our study is turbulent diffusion in a deep boundary layer. If our varying-ξ experiments were carried out with an eddy-resolving model, there would be no real distinction between the two. Given the similarities between the G1 clouds and these Snowball Earth clouds, we speculate that this type of single-layer cloud morphology is a moisture rather than a temperature effect, and thus a symptom of the atmospheric dryness.

Separate parameterizations for large-scale condensation, eddy diffusion, and convection are necessary to run a 1D climate model. When the atmosphere is simulated at a higher resolution in a CRM, the inconsistencies between their treatment is removed because these processes are more sensibly and directly coupled. The G1 to G2 transition coincides with a switch between diffusive and convective parameterizations and this fact is made very clear when convection is turned off. Is the G1 to G2 transition a real feature or is it an artifact of the parameterizations? Previous work lends credibility to there being G1- and G2-like states in CRMs (Abbot, 2014), but follow-up with a CRM is needed to know for sure.

The G2 and G3 states should be considered analogous to the climate states described

by P15. There are important differences between this study and P15 in the behavior of the clouds at the onset of the climate transition from a cool state with two-layer clouds to a hot state with elevated, single-layer clouds. P15 varied the solar constant in the 1D model used in this study and observed a 30% increase in column albedo and 300% increase in the column cloud water between the control state and the climate transition, leading them to conclude that low clouds delay the onset of the transition by reflecting more sunlight. In our experiments increasing SVP, we find that the net CRF becomes more negative in two-layer cloud states because high clouds warm less. The properties of the low clouds, which dominate the planetary albedo, are mostly unchanged. Thus, an increase in either forcing (insolation or ξ) reduces the net CRF, but for different reasons. The explanation given for the low cloud instability in this work also differs from that given by P15. They argue that low clouds disappear because of a transient increase in the vertical gradient of moist static energy. We frame the low cloud instability in our varying-ξ experiments in terms of a larger trend in which increasing moisture causes the CBL height to decrease faster than the LCL. Ultimately, the CBL dips under the LCL and low clouds become unstable, triggering a climate transition. It may be that the CBL-LCL constraint is only relevant within the ξ parameter space. If not, this need not imply a contradiction with P15. Our explanation of the low cloud instability stems from consideration of *equilibrium* climate states whereas P15's explanation is deduced from a non-equilibrium perspective of the climate transition, or in other words from analyzing the specific chain of events of a simulation undergoing the climate transition. Still, future studies may wish to consider whether some variation of the CBL-LCL instability underlies the moist greenhouse transition.

Finally, an unresolved question is why the CBL height matters at the G2 to G3 climate transition, where the depth of the simulated boundary layer is best approximated as the NBL (Figure 2.9a). A climate state where the NBL is deeper than the CBL is challenging to visualize, but timescales may be useful for intuition. The turnover timescale for the NBL ($\tau_{nbl} = \frac{h_{nbl}}{u^*}$) is a factor of 3 larger than that for the CBL ($\tau_{cbl} = \frac{h_{cbl}}{w^*}$) over the G2 states in

RCE (not shown). It may be that faster mixing in the CBL is important to the formation and maintenance of low clouds in high ξ states. This hypothesis should be tested in future work.

2.6 Conclusions

Our primary goal was to find climate "regime transitions" for hypothetical planets with vapor-rich and -poor atmospheres. We did this parametrically through a multiplicative constant, ξ, on the SVP of water at each temperature. Although motivated by "end-member" climate states on Earth and Titan, our focus necessarily involved extrapolation of the thermodynamics of the natural world through the alteration of the SVP of water. We also chose to restrict this study to a 1D climate model, which is well behind the state-of-the-art. This approach allows a broad study of ξ, providing testable hypotheses for future studies with a CRM. This abstraction, while clearly artificial, is nonetheless necessary to achieve our goal.

We put forward four hypotheses for the effects of changing the moisture content of an atmospheric column on clouds: 1) high clouds get higher as SVP increases; (2) low clouds get lower as SVP increases; 3) some vapor-poor states have a single cloud layer; and 4) some vapor-rich states have a single cloud layer. We tested the hypotheses with numerical experiments in which the SVP of water was artificially altered by a constant, ξ, in a single-column climate model. By altering the volatility of water vapor on an aquaplanet with Earth's background atmospheric composition, we isolated multiple effects of moisture on climate, clouds, and convection (CCC). These effects are illustrated in Figure 2.16. Below, we enumerate the main conclusions.

1. Three cloudy climate states are found by varying ξ. Earth-like, intermediate ξ states (G2) with 0.4-2 cm of precipitable water are in RCE, the surface temperature and column-integrated relative humidity are roughly constant, and clouds in the lower- and upper-troposphere with a net cooling effect are separated by a dry, cloud-free

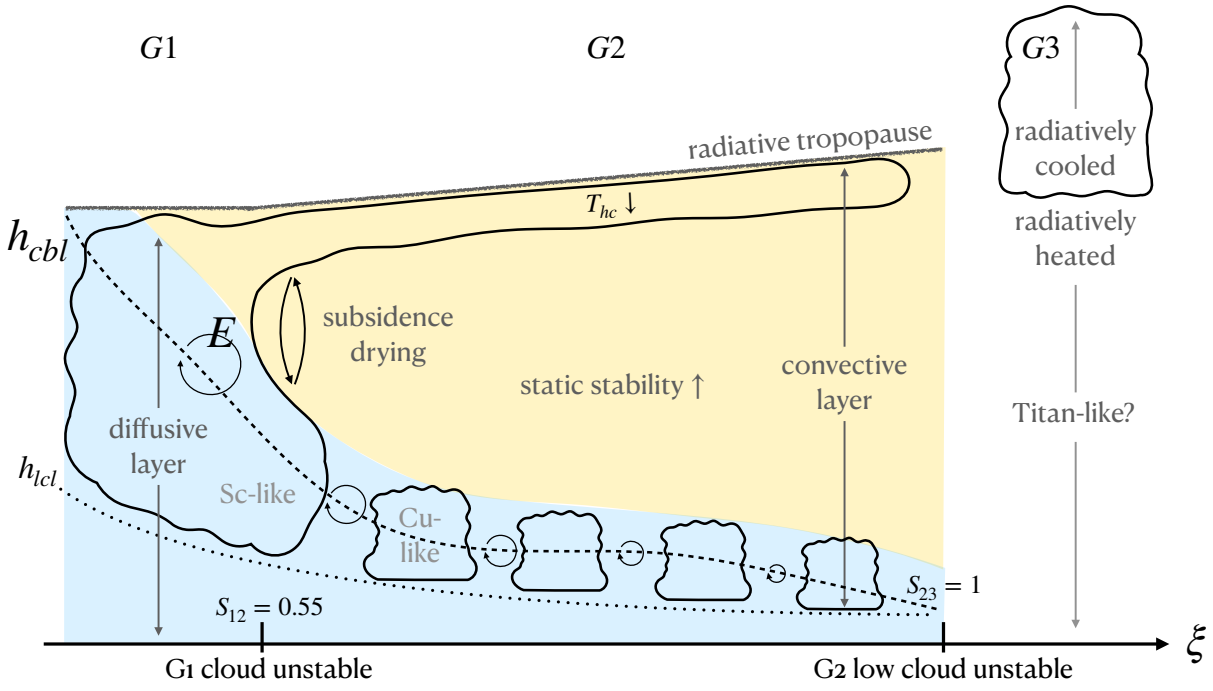

Figure 2.16: Illustration of the effect of varying ξ on climate, clouds, and convection. h_{cbl} is the height of the convective boundary layer and is traced as a dashed black line. h_{lcl} is the lifting condensation level and is traced as a dotted black line. Entrainment of free tropospheric air into the boundary layer (i.e., E) is depicted as a circular arrow. T_{hc} is the high cloud temperature. S_{12} and S_{23} are the cloud instability parameters referenced in the text that describe the G1→G2 and G2→G3 climate transitions, respectively. Clouds are sketched as thick, enclosed curves. Subsidence drying depicted as a pair of ascending and descending arrows. The diffusive and convective mixing layers are represented by blue and yellow shading, respectively. Shading preference is given to the former anywhere the two layers overlap.

layer. In low ξ states (G1) with 0.1-0.3 cm of precipitable water, a single cloud layer warms the surface by as much as 25 K relative to the reference state ($\xi = 1$). High ξ states (G3) have a surface temperature of 360 K, 5 m of precipitable water, and a radiatively-heated lower troposphere overlain by a radiatively-cooled upper troposphere with a single, net-cooling cloud.

2. High clouds get higher because they are bound by radiative constraints to occur at a lower temperature as ξ increases. For G2 states in RCE, the anvil cloud maximum and clear-sky longwave cooling decreases at a roughly constant vapor pressure path (VPP) predicted by an analytical theory of radiative transfer (Jeevanjee & Fueglistaler, 2020a). This result is perhaps the clearest demonstration of the FAT hypothesis to date.

3. Low clouds get lower because they are coupled to the convective boundary layer (CBL), which shallows with increasing ξ. The CBL shallows because of a partial cancellation between increased tropospheric stability and a reduced convective area fraction. The increase in tropospheric stability is due to a decrease in the lapse rate of the free troposphere, which causes the vertical gradient in potential temperature to increase. The convective area fraction change reflects that fewer positively-buoyant surface eddies reach the mean-state LCL as ξ increases.

4. Two-layer clouds first appear in vapor-poor states when a shallowing diffusively-mixed layer (with increasing ξ) separates from a convectively-mixed layer that tops out at the tropopause. Above the diffusive layer, moist convection maintains a thin high cloud (G2). Subsidence drying produces a relative humidity minimum at the separation level. The diffusively-mixed layer maintains the G2 low cloud. Clouds are well-separated in G2 because of the vertical offset of the diffusively-mixed layer and the level of deep convective detrainment.

5. G1 to G2 is an atypical Sc to Cu transition. At the transition, the G1 cloud meets the

minimum set of requirements for a Sc deck to decouple from the surface. Decoupling is primarily driven by a quasi-linear dependence of the surface latent heat flux on ξ. Across the transition, there is a 40% drop in peak cloud fraction and a 5 K drop in surface temperature.

6. Low clouds break up at the climate transition from G2 to G3 when the convective boundary layer falls below the lifting condensation level, cutting off the supply of moisture from the surface to the cloud. We combine the relevant physics into an instability parameter, S_{23}, that describes this constraint on low cloud formation and contextualizes the climate transition.

2.7 Appendix

2.7.1 Derivation of VPP invariance at cloud level to varying ξ

The spectrally-resolved optical depth with respect to total pressure is

$$\tau_{\tilde{\nu}}(p) = \int_0^p \kappa(\tilde{\nu}, p, T) q_v \, dp/g. \tag{2.17}$$

where $\tilde{\nu}$ is wavenumber, q_v is specific humidity, κ is the spectral absorption coefficient of water vapor (units of m^2/kg), and g is gravity.

$$\kappa(\tilde{\nu}, p, T) \approx \kappa(\tilde{\nu}, p) = \kappa_{ref}(\tilde{\nu}) \frac{p}{p_{ref}} D \tag{2.18}$$

For $\kappa(\tilde{\nu}, p)$, Jeevanjee & Fueglistaler (2020a, henceforth, JF20b) use a reference distribution, $\kappa_{ref}(\tilde{\nu})$, evaluated at $p_{ref} = 5 \times 10^4$ Pa and $T_{ref} = 260$ K with corrections for the two-stream approximation and changes in spectral absorption with pressure. The rough linear dependence of $\kappa(\tilde{\nu}, p)$ on pressure is given by the factor, $\frac{p}{p_{ref}}$. A value of 1.66 is used for the two-stream diffusivity factor, D. Note that in Equation (2.18) we neglect the weak

dependence of κ on temperature. An approximation for q_v at cloud level is

$$q_v \approx r_v = \varepsilon \frac{e}{p_d}, \tag{2.19}$$

where r_v is the water vapor mixing ratio, e is the partial pressure of water vapor, p_d is the partial pressure of dry air, and ε is the ratio of the specific gas constants of dry air and water vapor. As an aside, the maximum cooling occurs at $\tau_{\tilde{\nu}} = 1$ for each $\tau_{\tilde{\nu}}$. JF20b take advantage of the fact that a limited range of $\tilde{\nu}$ emit at similar $\kappa_{\tilde{\nu}}$ over the water vapor rotational band. In other words, the wavenumbers that cool to space at a given height are close together (Hartmann et al., 2022). Integrating over this limited range of $\tilde{\nu}$ gives the total cooling rate at each height. JF20b find that a coefficient of $k_{ref} = 40$ m^2/kg roughly corresponds to the location where cooling rates decrease with height. Setting $\tau_{\tilde{\nu}} = 1$ in Equation (2.17), substituting in Equations (2.18) and (2.19), and cancelling terms (assuming $p \approx p_d$), one obtains

$$\frac{D\varepsilon k_{ref}}{g p_{ref}} \text{VPP} = 1, \tag{2.20}$$

where VPP= $\int_0^p e \, dp$ is the vapor pressure path (Hartmann et al. 2022). In this study, $e = \xi \text{RH} e^*_{sat}$ where RH is relative humidity, e_{sat} is the saturation vapor pressure (SVP) of water, and ξ is the multiplicative factor used to artificially alter the SVP. Solving for VPP,

$$\text{VPP} = \frac{g \, p_{ref}}{D \, \varepsilon \, k_{ref}} \tag{2.21}$$

Note that Equation (2.21) depends only on fixed properties of water vapor. VPP specifically depends on the spectroscopic properties of water vapor (κ_{ref}) extrapolated from a reference height of p_{ref} and unperturbed thermodynamic properties of the absorber and the background gases ($\varepsilon = \frac{R_d}{R_v}$). g merely communicates the assumption of hydrostrophic balance, which sets the absorber concentration. Plugging some numbers in, $k_{ref} = 40$ m^2/kg, $p_{ref} = 5 \times 10^4$ Pa, g = 9.81 m/s^2, $\varepsilon = 0.622$, and D = 1.66, we predict cooling rates should decrease with height at VPP $\approx 1.2 \times 10^4$ Pa^2.

CHAPTER 3

Clear-sky convergence and the origin of tropical congestus clouds

Congestus clouds, characterized by their towering vertical structure, are widespread in tropical regions and play a pivotal role in Earth's climate system by their contribution to cloud radiative forcing, atmospheric humidification, and surface rainfall. However, their spatial abundance is inaccurately captured by state-of-the-art climate models, revealing that many fundamental questions regarding their formation, dynamics, and implications for regional climate variability remain unanswered. Here, we demonstrate how congestus cloud tops form by detraining preferentially at altitudes between 5-6 km and why they are more prevalent in dry mid-tropospheric conditions. Convective detrainment maximizes at a height of 5-6 km due to a swift decline in the water vapor cooling rate in clear-sky regions. This decline is, in turn, a consequence of the spectral density of strong absorption lines in the water vapor rotation band. The increased prevalence of congestus clouds in drier mid-tropospheric conditions is due to stronger vertical gradients in the clear-sky cooling rate, which drives stronger outflow at 5-6 km. Our finding of a clear-sky radiative mechanism for congestus cloud top formation could be used to refine models of mid-level cloud fraction in general circulation models, which systematically under-estimate this major cloud population.

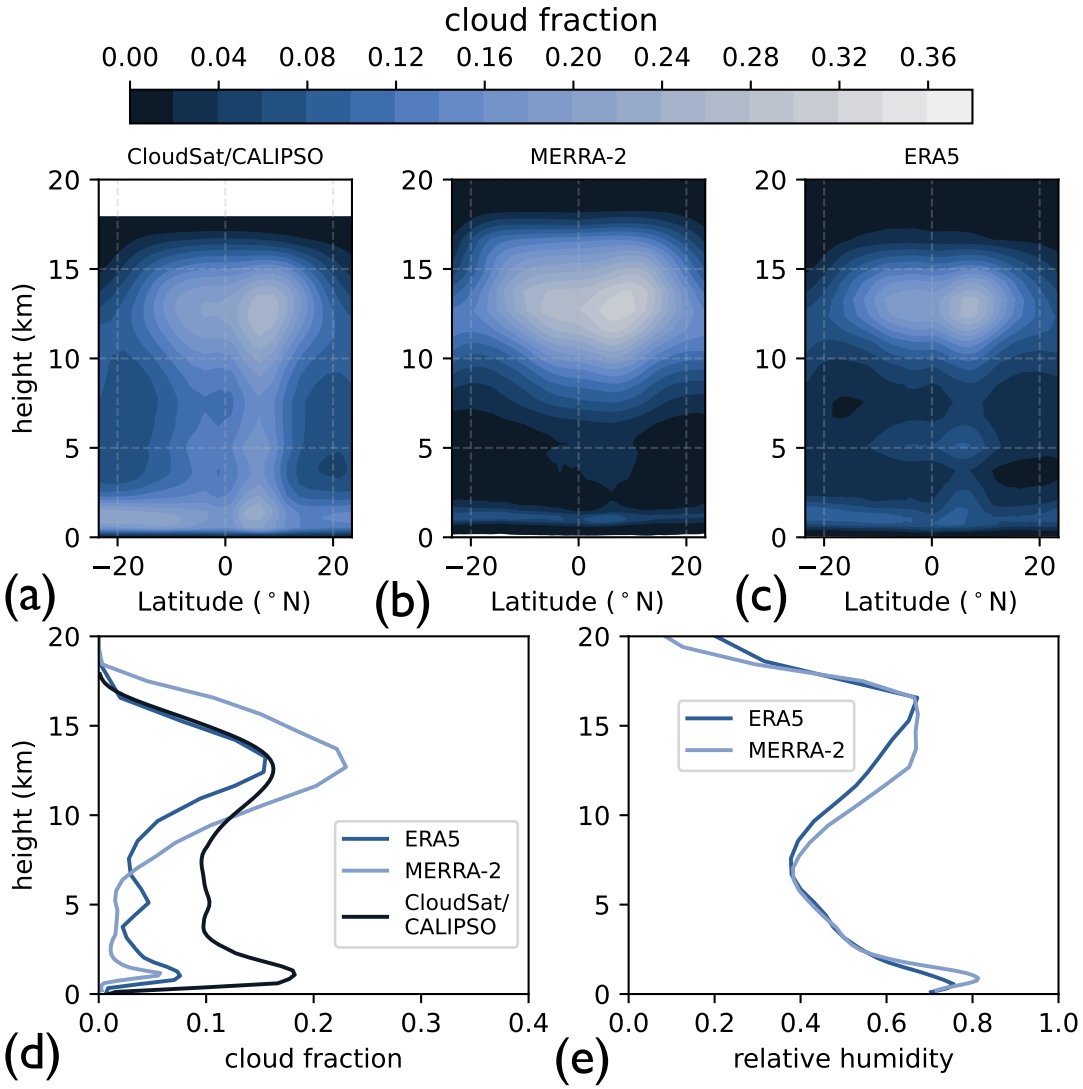

Figure 3.1: In the first row, zonal-mean average of cloud fraction in the tropics over 2006-2019 from (a) combined CloudSat/CALIPSO observations (Bertrand et al., 2023), (b) the MERRA-2 re-analysis, and (c) the ERA5 reanalysis. In the second row, (d) tropical-mean cloud fraction from observations and reanalyses and (e) tropical-mean relative humidity from reanalyses.

3.1 Introduction

Tropical clouds, i.e. those found within approximately 23.5 degrees of the equator, appear in three distinct cloud populations or "modes": shallow cumulus, mid-level congestus and deep cumulonimbus (Johnson et al., 1999). A simple way to demonstrate the existence of the three modes is by inspection of the tropical-mean cloud fraction from CloudSat/CALIPSO observations (Figure 3.1a; Bertrand et al., 2023), which reveal three peaks in the vertical distribution of cloudiness. Shallow cumulus, also known as fair-weather clouds, form at the top of the boundary layer and cool the climate by reflecting sunlight (Cesana et al., 2019; Albrecht et al., 2019). Precipitating cumulonimbus rise out of the boundary layer and detrain near the tropopause, forming anvils as the cloudy air spreads out laterally (Hartmann et al., 2018; Romps, 2014). The detraining anvils are also associated with the production of thin, high cirrus, which have a greenhouse warming effect on the climate (Sassen et al., 2009). Congestus clouds extend well above shallow cumulus but are less vertically developed than deep cumulonimbus, terminating in the mid-troposphere (Wall et al., 2013; Mechem & Oberthaler, 2013). Unlike the other modes, congestus cloud tops form where the relative humidity (RH) tends to be low (Figure 3.1e). Thin, mid-level clouds with a cooling effect are ubiquitous in the tropics and are associated with convective detraiment at congestus peaks (Bourgeois et al., 2016). The focus of this paper is on the origin of the middle, congestus peak.

Tropical congestus clouds reach their peak altitude at 5-6 km, with the spread indicative of the typical values over ocean and land areas (Wall et al., 2013). Two theories based on buoyancy arguments have been proposed to explain the height of the congestus peak: the weak stability theory and the dry air entrainment theory. The shared premise of these theories is that some buoyancy-reduction mechanism decelerates cloudy air as it ascends, causing it to accumulate and spread out preferentially at this level (Redelsperger et al., 2002; Jensen & Genio, 2006). The weak stability theory posits that semi-permanent and/or transient ar-

eas of weak stability in the mid-troposphere act as barriers to convective cloud development. Various mechanisms that generate weak stability have been proposed, including melting of stratiform cloud ice across the 0°C freezing level at 4-5 km in typical tropical conditions (Johnson et al., 1996), re-evaporation of detrained cloud condensate (Nuijens & Emanuel, 2018), and sublimation cooling as a result of dry air intrusions (Zuidema et al., 2006). The freezing level explanation is compelling because it is based on simple moist thermodynamics and, for this reason, the freezing level is commonly referenced in studies of tropical congestus (Johnson et al., 1999; Jensen & Genio, 2006; Mechem & Oberthaler, 2013). The dry air entrainment theory asserts that congestus clouds peak in the mid-troposphere where the RH is lowest due to a loss of buoyancy from mixing between the cloud and its dry environment (Brown & Zhang, 1997). A strong consensus as to which mechanism is most important to congestus clouds seems to be lacking, with some studies arguing in favor of weak stability (Zuidema, 1998) or dry air entrainment (Brown & Zhang, 1997; Takemi et al., 2004; Jensen & Genio, 2006; Kumar et al., 2014) or both (Johnson et al., 1999; Redelsperger et al., 2002). There is, on the other hand, concordance between observations and model simulations that congestus clouds are more prevalent where the mid-level RH is low (Brown & Zhang, 1997; Redelsperger et al., 2002; Takemi et al., 2004; Jensen & Genio, 2006; Kumar et al., 2014; Sokol & Hartmann, 2022). These studies also find that areas with low mid-level RH have fewer deep convective clouds (cumulonimbus).

Therefore, a well-rounded theory of congestus cloud top formation should be able to explain (1) the 5-6 km peak in cloud fraction *and* (2) the enhancement of congestus by low mid-tropospheric RH. While weak stability at the freezing level of water may indicate why congestus clouds terminate near 5 km, it does not explain the invigoration of congestus clouds by low mid-tropospheric RH. Similarly, the dry air entrainment theory implies that congestus/cumulonimbus clouds should be more/less prevalent when the mid-level RH is low, but it does not tell us why congestus clouds peak at 5-6 km, which is well below the tropospheric minimum in RH at 7.5 km (Figure 3.2e). Of course, there may be a coordination

between both buoyancy-reduction mechanisms that reproduce the observations, but this is far from obvious given the evidence. A goal of this study, therefore, is to derive a theory of cloud formation that explains both observations of congestus clouds.

Around two decades ago, Hartmann & Larson (2002) hypothesized a connection between the height of anvil clouds and the emissivity of water vapor. Notably, a reduction in emissivity around the 200 hPa level produces a swift decline in radiative cooling. This phenomenon is realized in cloud-resolving model simulations (Zelinka & Hartmann, 2010), wherein the strongest convective outflow occurs precisely where radiative cooling declines at the fastest rate with increasing height. Given that the concentration of water vapor in the upper troposphere is primarily governed by temperature, it was hypothesized that these anvil clouds should consistently form at a specific temperature. The so-called "fixed anvil temperature" (FAT) hypothesis is generally backed by the results of observation and modeling (Kuang & Hartmann, 2007; Zelinka & Hartmann, 2010; Li et al., 2012). The robustness of the fixed cloud-top temperature, in the strictest sense, is debated (Seeley et al., 2019a; Seidel & Yang, 2022). Recently, the underlying cause of the decline in emissivity at the upper tropospheric boundary was clarified by Jeevanjee & Fueglistaler (2020b) (henceforth JF20a). Employing a line-by-line radiative transfer model, they revealed that the diminishing upper-tropospheric emissivity partly stems from a decrease in the abundance of strongly-absorbing wavenumbers within the rotational band of water vapor above the 200 hPa level. Their result motivates the question: can the congestus peak be similarly understood through clear-sky radiative transfer? On large spatio-temporal scales, the tropics are in a state of energy balance between radiative cooling and latent heating known as radiative-convective equilibrium (RCE; Jakob et al., 2019; Miyawaki et al., 2022). It is reasonable to assume that most of this latent heating occurs in cloudy regions. Since clouds are effective at limiting the outgoing longwave radiation to space, it is also reasonable to assume that most of the radiative cooling occurs in the clear-sky regions. Since cloudy regions and clear-sky regions are energetically connected, the physics that governs one may also influence the other. From this simple con-

ceptual picture, a *clear-sky* theory of cloud formation emerges in which cloudy air converging into clear-sky regions is connected to vertical decreases in the clear-sky cooling rate. The "clear-sky convergence" (CSC) hypothesis is at the heart of the FAT hypothesis, and its applications could be broader than previously recognized. A goal of this study is to extend the CSC theory to congestus clouds.

The structure of this paper is as follows. In Section 3.2, we derive the CSC theory of cloud formation. In Section 3.3, we describe our method of evaluating the CSC theory with a state-of-the-art radiative transfer model. In Section 3.4, we show that water vapor absorption is associated with a rapid decrease in the clear-sky cooling rate near the congestus level. In Section 3.5, we use our theory to show that crucial information about congestus cloud height is encoded in the hidden "spectral dimension" of an atmosphere in RCE. In Section 3.6, we use the CSC theory to explain congestus invigoration when the mid-level RH is low. In Section 3.7, we discuss the implications of our findings for the representation of mid-level cloudiness in global climate models. Finally, in Section 4.5, we summarize our results and compare them against previous theories of congestus formation.

3.2 A clear-sky theory of cloud formation in radiative-convective equilibrium

We now develop a predictive model of cloud-top formation based on the CSC hypothesis. Consider an idealized tropical environment in which there is widespread subsidence in clear-sky regions and narrow ascent in cloudy regions (Figure 3.2a), which are linked by mass balance (Hartmann & Larson, 2002; Seeley et al., 2019a). We assume that cloud generation over large horizontal areas is linked to the convergence of cloud water into clear-sky regions, an assumption that is supported by cloud-resolving model simulations (Zelinka & Hartmann, 2010; Beydoun et al., 2021; Jeevanjee & Zhou, 2022). Conservation of energy in clear-sky

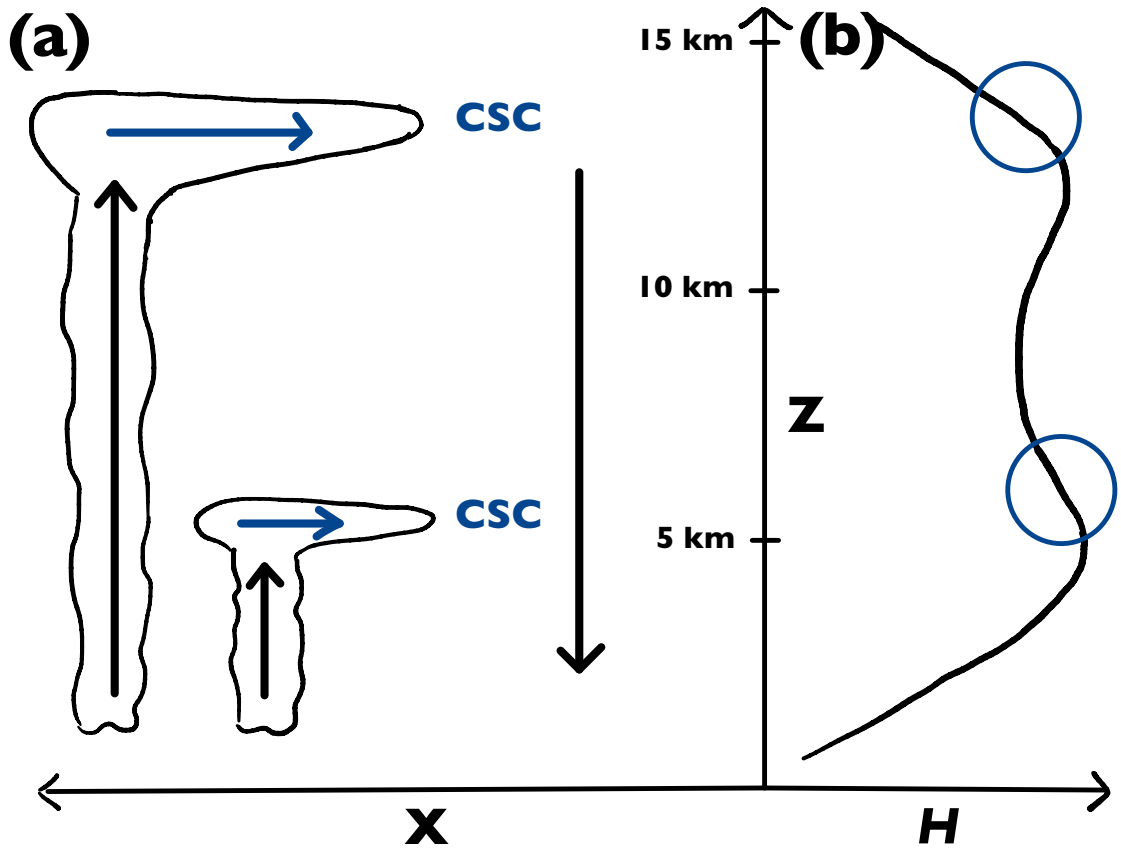

Figure 3.2: The radiative-convective perspective of cloud formation links the decline in clear-sky radiative cooling with height to transport of cloudy air into clear-sky regions. In (b), there are two regions where this hypothetical clear-sky infrared cooling rate $\mathcal{H}$ decreases with height, which are associated with hypothetical middle and high peaks in cloud fraction in (a). Our study focuses on the middle "congestus" peak.

regions can be expressed as

$$\begin{array}{rcl} \rho c_p \dfrac{\partial T}{\partial t} & = & \dfrac{\partial p}{\partial t} - H, \\ (i) & & (ii) \;\; (iii) \end{array} \tag{3.1}$$

where ρ is density, c_p is the specific heat of environmental air at constant pressure, p is pressure, T is temperature, and H is diabatic heating, each having their usual units. Conservation requires the change in energy density of the air (i) balance subsidence warming (ii) and diabatic cooling (iii), the latter including both radiative and latent heating. If the diabatic cooling in clear-sky regions is primarily radiative and shortwave absorption is small, then H can be approximated by the infrared cooling rate $\mathcal{H}$ (by convention, positive values for cooling). Note that re-evaporation of cloud condensate in clear-sky regions is another potentially important source of local cooling that can increase the clear-sky convergence (Jeevanjee & Zhou, 2022), which we neglect. With these assumptions, the clear-sky mass flux (positive downward),

$$M_{clr} = \frac{\partial_t p}{g} = \frac{\mathcal{H}}{c_p \sigma}, \tag{3.2}$$

where $\sigma = \Gamma_d - \Gamma$ is the static stability (positive values are stable to dry convection). By mass continuity, (vertical) divergence in M_{clr} must be balanced by clear-sky (horizontal) convergence:

$$\begin{array}{rcl} \text{CSC } (\text{s}^{-1}) & = & \dfrac{-\partial_z M_{clr}}{\rho} \\ & = & \dfrac{-1}{c_p \rho \sigma} \partial_z \mathcal{H} + \dfrac{\mathcal{H}}{c_p \rho \sigma^2} \partial_z \sigma. \end{array} \tag{3.3}$$

Positive values of CSC support a net transport of air from the cloud into clear-sky regions – i.e. detrainment – and following Seeley et al. (2019b) is specified with the units of an inverse timescale. Equation 3.3 identifies two environmental factors that support CSC. First, CSC may occur when there is a decrease in radiative cooling with increasing height, $\partial_z \mathcal{H} > 0$. Second, CSC may occur where the static stability increases with height, $\partial_z \sigma > 0$. In regions where the first term is positive, however, the stability term is typically negative and thus

reduces the net positive CSC, as pointed out by Seeley et al. (2019a). If we assume that the mid-tropospheric clear-sky lapse rate is constant, the CSC at the congestus level would be dominated by vertical changes in the clear-sky cooling rate.

$$\text{CSC} \approx \frac{-1}{c_p \rho \sigma} \partial_z \mathcal{H}. \tag{3.4}$$

Equation 3.4 is an expression of the CSC hypothesis, and will be assumed throughout the remainder of this work. Figure 3.2 demonstrates the significance of this simple picture of cloud formation. In Figure 3.2b, a hypothetical clear-sky cooling rate is given, in which there are two locations where $\mathcal{H}$ decreases with height. Convective detrainment should be preferred at these heights, and therefore contribute to the areal cloud fraction as depicted schematically in Figure 3.2a. To relate this simple picture to the congestus mode, we hypothesize that a decrease in clear-sky cooling must preferentially occur between 5-6 km, and that it must be associated with one or more of Earth's greenhouse gases. In Section 3.3, we describe our method of computing $\mathcal{H}$ with a line-by-line radiative transfer model for several greenhouse gases.

3.3 Methods

We employ the Reference Forward Model (RFM; Dudhia, 2017) for line-by-line radiative transfer calculations at high resolution over a clear column of atmosphere. We use a vertical resolution of 100 m between the surface and the top of atmosphere at 30 km and a spectral resolution of 0.1 cm^{-1} between 10-1500 cm^{-1}. This spectral range was chosen because it includes the majority of blackbody emission at typical tropical conditions. Specifically, it includes 93% of the spectrally-integrated emission from a 300 K blackbody and 99% of the spectrally-integrated emission from a 200 K blackbody. In our RFM calculations, we use the most recent line absorption data from the 2020 High-Resolution Transmission (HITRAN; Gordon et al., 2022) release. Continuum absorption by water vapor and carbon dioxide are included in our calculations, which are represented in RFM according to Mlawer et al. (2012)

and Edwards (1992). Since oxygen and nitrogen are transparent to infrared radiation, we do not include them in our line-by-line calculations. As model inputs, we provide vertically-resolved profiles of temperature, pressure, and absorber mixing ratio that are representative of the tropical atmosphere. These inputs include a surface pressure and temperature of 1 bar and 300 K, a uniform lapse rate of 7 Kkm^{-1}, and an isothermal stratosphere of 200 K. From these inputs, RFM computes the clear-sky infrared cooling rate, optical depth, transmissivity, and molecular absorption coefficients as a function of height, temperature, absorber concentration, and wavenumber. The line-by-line cooling rates from RFM are used to calculate the clear-sky convergence (Equation 3.4)

We construct four scenarios for radiative transfer calculations with RFM: (1) h2o, (2) h2o-co2, (3) co2, and (4) h2o-C. The absorbing species in scenarios (1) and (4) is water vapor and in scenario (3) is carbon dioxide; scenario (2) includes both water vapor and carbon dioxide. In scenarios (1) and (2), the troposphere has a uniform RH of 75% and the stratospheric water mixing ratio is pegged to the tropopause value and is constant with height. In scenarios (2) and (3), the molar mixing ratio of carbon dioxide is constant with height at 350 ppmv. Scenario (4) differs from scenario (1) only in that we allow RH to vary with height in a "C"-shape between the surface at 75% RH, the tropopause at 75% RH, and a mid-tropospheric RH minimum (RHmin) at 7.5 km. To construct a smooth C-shape from these three points, we perform a least-squares polynomial fit on the intersecting lines.

3.4 The spectral origin of the congestus mode

The CSC theory states that cloud formation is linked to decreases in $\mathcal{H}$ with height. In the h2o, h2o-co2, and co2 scenarios, we evaluate $\mathcal{H}$ with RFM and solve for the CSC using Equation 3.4. These scenarios differ only the number of greenhouse gases included in the RFM calculation (see Methods). The result is given in Figure 3.3a. Below the tropopause, $\mathcal{H}$ monotonically decreases with height in all scenarios. Figure 3.3a reproduces the well-known

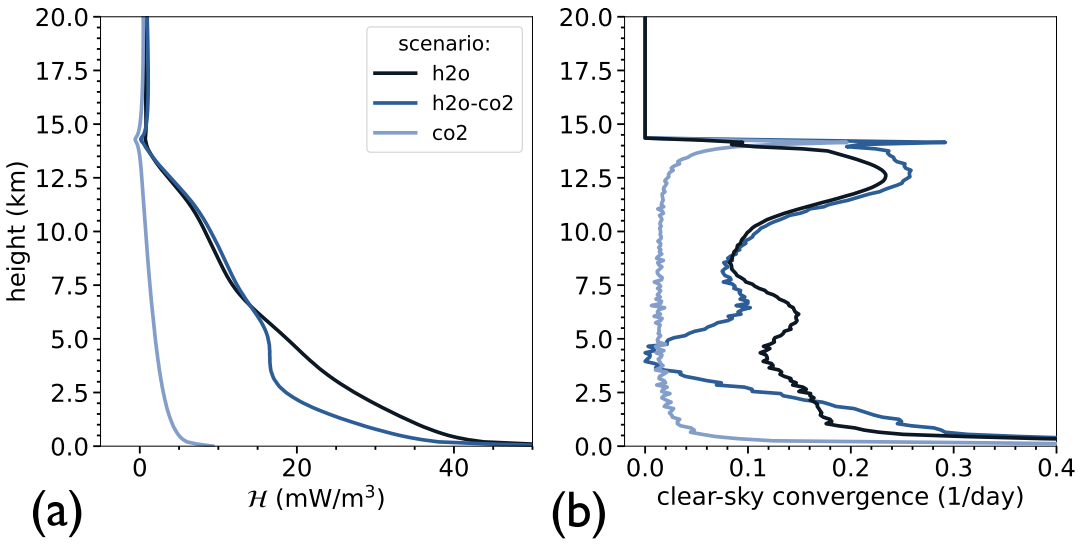

Figure 3.3: (a) RFM cooling rate $\mathcal{H}$ (Equation 3.5) and (b) clear-sky convergence (Equation 3.4) in 3 different absorbing scenarios.

fact that water vapor accounts for the overwhelming majority of tropospheric cooling (Held & Soden, 2000). Figure 3.3b demonstrates that regions where $\mathcal{H}$ falls off fastest with height give rise to the peaks in CSC, in accordance with Equation 3.4. The cooling rate associated with the h2o scenario has a strong local decrease in the mid-troposphere that produces a peak in CSC at 6 km. Therefore, we propose that the congestus peak in Figure 3.1d is related to the radiative properties of water vapor.

To better understand the role of water vapor in driving CSC at 6 km, we resolve the spectral dimension of $\mathcal{H}$. The cooling rate ($\mathcal{H}$; Wm^{-3}) is, in fact, an integral over the spectrally-resolved cooling rate ($\tilde{\mathcal{H}}$; Wm^{-3}cm) in wavenumber space:

$$\mathcal{H}(z) = \int \tilde{\mathcal{H}}(\nu, z) d\nu \tag{3.5}$$

where ν is wavenumber (cm^{-1}) and z is height. For now, we leave Equation 3.5 as an indefinite integral, and comment on the boundaries later. Tildes are used to identify any variable that is spectrally-resolved: i.e., a function of wavenumber. When we say that an atmospheric layer is radiatively cooling, what we mean is that more radiation is going out

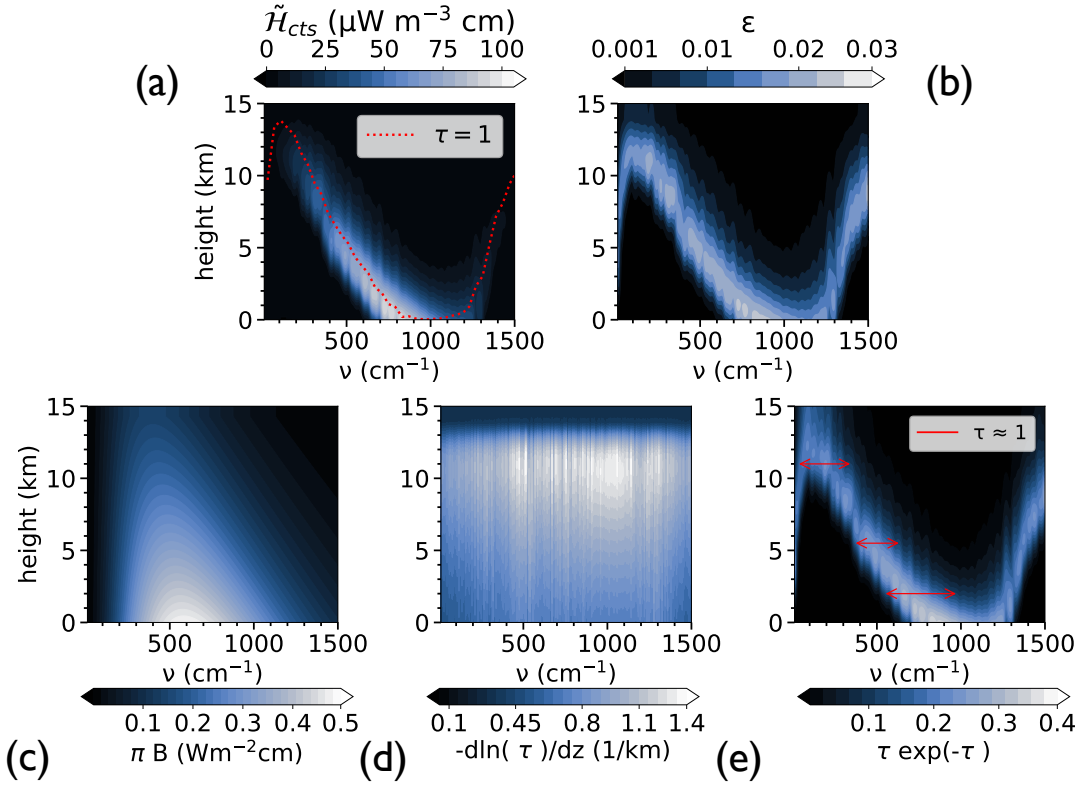

Figure 3.4: In the first row, (a) the cooling-to-space cooling rate $\tilde{\mathcal{H}}_{cts}$ (Equation 3.6) and (b) the spectrally-resolved emissivity $\tilde{\epsilon} = \Delta z \times -\partial_z \ln(\tilde{\tau}) \times \tilde{\tau} \exp(\tilde{\tau})$ using layer thicknesses of $\Delta z = 100$ m. In (a), $\tilde{\tau} = 1$ surfaces as linear averages over coarse 40 cm^{-1} bins. In the second row, we show the key terms of $\tilde{\mathcal{H}}_{cts}$: (c) $\pi \tilde{B}$, (d) $-\partial_z \ln \tilde{\tau}$, and (e) $\tilde{\tau} \exp(-\tilde{\tau})$. In (e), the emitting width of water vapor (i.e., the spectral region where $\tilde{\tau} \approx 1$) at 3 heights is estimated with a red line, and this shows a narrowing in the mid-troposphere. All data are from the h2o scenario.

than coming in. In the case of a molecule like water vapor in Earth's tropics, it is reasonable to make the cooling-to-space (CTS) approximation (Jeevanjee & Fueglistaler, 2020a). In the CTS approximation, we assume that the non-local upwelling and downwelling fluxes cancel out, and so the net upward flux at any given height is equal to the fraction of the local Planck emission that escapes to space (Jeevanjee & Fueglistaler, 2020b).[1] This approximation isn't necessary for our arguments, but it brings to the fore the underlying mechanism for CSC in Earth's middle troposphere. The cooling rate in the CTS approximation may be expressed as a spectral integral over the product of three terms

$$\mathcal{H}_{cts}(z) = \int \underset{(i)}{\pi \tilde{B}} \times \underbrace{\frac{-\partial \ln \tilde{\tau}}{\partial z}}_{(ii)} \times \underbrace{\tilde{\tau} \exp(-\tilde{\tau})}_{(iii)} \, d\nu \tag{3.6}$$

where

$$\tilde{\tau} = \int_0^p \tilde{\kappa}(\nu, p, T) \, q \, dp/g \tag{3.7}$$

is the spectrally-resolved optical depth that is by convention zero at the top of the atmosphere and increases monotonically towards the surface (Jeevanjee & Fueglistaler, 2020a). $\tilde{\kappa}$ is the specific absorption cross section, p is the pressure and g the surface gravity. The terms in Equation 3.6 can be understood as follows: (i) $\pi \tilde{B}(\nu, T)$ is the Planck emission at the local temperature T in $\mathrm{Wm}^{-2}\mathrm{cm}.^2$; (ii) $\partial_z \ln \tilde{\tau}$ is the inverse scale height of optical depth in m^{-1}, a measure of how rapidly the emissivity declines with height; and (iii) $\tilde{\tau} \exp(-\tilde{\tau})$, which has a maximum at $\tilde{\tau} = 1$, is the "$\tau = 1$" law of radiative transfer that states $\tilde{\mathcal{H}}$ at a particular wavenumber is strongest where $\tilde{\tau} = 1$.

The fact that the absorption cross section of a molecule like water vapor depends on the wavenumber of light (as well as the ambient temperature and pressure) is central to our estimate of the congestus height in Section 3.5. Figure 3.5b shows $\tilde{\kappa}_{ref}(\nu)$, which is

[1] In the SI, we verify that the CTS approximation agrees to within ∼10% with $\mathcal{H}$ for water vapor and, more importantly, $\mathcal{H}_{cts}$ decreases rapidly with increasing height between 5-6 km.

[2] The pre-factor of π comes from an integral of the spectral intensity over all upper-hemispheric solid angles (e.g., see Rybicki & Lightman, 1985)

the specific absorption cross section at a reference temperature and pressure of 260 K and 500 hPa; absorption per unit mass is larger in the peaks than in the valleys. The peak at 150 cm^{-1} is the center of the water vapor rotation band and the peak to the right of 1500 cm^{-1} (just beyond the upper limit of the axis) is the center of the water vapor vibration-rotation band. We demarcate the rotation band as the spectral region to the left of 1000 cm^{-1} and vibration-rotation band as the spectral region to the right of 1000 cm^{-1}. With this definition, we turn to Figure 3.4a, which shows $\mathcal{H}_{cts}$ in the h2o scenario. It is clear in Figure 3.4a that most of the cooling originates from the water vapor rotation band. It is easy to understand why this must be the case from Figure 3.4c. The temperature range of Earth's troposphere places the peak in blackbody emission roughly between 400-600 cm^{-1}, with the maximum values of $\pi\tilde{B}$ (those greater than 0.3 $Wm^{-2}cm$) falling squarely within the water vapor rotation band. This implies that the rapid decrease in $\mathcal{H}$ and the associated peak in CSC at 6 km originates in the water vapor rotation band.

In Equation 3.6, we investigate which of the three terms can be eliminated as the cause for the swift decline in $\mathcal{H}$ at 6 km. First, we consider $\pi\tilde{B}$. In Figure 3.4c, it's evident that $\pi\tilde{B}$ monotonically decreases with height for every wavenumber. This behavior is expected because blackbody emission increases monotonically with temperature. However, the lapse rate in the troposphere is, by construction, a constant. Planck's law does not predict an unusually rapid decrease in $\pi\tilde{B}$ over the temperature drop of 265 K to 251 K between 5-7 km. Consequently, we can rule out $\pi\tilde{B}$. Next, we turn our attention to $-\partial_z \ln\tilde{\tau}$, shown in Figure 3.4d. We see that $-\partial_z \ln\tilde{\tau}$ steadily increases from the surface to 11 km, indicating that the scale height of optical depth decreases. Between 11 km and the tropopause, the emissivity of water vapor and the optical depth swiftly decline (Figure 3.4b, Jeevanjee & Fueglistaler, 2020b; Hartmann & Larson, 2002), producing an upper-tropospheric decrease in $-\partial_z \ln\tilde{\tau}$. In the stratosphere, $-\partial_z \ln\tilde{\tau}$ is uniform with height because q is, by construction, fixed to its value at the tropopause. Thus, we can also rule out $-\partial_z \ln\tilde{\tau}$.

Through process of elimination, only $\tilde{\tau}\exp(-\tilde{\tau})$ in Figure 3.4e can explain the mid-

tropospheric decline in $\mathcal{H}$. A general property of the special mathematical function $\tilde{\tau}\exp(-\tilde{\tau})$ is that only wavenumbers where $\tilde{\tau} \approx 1$ significantly contribute to the spectral integral in Equation 3.6. This consequence of the $\tau = 1$ law is visually apparent when comparing the height of $\tilde{\tau} = 1$ surfaces in Figure 3.4a to where most of the spectrally-resolved cooling emanates. Indeed, $\tilde{\mathcal{H}}_{cts}$ is strongest near $\tilde{\tau} = 1$ surfaces. Thus, we may interpret $\tilde{\tau}\exp(-\tilde{\tau})$ as an effective emitting width - that is to say, the wavenumber interval $\Delta\nu$ that meaningfully contributes to $\mathcal{H}$ (see also Jeevanjee & Fueglistaler, 2020b). In Figure 3.4e, we provide a visual approximation for the magnitude of $\Delta\nu$ with horizontal lines spanning the region where $\tilde{\tau}\exp(-\tilde{\tau}) \geq 0.15$. What Figure 3.4e tells us, therefore, is that a narrowing of the effective emitting width of water vapor occurs at a height of 6 km. As fewer wavenumbers in the water vapor rotational band contribute to the cooling rate at 6 km, $\mathcal{H}$ more swiftly declines, and CSC reaches a local maximum by Equation 3.4.

3.5 Line-by-line estimate of the congestus peak

In the previous section, we learned that $\mathcal{H}$ rapidly declines at 6 km due to a narrowing of the spectral emitting width in the water vapor rotation band, $\Delta\nu(\tilde{\tau} \approx 1)$. This information can be exploited to estimate the congestus height. The emitting width is only a function of $\tilde{\tau}$, which, in turn, depends only on pressure p, gravity g, specific humidity q, and the spectral absorption coefficient $\tilde{\kappa}$. Equation 3.7 reveals that $\tilde{\kappa}$ is the only spectrally-resolved dependency of $\tilde{\tau}$. Thus, any narrowing of $\Delta\nu$ must stem from $\tilde{\kappa}$. $\tilde{\kappa}$ is a fixed spectroscopic property of water vapor, and its value is uniquely determined as a function of wavenumber, pressure, and temperature. Note that, for analytic tractability, we neglect the minor dependence of $\tilde{\kappa}$ on temperature.

$$\tilde{\kappa}(\nu, p, T) \approx \tilde{\kappa}(\nu, p) = \tilde{\kappa}_{ref}(\nu, 500\text{hPa}, 260\text{K})\frac{p}{p_{ref}}D. \tag{3.8}$$

$\tilde{\kappa}_{ref}$ is the absorption coefficient distribution at a reference temperature (T_{ref}) and pressure (p_{ref}) of 260 K and 500 hPa. The roughly linear dependence of $\tilde{\kappa}$ on pressure is given by

the factor p/p_{ref}, and results from pressure broadening of absorption lines. We use the default RFM value for the two-stream diffisivity factor $D = 1.5$. Figure 3.5b spectrally-resolves the peaks and valleys of $\tilde{\kappa}_{ref}$. To bring out the features of interest, we also show $\tilde{\kappa}_{ref}$ log-averaged over 10 cm^{-1} bins, which gives a smooth fit to the absorption lines. In Figure 3.4a, we see that $\tilde{\tau} = 1$ surfaces mirror the shape of $\tilde{\kappa}_{ref}$. Referring back to Equation 3.7, this comes about because wavenumbers where $\tilde{\kappa}_{ref}$ is large have $\tilde{\tau} = 1$ surfaces near the top of the atmosphere, and vice versa. Since $\Delta\nu$ measures the width of the spectral region that significantly contributes to the total emission, a narrowing of $\Delta\nu$ implies that it is associated with a region of $\tilde{\kappa}_{ref}$ with a lower density of absorption lines. To prove this, we perform a two-dimensional (2D) binning procedure of $\log_{10}(\tilde{\kappa}_{ref})$ values with bin widths of 100 cm^{-1} between 150-1000 cm^{-1} and bin heights of uniform logarithmic increments of 0.2.[3] The results of this procedure given as a 2D histogram in Figure 3.5a. There appears to be a drop in line density around $\log_{10}(\tilde{\kappa}_{ref}) = 0.5$. To confirm this, we perform a 1D binning procedure of $\log_{10}(\tilde{\kappa}_{ref})$ over a single spectral bin between 150-1000 cm^{-1} with the same bin heights as before. There are, at least, two regions in Figure 3.5a where there is a significant drop in the line density of $\tilde{\kappa}_{ref}$. The first region is near 40 m^2/kg (Jeevanjee & Fueglistaler, 2020b), and is central to the reason why cooling rates decline rapidly with height in the upper troposphere. The second region is between 0.3-1.1 m^2/kg, which we will show causes the mid-tropospheric decline in $\mathcal{H}$.[4]

To retrieve the congestus peak, we simply solve for the height where $\tilde{\tau} = 1$ and $\tilde{\kappa}_{ref} =$ 0.3-1.1 m^2/kg. Using an approximation for the specific humidity,

$$q \approx \frac{R_d}{R_v}\frac{e}{p}, \tag{3.9}$$

[3]As shown by Figure 3.4c, blackbody emission is strongest between 150-1000 cm^{-1}: that is, the spectral region to the right of the peak in the water vapor rotation band and to the left of the vibration-rotation band.

[4]This range of $\tilde{\kappa}_{ref}$ is significant because wavenumbers with these values are centered over the peak in the background Planck emission.

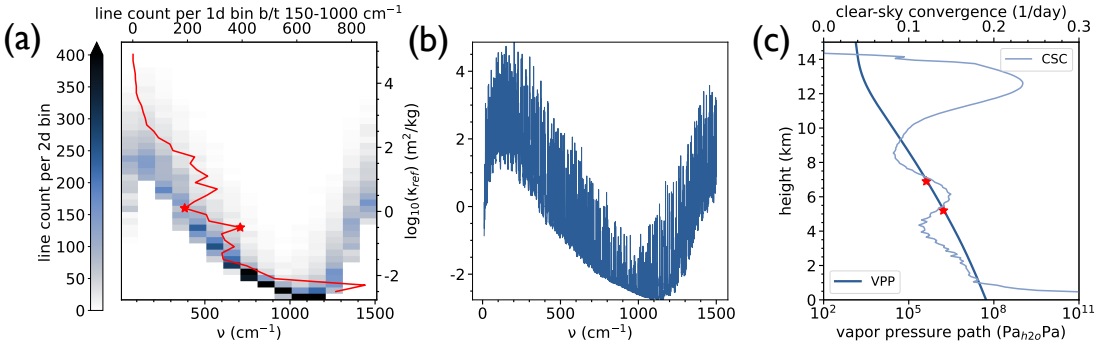

Figure 3.5: (a) 2D histogram of $\log_{10}(\tilde{\kappa}_{ref})$, representing the density of absorption lines in wavenumber-$\log_{10}(\tilde{\kappa}_{ref})$ bins. 1D histogram of $\log_{10}(\tilde{\kappa}_{ref})$ over a single spectral bin between 150-1000 cm^{-1} as a red line. Red stars identify a sharp drop in line density between 0.3-1.1 m^2/kg. (b) Logarithm of reference absorption coefficient $\log_{10}(\tilde{\kappa}_{ref})$ at 500 hPa and 260 K. (c) Vapor pressure path (Equation 3.10) as a function of height in dark blue. The red stars denote the theoretical value of VPP at the CSC peak (Equation 3.11).

defining the vapor pressure path (Hartmann et al., 2022) as

$$\text{VPP} = \int_0^p e \, dp, \tag{3.10}$$

and setting $\tilde{\tau} = 1$ (Equation 3.7), we arrive at a theoretical prediction for the VPP at the congestus level:

$$\text{VPP} = \frac{g R_v p_{ref}}{D R_d \tilde{\kappa}_{ref}}, \tag{3.11}$$

where e is the partial pressure of water vapor and R_d and R_v are the specific gas constants of dry air and water vapor, respectively. Incredibly, the VPP is a *conserved quantity* of congestus clouds because it is only a function of thermodynamic and spectroscopic constants. We solve Equation 3.11 with the idealized profiles of temperature, pressure, and humidity constructed for RFM (see Methods). This yields a height of *5.1-6.8 km* for the peak in CSC, as expected from Figure 3.5c.

We conclude that the congestus height can be extracted, line by line, from the spectral absorption coefficient, $\tilde{\kappa}$. Our approach underscores how the VPP is an incredibly useful

vertical coordinate for diagnosing the cloud height on Earth. The relationship between VPP and cloud height (Equation 3.11) was previously exploited by Spaulding-Astudillo & Mitchell (2023b) in order to explain why the VPP is fixed at the high anvil cloud level in one-dimensional radiative-convective equilibrium simulations as atmospheric water content was varied. Their solution in terms of VPP (Equation 3.11) is a variation of an earlier one introduced by Jeevanjee & Fueglistaler (2020b) that is based on an analytical approximation to the water vapor path (WVP).

3.6 Congestus invigoration by low mid-tropospheric RH

In nature, the congestus mode persists in the low RH of the tropical mid-troposphere. The vertical distribution of RH in the tropics is the result of a competition between subsidence drying and convective moistening (Romps, 2014). The dominant mechanism switches from subsidence drying to convective moistening around 7.5 km in the tropics, producing the characteristic "C-shape" in reanalyses (Figure 3.1e) and global climate models (Lang et al., 2021). In the previous section, we learned that water vapor spectral features encode the height of tropical congestus clouds. Remarkably, we arrived at this result using RFM in an idealized setup with a constant lapse rate of 7 K/km and a uniform RH of 75%.

What effect does the "C-shape" in the vertical profile of RH have on the congestus mode? Observations and cloud-resolving model simulations indicate that more mid-level clouds and fewer upper-level clouds occur in regions of relatively lower mid-tropospheric humidity (Redelsperger et al., 2002; Takemi et al., 2004; Kumar et al., 2014; Sokol & Hartmann, 2022). For the first time, we quantify the effect of the "C-shape" by incrementally reducing the mid-level RH in RFM experiments. Figures 3.6a,c demonstrate that reducing the mid-level RH significantly enhances the CSC at mid-levels and reduces CSC at upper-levels relative to the RFM experiment with uniform RH. The increase in CSC in the mid-troposphere is easy to understand. Below 7.5 km, water vapor abundance decreases more rapidly with height

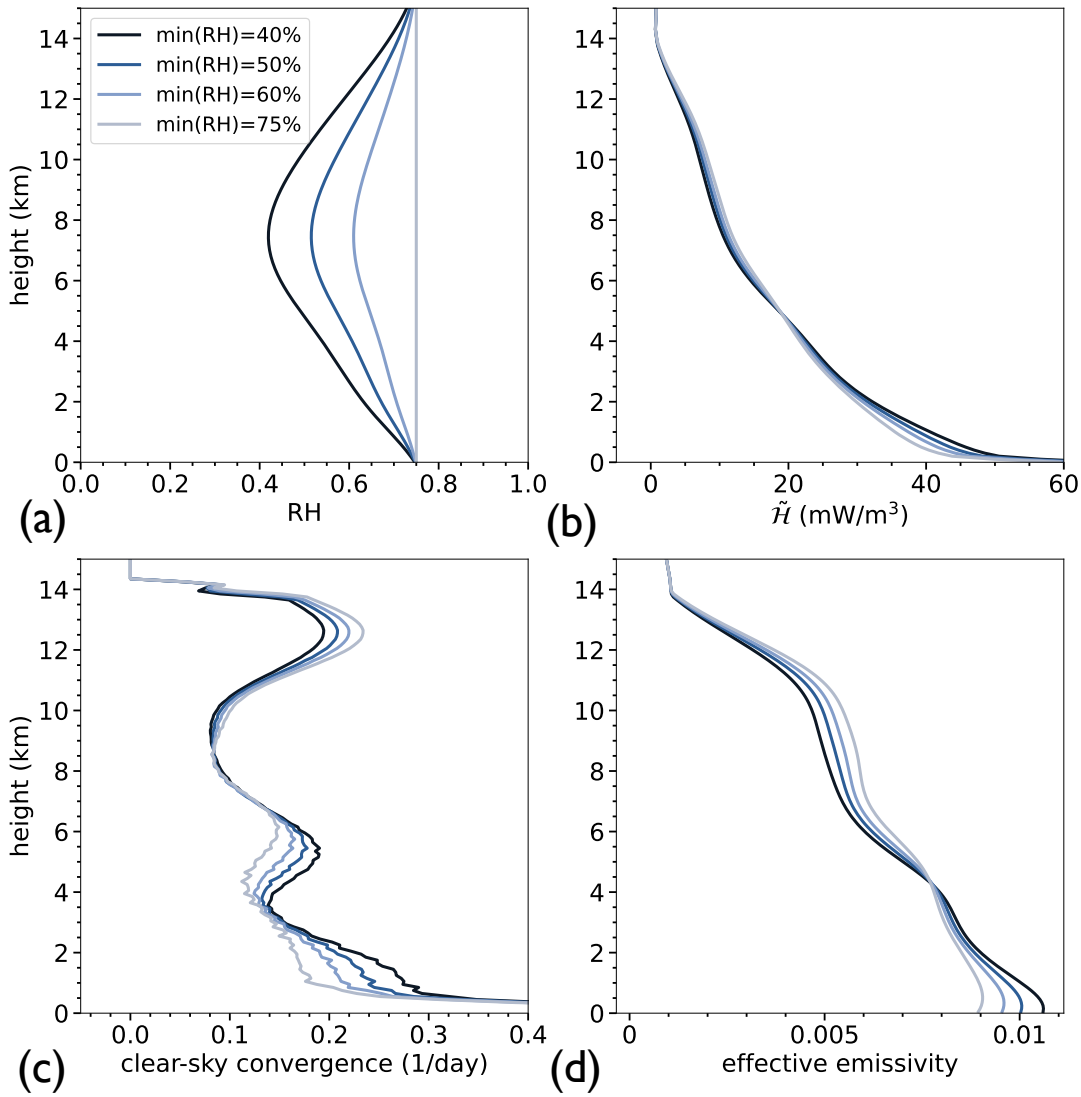

Figure 3.6: We show the effect of (a) varying RH on the (b) RFM cooling rate $\mathcal{H}$ (Equation 3.5), (c) clear-sky convergence (Equation 3.4), and (d) effective emissivity (Equation 3.12). All data are from the h2o and h2o-C scenarios.

than when the RH is constant, leading to a faster decline in $\tilde{\tau}$ with height. As a result, $-\partial_z \ln \tilde{\tau}$ (Equation 3.6) increases below 7.5 km relative to the case with fixed RH (not shown), increasing $\partial_z \mathcal{H}$ (Figure 3.6b). The opposite is true above 7.5 km. There is also a downward shift of the mid-level CSC peak with decreasing mid-level RH in Figure 3.6c from 6.0 km at 75% constant RH to 5.3 km at 40% mid-tropospheric RH, where the latter is more consistent with observations and climate re-analyses (Figures 3.1d,e). The downward shift can be explained by the fact that a drier troposphere increases the path length between the top of the atmosphere and any given optical depth. The slight descent of $\tilde{\tau} \approx 1$ levels in the water vapor rotational band (not shown), which represent the majority of the tropospheric cooling, also displaces the mid-level region of fastest decline in $\mathcal{H}$ (Figure 3.6b). In summary, a drier mid-troposphere drives more CSC and this mechanism should lead to more mid-level clouds.[5]

Our spectral interpretation of congestus enhancement is consistent with the arguments of Sokol & Hartmann (2022), namely that the congestus mode is invigorated by convective aggregation in cloud-resolving model simulations. The two consequences of aggregation that lead to congestus invigoration in their study are a decrease in the mid- and upper-level RH and a more rapid decrease in radiative cooling across the congestus level. They refer to the mechanism underlying congestus invigoration in their simulations as the "radiative-divergence feedback". Our line-by-line experiments with RFM bring additional clarity to the origin of this feedback. Congestus invigoration stems from two fundamental sources: (1) a narrowing of the emitting width in the water vapor rotation band that gives rise to a peak in CSC at 6 km and (2) a mid-level reduction in RH that hastens the decline in $\mathcal{H}$ across the congestus level. Sokol & Hartmann (2022) find convective aggregation enhances the latter.

[5]Decreasing the RH in clear-sky regions is likely to reduce the cloud lifetime simultaneously (Seeley et al., 2019b), so this argument holds to the extent that increases in sources of cloud water dominate over the sinks.

3.7 Implications for the representation of mid-level clouds in global climate models

There is a clear need to better understand cloudiness in varied environmental and dynamical conditions on Earth because clouds are crucial to the atmospheric energy and moisture budgets. In fact, clouds remain the largest source of uncertainty in estimates of Earth's climate sensitivity to anthropogenic carbon dioxide emissions (Ceppi & Nowack, 2021). The range of spatial and temporal scales over which clouds form and evolve in response to the complex interaction of cloud microphysics with radiation, convection, and large-scale dynamics make clouds, arguably, the most difficult part of the climate system to represent faithfully in climate models. In Figure 3.1, we compare the zonal-mean tropical cloud fraction from CloudSat/CALIPSO and two reanalysis products: ERA5 and MERRA-2; reanalyses are produced using global climate model simulations that are nudged towards real observations. Figure 3.1 reveals the well-known problem that reanalyses often underestimate the mid-level cloud fraction and/or fail to resolve the mid-level peak (Miao et al., 2019; Bodas-Salcedo et al., 2008). Models that do not resolve cloud-scale motions (e.g., general circulation models) rely on parameterizations or "schemes" to calculate cloud fraction. Parameterizations compute the unresolved, sub-grid scale variability of a climate variable in terms of resolved, grid scale quantities (Smith, 1990). Even so-called cloud-resolving models (CRMs) employ parameterizations for the cloud microphysics, which occur at spatial scales several orders of magnitude smaller than the finest model resolution. In the simplest cloud schemes, a unique relationship between the grid scale RH and sub-grid scale cloudiness is assumed, thus enabling the latter to be diagnosed from the former. This longstanding assumption is backed by considering the statistics of unresolved sub-grid scale fluctuations in RH. Spatial variations in moisture and temperature over sub-grid scales yield regions where the humidity is greater than or less than the local saturation value (Tompkins, 2005), which should result in fragmented patches of cloud and clear-sky that are unresolved by the climate model. As

the mean RH increases, it follows that a greater fraction of the grid cell should be cloudy. This argument is entirely valid for stratiform clouds, but it has been long recognized that the same argument likely does not extend to convective clouds (Tompkins, 2005), which form and evolve in response to different physical processes (Sundqvist, 1988). The widespread adoption of RH-based schemes in climate models has made it commonplace to interpret high cloudiness within the model as a symptom of high RH (Spaulding-Astudillo & Mitchell, 2023b). The congestus mode is a clear contradiction of this paradigm.

In the previous section, we demonstrated that the physics of clear-sky radiative transfer produce a *negative* correlation between mid-level RH and mid-level cloudiness. However, in most, if not all, cloud schemes, a positive correlation between the RH and cloudiness is assumed. This raises an important question: can the representation of mid-level clouds be improved by designing parameterizations that take into account the observed anti-correlation between RH and mid-level cloudiness? Our proposed mechanism of congestus enhancement in Section 3.6 suggests this is a promising direction for future study.

3.8 Discussion

The processes that control the height and abundance of congestus clouds have been debated for some time. Two buoyancy-based theories that have contributed significantly to our understanding are the dry air entrainment theory and the weak stability theory. In observational and modeling studies, these theories have been used successfully to show that the buoyancy of convective clouds can be reduced through dry air entrainment and/or melting of cloud ice at the freezing level. These preceding theories individually fall short in offering a comprehensive explanation for two phenomena: first, that congestus clouds peak at 5-6 km and, second, that they are invigorated by low mid-tropospheric RH. Therefore, the aim of this study has been to forge a complementary perspective of cloud formation that can explain a greater array of the observations. We do so starting from scale-invariant assumptions of

mass and energy conservation that are satisfied in the tropics in the climatological average (Jakob et al., 2019).

The central result of this work is that a decrease in the spectral emitting width of water vapor is the cause of a local, rapid decrease in the clear-sky cooling rate that, in turn, produces a peak in clear-sky convergence (CSC) between 5-6 km, a region associated with congestus cloud formation in the tropics (Wall et al., 2013). The CSC theory is derived from the basic building blocks of mass and energy conservation in radiative-convective equilibrium. It offers a simple, physical explanation for enhanced convective detrainment at specific heights of the atmosphere. In Section 3.5, we showed that the height of congestus clouds may be inferred from the density of absorption lines in the water vapor rotation band. Specifically, we derived a simple physical relationship between the vapor pressure path and thermodynamic and spectroscopic constants that together yield an accurate estimate of the mid-tropospheric peak in CSC (Figure 3.5c). In Section 3.6, we demonstrated that a drier mid-troposphere creates larger gradients in radiative cooling that, in turn, drives more convective outflow at mid-levels and less at upper-levels, consistent with the observations. Our conclusions are based on theoretical considerations and results obtained from a line-by-line radiative transfer model.

However, there is still a need for a comprehensive assessment of our congestus formation theory using a cloud-resolving model. One possible path forward is through a mechanism-denial experiment. This could involve deliberately manipulating the absorption coefficient distribution of water vapor to maintain a constant emission width across the spectral range linked to the congestus mode. If our spectral hypothesis for the origin of congestus clouds is correct, this alteration would lead to the disappearance of the peak in mid-level cloud fraction.

While it is well established that CSC supplies cloud water to clear-sky areas, it is important to note that our analysis does not also include sinks of cloud water such as precipitation and re-evaporation. The sink processes are thought to wield an equally influential role as the

sources in shaping the time-mean cloud fraction (Seeley et al., 2019b; Beydoun et al., 2021; Jeevanjee & Zhou, 2022). The lifetime of mid-level clouds, for example, is likely to shorten as the RH decreases, in competition with the increase in CSC that we see in Figure 3.6c. Diagnosing the change in tropical cloud fraction as a function of environmental conditions such as surface temperature, carbon dioxide concentration, and mid-level RH therefore requires an accurate accounting of both cloud sources and sinks. This task we leave to future work.

Under the convectional view, a decline in emissivity with height is required for anvil cloud formation. We define an effective emissivity ϵ for a hypothetical, spectrally-uniform layer of thickness $\Delta z = 100$ m:

$$\epsilon(z) = \frac{\Delta z \int_{150cm^{-1}}^{1000cm^{-1}} \pi \tilde{B} \times \frac{-\partial \ln \tilde{\tau}}{\partial z} \times \tilde{\tau} \exp(-\tilde{\tau}) d\nu}{\int_{150cm^{-1}}^{1000cm^{-1}} \pi \tilde{B} d\nu} \tag{3.12}$$

These terms should look familiar, as they also appear in Equation 3.6. The conventional view finds validation in Figure 3.6d where we see that the middle and upper layers of convective outflow coincide with declining emissivity. In typical conditions where temperature decreases with height, a strong decline in emissivity with height tells us to expect strong clear-sky convergence. The mechanism that sets the height of congestus clouds is the same as that for the highest cloud anvils. In at least two regions of the troposphere, between 5-6 km and above 11 km or so, water vapor has fewer strong absorption lines. The decrease of line density in the water vapor rotation band is ultimately the cause of the rapid decline in $\mathcal{H}$ at both middle and upper levels that we associate with anvil cloud formation.

CHAPTER 4

The emergence of relaxation-oscillator convection on Earth and Titan

In relaxation-oscillator (RO) climate states, short-lived convective storms with torrential rainfall form and dissipate at regular, periodic intervals. RO states have been demonstrated in two- and three-dimensional simulations of radiative-convective equilibrium (RCE), and it has been argued that the existence of the RO state requires explicitly resolving moist convective processes. However, the exact nature and emergence mechanism of the RO state have yet to be determined. Here, we show that (1) RO states exist in single-column-model simulations of RCE with parameterized convection, and (2) the RO state can be understood as one that has no equilibrium solutions of a zero-buoyancy heat engine model of convection. As with model simulations with resolved convection, these simpler, one-dimensional models of RCE clearly demonstrate RO states emerge at high surface temperatures and/or very moist atmospheres. The RO state emerges when the equilibrium condition of a natural heat engine is violated, in which the heat of condensation released by convective motions exceeds the work performed by the heat engine. The proposed mechanism for RO emergence is general to all moist planetary atmospheres, is agnostic of the condensing component, and naturally leads to an understanding of Titan's bursty methane weather.

4.1 Introduction

Earth's tropics are characterized by a steady balance between heating by moist convection and radiative cooling, which is known as *quasi-equilibrium* (QE; Emanuel, 2008; Arakawa & Schubert, 1974). QE states exhibit continuous, deep convection and small, random fluctuations in clouds and precipitation about the mean. In Chapter 1, we pointed out that the pattern of global-mean precipitation on Earth is distinct from that on Saturn's moon Titan (Figure 1.2). Titan is thought to have a mostly dry climate that is disrupted at quasi-periodic intervals by massive storms. We likened Titan's bursty methane weather to the canonical *relaxation oscillator* (RO) waveform. A new mode of convection on Earth with quasi-periodic oscillations was recently discovered for high surface temperatures in three-dimensional, cloud-resolving model simulations of radiative-convective equilibrium (3D-RCE; Seeley & Wordsworth, 2021, henceforth SW21). In this new RO mode of convection, storms erupt at regular intervals with vigorous, short-lived rainfall, separated by dry, cloud-free spells. Although the RO state is not a feature of the modern climate, significant time-variation in convective storms have been observed or simulated in a variety of planetary environments: from Jupiter (Sugiyama et al., 2014) and Saturn (Li & Ingersoll, 2015; Fischer et al., 2011) to Titan (Schaller et al., 2009; Turtle et al., 2011b) and the hothouse Earth (SW21). Therefore, the physics underlying the dynamics of convecting atmospheres may be more general than once thought.

This study offers the first thermodynamic explanation for the differing patterns of precipitation on Earth and Titan. Observations and theory predict that the precipitable moisture in the atmospheres of Earth and Titan differs by, at least, two orders of magnitude (Tokano et al., 2006; Hartmann, 2016a). We will show that increasing the amount of condensable in an atmosphere causes the transition from QE to RO convection. The findings of Seeley & Wordsworth (2023) imply that such a transition may occur on Earth in the distant future through an increase in the surface temperature from solar brightening. A major consequence

of this surface warming is an increase of atmospheric moisture content. Since the RO state is, by definition, non-steady, it suggests that we may conceive of the QE-to-RO transition as a *breakdown of steady-state quasi-equilibrium*. To look for a breakdown of steady-state convection with increasing surface temperature and/or moisture content, what is needed is a plausible model of a convecting atmosphere, which we detail in Sections 4.4.1 and 4.4.2.

The structure of this paper is as follows. In Section 4.2, we describe the single column model (SCM) used to vary surface temperature and/or moisture content in a one-dimensional Earth-like atmosphere in radiative-convective equilibrium (1D-RCE). In Section 4.3, we show that RO states emerge in 1D-RCE simulations at a surface temperature of 350 K. Our results challenge a previous finding that RO emergence requires conditions that support net radiative heating of the lower tropsphere. In Section 4.4, we propose a new theory of RO emergence that merely outlines the conditions necessary for a breakdown of quasi-equilibrium. In order to determine what these conditions are, we combine two theories of quasi-equilibrium convection - convection is conceived as a natural heat engine in one theory (Section 4.4.1) and as an ensemble of zero-buoyancy plumes in the other (Section 4.4.2) - and we test the zero-buoyancy heat engine theory against our 1D-RCE simulations. We discuss our findings in Section 4.5. To illustrate the flexibility of our approach, we test it in Section 4.6 against a completely different moist-convective system: methane on Titan.

4.2 Methods

SW21 propose that the physical ingredients required for RO states are (i) realistic radiation, (ii) clouds, (iii) convection, and (iv) large-scale condensation and re-evaporation; they further speculate that RO states require model simulations with resolved convection, i.e., a model of 3D-RCE. These four ingredients, however, are not unique to 3D-RCE – all of them can be parameterized in simpler models of RCE. In this paper, we demonstrate the existence of RO states in a single-column model of RCE, i.e., 1D-RCE.

We use a version of the ECHAM6 GCM in single-column mode that has been modified to allow water vapor to comprise a significant fraction of the atmospheric mass (Popp et al., 2015, henceforth P15) and the SVP of water to be multiplicatively altered (Spaulding-Astudillo & Mitchell, 2023b). The single-column model has separate schemes for radiation, convection, and clouds. Shortwave and longwave radiation is resolved into 14 and 16 spectral bands by the Rapid Radiative Transfer Model for General Circulation Models (RRTMG - Iacono et al., 2008). All phases of water are prognostic and accounted for in the radiation calculation. As in P15, we use an exponential extrapolation of all molecular absorption coefficients in the longwave and the H2O self-broadened absorption coefficients in the shortwave for temperatures above which no data in the original model exists. The effect of pressure broadening by water vapor is neglected. Convection is represented by a bulk-plume scheme (Tiedtke, 1989; Giorgetta et al., 2013) that parameterizes turbulent entrainment and detrainment of air between updrafts, downdrafts, and the environment. Clouds are formed by a large-scale condensation and re-evaporation scheme (Sundqvist et al., 1989) as a function of the relative humidity of the environment.

In our minimal-recipe experiment, the insolation is set 10% higher than the present-day value and is temporally fixed (no diurnal or seasonal cycle). We set the column latitude to 38°N, where the globally-averaged insolation is the same as the local value. Clouds are the only source of time-varying planetary albedo. The atmosphere is composed *only* of nitrogen, oxygen, and water vapor. We use a time step of 60 s and run the simulations for approximately 200 years. The sea surface temperature (SST or T_s) of a 1 m mixed-layer ocean with an albedo of 0.07 is fixed at every time step through the use of an artificial surface heat sink. We vary the fixed T_s in 1-5 K increments from 290 to 370 K. In Section 4.3, we detail the results of increasing T_s in 1D-RCE simulations with the ECHAM6 SCM.

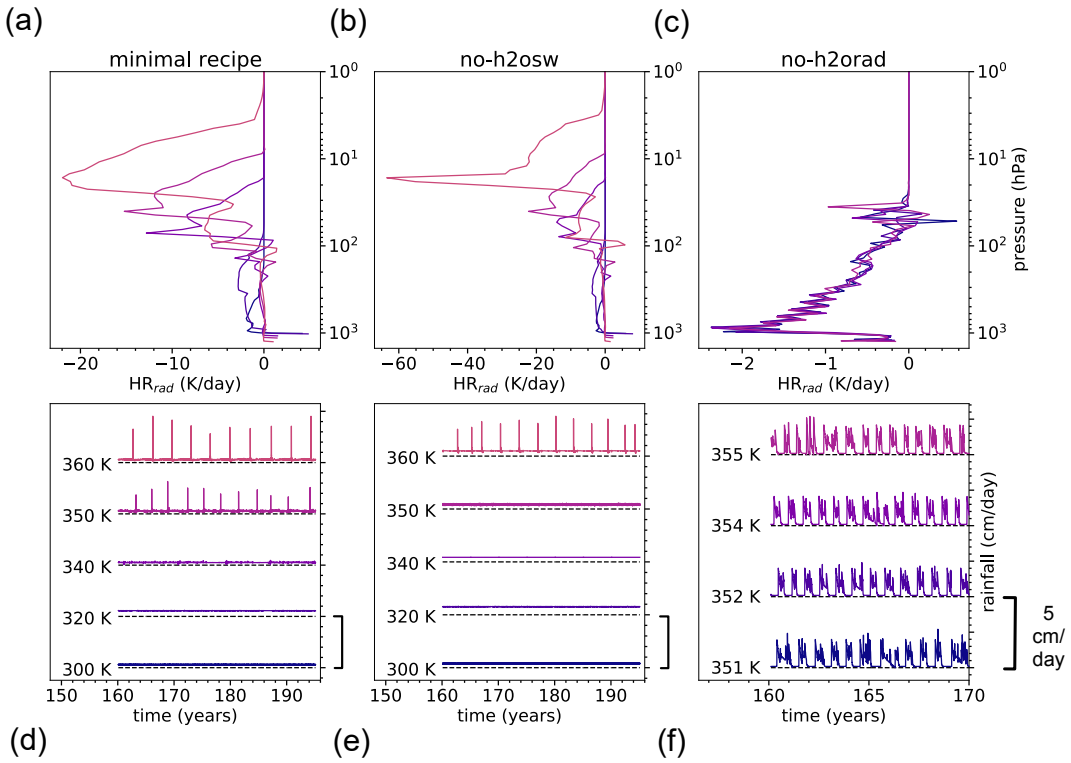

Figure 4.1: Displays (left to right) the minimal recipe, no-h2osw, and no-h2orad single column experiments with fixed SSTs between 300-360 K. The top row is net radiative temperature tendency in K/day. The bottom row is a time-series of rainfall rates in cm/day over a 30 year period. Rainfall rates at each SST are vertically offset by 5 cm/day and a zero rainfall contour is given for reference as a dashed black line.

4.3 Results of 1D-RCE simulations

4.3.1 Description of RO states

Figure 4.1d clearly shows that our single column, minimal-recipe simulations transition into RO states at a surface temperature around $T_s = 350$ K. At cooler temperatures, precipitation is steady and continuous and hovers around a mean value of 2-6 mm/day; these simulations are in the QE regime. RO states exhibit large bursts of precipitation with intensities up to 5 cm/day that repeat every $O(100)$-$O(1000)$ days and that are relatively short-lived (10-30 days).[1] Consistent with 2D (Sugiyama et al., 2014) and 3D (SW21) simulations of oscillatory climate states, 1D-RCE RO states cycle through 3 phases: a rapid convective phase (RCP), a slow cooling phase (SCP), and a triggering phase (TP).

In the RCP, deep convection rapidly heats and moistens the atmosphere above the boundary layer at $O(1)$-$O(10)$ K/day (Figure 4.2b). The storm generates a spike in rainfall resembling a delta function that is 10-20 times stronger than the mean background rate (Figure 4.2d). Strong warming disrupts cloud formation by reducing the column relative humidity, contributing to a sharp drop in vertically-integrated cloud water of 1-2 orders of magnitude (Figure 4.2a). Low-level temperature inversions in our warmest simulations are a clear source of convective inhibition that form during the RCP and are slowly eroded during the subsequent SCP; such inversions are common to the so-called moist greenhouse state (Wolf & Toon, 2015; Popp et al., 2015; Wordsworth & Pierrehumbert, 2013).

During the SCP, the atmosphere cools radiatively from its upper layers. The lower layers are water-dominated and thus are unable to cool directly to space because of their high infrared opacity. Top-of-atmosphere radiative cooling is communicated to the lower layers through the re-evaporation of precipitation; re-evaporation destablizes the atmosphere from the top down, building CAPE in the process (Figure 4.2c,d). The increase in CAPE is

[1]The storm duration is calculated as the number of contiguous days where the precipitation rate is above the mean value.

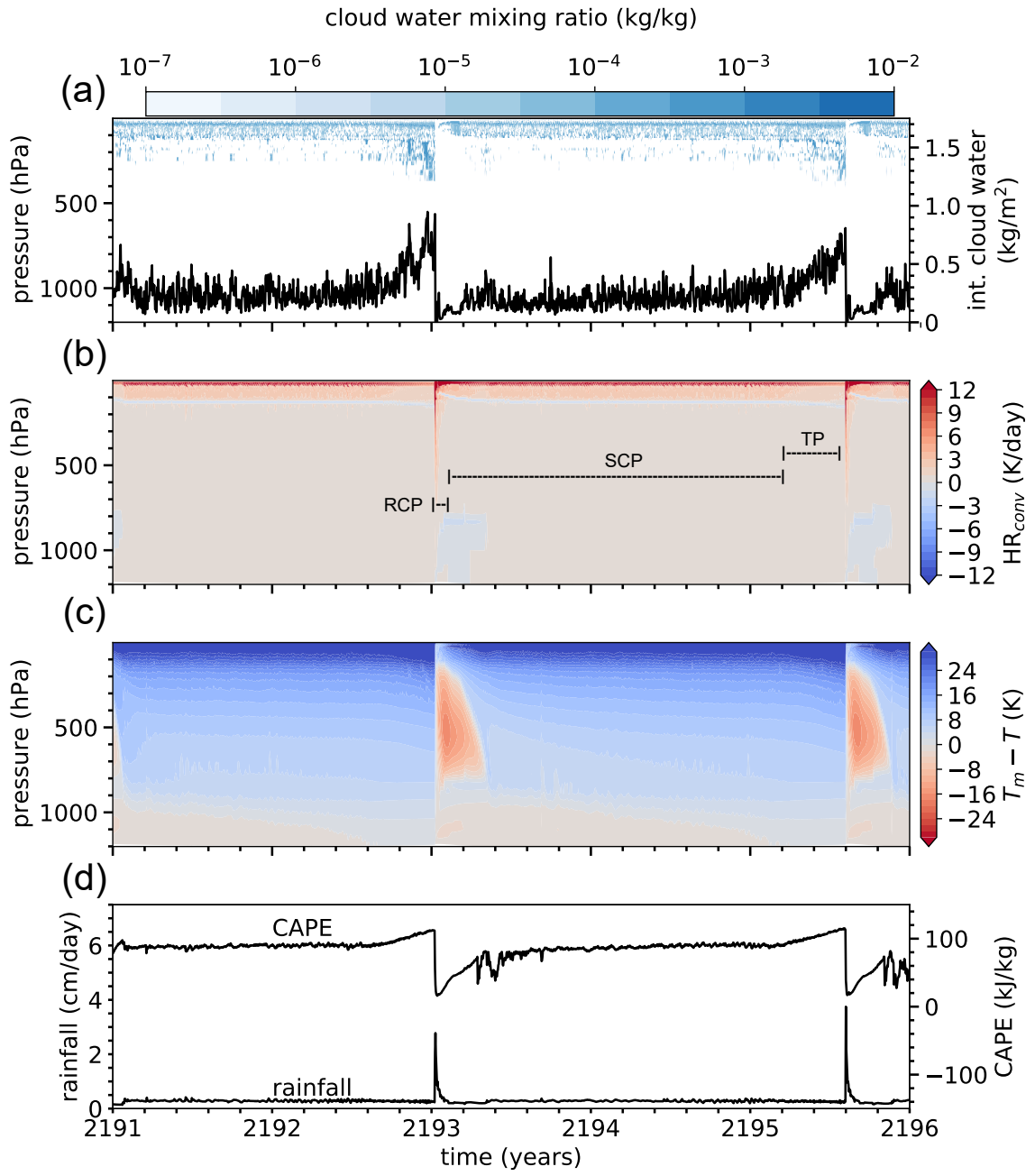

Figure 4.2: Time series of the minimal-recipe experiment over 5 years at $T_s = 355$ K. Depicts (a) cloud water mixing ratio in color and vertically-integrated cloud water in black. (b) Temperature tendency from the convection scheme in K/day. (c) Difference in temperature between a parcel lifted from the surface along the moist pseudo-adiabat and the environment. This is a proxy for the atmospheric instability. (d) Rainfall rate and convective available potential energy (CAPE).

evident in a time series of the difference in temperature between the environment and the moist pseudo-adiabat of a parcel lifted from the surface (Figure 4.2c). Total cloud cover steadily increases over the SCP (Figure 4.2a).

The TP begins when the troposphere is everywhere unstable with respect to surface-based, pseudo-adiabatic moist convection (Figure 4.2c). A striking feature of the TP is the rapid descent of the cloud base (Figure 4.2a), which has been observed in other numerical studies of oscillatory climate states (SW21, Sugiyama et al., 2014). Vertically-integrated cloud water quadruples during this period (Figure 4.2a), which could be related to the troposphere nearing saturation. Eventually, the built-up CAPE is released (Figure 4.2d) and the cycle repeats from the RCP.

The inhibitive cap that exists during the SCP is slowly eroded away by the TP (Figure 4.2c). Paradoxically, CAPE continues to grow during the TP with no apparent convective inhibition mechanism (Figure 4.2d). In fact, the TP typically represents over 25% of the quiescent period. This means that there is a significant delay between when the troposphere becomes globally unstable and when the next storm begins. This apparent paradox suggests that we have thus far overlooked an emergent constraint on deep convection, which we will return to in Section 4.4.

4.3.2 RO states occur in the absence of lower-tropospheric radiative heating

SW21 hypothesize that lower-tropospheric radiative heating (LTRH) that emerges in hot climate states is essential for the emergence of RO convection; LTRH is a consequence of strong shortwave absorption by water vapor. By enforcing LTRH in fixed SST 3D-CRM simulations, SW21 observed that RO states emerged at SSTs over 20 K less than their default experiment.

To test the LTRH hypothesis, we ran two separate mechanism-denial experiments in which we zero out the contribution of water vapor in the SW radiative calculation ("no-

h2osw" experiment) and one in which it is zeroed out in the SW and LW radiative calculation ("no-h2orad" experiment). The lower troposphere remains opaque to infrared radiation in the no-h2osw experiment and consequently net cooling rates there remain close to zero (Figure 4.1b). In contrast, the whole troposphere radiatively cools in the no-h2orad experiment (Figure 4.1c). In both the no-h2osw and no-h2orad experiments, we found that RO-like states still occur (Figures 4.1e,f). From these mechanism-denial experiments, we conclude that the radiative effects of water vapor influence RO states, but they do not tell the whole story. We suspect that a previously-unrecognized constraint on convection produces the RO phenomenon over warm SSTs, which we now detail.

4.4 The mechanism for the emergence of RO states

The QE state is characterized by a steady balance between the generation of CAPE by radiation and its destruction by convection. The RO state is clearly not steady, however we posit that exploring the conditions in which a steady, QE state is valid can illuminate the mechanisms that lead to the transition from QE to RO convection. We carry this out quantitatively in Section 4.4.1, but first consider heuristically how the dynamics of RO convection would differ from the QE state. Essential to the QE state is the ability of radiative cooling to keep pace with the more rapid convective heating. In warm and/or humid conditions, however, the fast convective process releases an amount of latent energy that the slower radiation cannot keep pace with. The sudden release of this heat, $\langle r \rangle$, in convection would naturally stabilize the atmosphere and shut off convection until radiation can restore buoyancy. CAPE would necessarily be time-dependent, undergoing large oscillations bounded above by $\langle r \rangle$. In this picture, the RO state emerges when $\langle r \rangle$ exceeds the value of CAPE that would be present in the QE regime. Thus, a predictive model of RO emergence requires a plausible model of steady-state RCE.

Just such a model of QE convection was introduced by Emanuel & Bister (1996) (hence-

forth EB96), which conceives of convection as a natural heat engine. Heat absorbed at the warm surface and lost from the colder upper atmosphere is converted into work (vertical motion of air) by the convective heat engine. A necessary condition of equilibrium is that the heat ($\langle r \rangle$) must be converted into work (CAPE) at an efficiency η. To estimate CAPE and $\langle r \rangle$ as a function of surface temperature, we use another steady-state model of convection that has gained traction in recent years (Singh & O'Gorman, 2013; Romps, 2014, 2016; Seeley & Wordsworth, 2023). Romps (2016, henceforth R16) conceives of a saturated, convective plume interacting with a sub-saturated environment with which it has zero buoyancy – the so-called "zero-buoyancy model" (ZBM) – a condition that is supported by observations in the tropics and in cloud-resolving models simulations (see Section 4.4.2 for a derivation of the ZBM.). The ZBM predicts the steady value of CAPE that would be present in QE for a given surface temperature and a set of convective parameters. It's important to note that the CAPE predicted by the ZBM represents a steady-state storage of buoyancy, not the rate of CAPE generation and destruction by radiation and convection. Furthermore, the ZBM predicts a maximum in CAPE at intermediate, warm surface temperatures, which are explored quantitatively in the following sections. Concurrently, increasing the SST would naturally increase water vapor, and we will show that the latent heat release by convection in the ZBM, $\langle r \rangle$, increases monotonically with surface temperature. Thus, $\langle r \rangle$ inevitably exceeds the steady value of CAPE above a certain SST; above this SST, the QE state is no longer viable. Our hypothesis is that the RO state is preferred in this SST regime.

In Section 4.4.1, we derive the heat engine model of EB96. In Section 4.4.2, we derive the zero-buoyancy model of R16 and describe how we use it to estimate CAPE and $\langle r \rangle$ as a function of SST, and convective and thermodynamic parameters. We then test our hypothesis for the emergence of RO states by seeking the answers to the questions: (1) Under what conditions does $\langle r \rangle$ diverge from CAPE in the ZBM?; and (2) Is the point of divergence between $\langle r \rangle$ and CAPE predictive of the emergence of RO states in simulations as indicated by the heat engine model of convection?

4.4.1 Theory 1: convection as a heat engine

First, we summarize a theory of convection developed by Emanuel & Bister (1996). The theory conceptualizes convection as an ensemble of plumes rising in cloudy regions and descending in clear-sky regions. Since air is compressible, plumes expand as they rise, performing work on the environment. Radiative-convective equilibrium is defined as a *statistical* equilibrium between radiative and convective sources of heating and cooling. In equilibrium, the mass-integrated radiative cooling of the atmosphere ($\overline{Q}_A$; Wm^{-2}) balances surface heating ($\overline{Q}_s$; Wm^{-2}):

$$\overline{Q}_s + \overline{Q}_A = 0 \ , \tag{4.1}$$

where bars denote mass-weighted averages. The surface heating is

$$\overline{Q}_s = SW_{toa} - \Delta SW - LW_0, \tag{4.2}$$

where SW_{toa} is the net downward solar radiation at the top of the atmosphere, ΔSW is the solar radiation absorbed in the atmosphere, and LW_0 is the net upward longwave radiation at the surface. The atmospheric cooling is

$$\overline{Q}_A = LW_0 + \Delta SW - LW_{toa}, \tag{4.3}$$

where LW_{toa} is the net upward longwave radiation at the top of the atmosphere.

Following EB96, we assume radiative processes are thermodynamically reversible. Low entropy radiation is absorbed at the surface and high entropy radiation is emitted from the atmosphere at temperatures T_s and $\overline{T}_{rad}$, respectively (Singh & O'Neill, 2022). Thus, radiative processes contribute a net sink of specific entropy (s; $\mathrm{Jkg}^{-1}\mathrm{K}^{-1}$) from the Earth climate system (defined as the surface and atmosphere),

$$\frac{1}{g}\int \left(\frac{\partial s}{\partial t}\right)_{rev} dp = \frac{\overline{Q}_s}{T_s} + \frac{\overline{Q}_A}{\overline{T}_{rad}} = \overline{Q}_A\left(\frac{1}{T_s} - \frac{1}{\overline{T}_A}\right). \tag{4.4}$$

Following EB96, we assume that the only source of entropy in the system is the dissipation of kinetic energy in convective turbulence. In statistical equilibrium, the vertical integral of

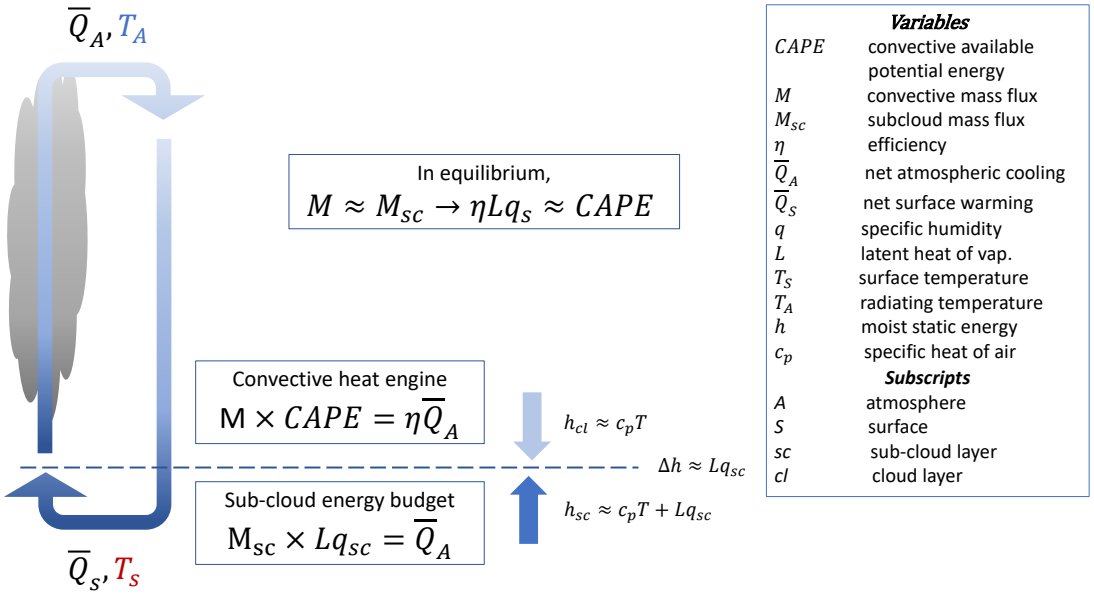

Figure 4.3: Illustration of the convective heat engine model of Emanuel & Bister (1996). Heat entering the system at the warm surface temperature T_S and leaving the system at the cold radiating temperature T_A is converted into work ($M \times$CAPE) at an efficiency η. The mass flux in the heat engine is assumed to be constant with height. The mass flux is equal to $\eta \overline{Q}_A$/CAPE. The sub-cloud energy budget constrains the mass flux out of the boundary layer M_{sc} equal to $\overline{Q}_A / L q_{sc}$. No net vertical transport of mass in equilibrium requires $M \approx M_{sc}$, which implies that $\eta L q_s \approx$ CAPE. When $\eta L q_s$ and CAPE diverge with increasing surface temperature, it violates the equilibrium assumption, pushing the atmosphere into the RO state.

the "kinetic energy equation" - that is, the equation describing the time rate of change of kinetic energy per unit volume - is a balance between pressure work and dissipation:

$$\int_z [-v \cdot \nabla p + \rho f \cdot v] = 0 \ , \tag{4.5}$$

where v is the velocity, p is the pressure, f is the net frictional acceleration and ρ is density. We refer to the first term in the above equation as "work" and the second as "dissipation". The units of these terms are Wm^{-3}. Dissipation is an irreversible source of entropy; assuming it occurs at an average temperature $\bar{T}_{irr}$,

$$\frac{\bar{T}_{irr}}{g} \int \left(\frac{\partial s}{\partial t} \right)_{irr} dp = - \int_z \rho f \cdot v \tag{4.6}$$

EB96 show that to a good approximation

$$\int_z -v \cdot \nabla p \approx \int_z MB \ , \tag{4.7}$$

where M is the mass flux and

$$B = g \frac{(\bar{\rho} - \rho)}{\rho} \tag{4.8}$$

is the buoyancy, $\bar{\rho}$ is the density of the environment, and ρ is the density of the working fluid; MB is the buoyancy flux (Wm^{-3}). The above imply the dissipation is equal to the buoyancy flux. Therefore, the irreversible source of entropy is

$$\frac{1}{g} \int \left(\frac{\partial s}{\partial t} \right)_{irr} dp = \frac{1}{\overline{T}_{irr}} \int_z MB \ , \tag{4.9}$$

In equilibrium, the net production of entropy must be zero, so the reversible sinks and irreversible sources must balance:

$$\overline{Q}_A \left(\frac{1}{T_s} - \frac{1}{\overline{T}_A} \right) = - \frac{1}{\overline{T}_{irr}} \int_z MB \tag{4.10}$$

If we assume the mass flux is constant, as would be the case for plumes that entrain and detrain air in equal parts with height,

$$M \int_z B = M \times CAPE \ . \tag{4.11}$$

$CAPE$ is the convective available potential energy, i.e. the part of the potential energy that is available to convert to kinetic energy. Defining $\eta \equiv \overline{T}_{irr}(1/T_s - 1/\overline{T}_{rad})$, we arrive at

$$\eta \overline{Q}_A = M \times CAPE \ . \tag{4.12}$$

The above equation can be thought of as representing a convecting atmosphere as a heat engine. The engine does work at the rate $M \times CAPE$ that is equal to the heating rate $\overline{Q}_A$ times an efficiency η. Solving for the mass flux implied by the convective heat engine,

$$M = \frac{\eta \overline{Q}_A}{CAPE} \ . \tag{4.13}$$

4.4.1.1 The subcloud mass flux

Following EB96, we divide the atmosphere into the dry convecting subcloud layer and the moist convecting cloud layer. In the two-layer model, the cooling rate sums over both layers of the atmosphere:

$$\overline{Q}_A = \overline{Q}_{A,sc} + \overline{Q}_{A,cl} \tag{4.14}$$

The enthalpy budget of the subcloud layer allows us to estimate the mass flux therein:

$$\overline{Q}_s + \overline{Q}_{A,sc} + M_{sc}(h_{cl} - h_{sc}) = 0 \ . \tag{4.15}$$

Here the subscript "sc" indicates the subcloud layer, the subscript "cl" indicates the cloud layer, h_{cl} is the average enthalpy of downdrafts, and h_{sc} is that of the subcloud layer. Mixing equal parts of air between the subcloud layer and the cloud layer implies a net upward transport of enthalpy, $h_{sc} - h_{cl}$. Solving for the mass flux from the sub-cloud layer,

$$M_{sc} = \frac{\overline{Q}_{A,cl}}{\Delta h} \tag{4.16}$$

where $\Delta h = h_{cl} - h_{sc}$.

EB96 equate M and M_{sc} to derive an expression for $CAPE$. This is clearly necessary for statistical equilibrium. Combining them, we find that equilibrium requires a statistical

Parameter	Definition	Earth-like	Titan-like
$c_{p,d}$	Specific heat of dry air at constant pressure ($\mathrm{Jkg^{-1}K^{-1}}$)	1004	1040
R_d	Specific gas constant of dry air ($\mathrm{Jkg^{-1}K^{-1}}$)	287	290
R_v	Specific gas constant of the condensable ($\mathrm{Jkg^{-1}K^{-1}}$)	462	518
L	Latent heat of vaporization of the condensable ($\mathrm{Jkg^{-1}}$)	2.26×10^6	5.5×10^5
g	Gravitational acceleration ($\mathrm{ms^{-2}}$)	9.81	1.35
T_{trp}	Tropopause temperature (K)	200	70
$p_{s,d}$	Partial pressure of dry air at the surface (Pa)	10^5	1.42×10^5

Table 4.1: Parameters used to evaluate the zero-buoyancy model (Romps, 2016) at Earth-like and Titan-like conditions. These are not necessarily the values used by ECHAM6 (Stevens et al., 2013) or the Titan Atmospheric Model (TAM - Lora et al., 2015).

balance between the conversion of latent heat into CAPE at an efficiency η:

$$M \approx M_{sc} \rightarrow \eta L q_s \approx CAPE. \tag{4.17}$$

But is there a regime where M and M_{sc} don't equal one another? Instead of using the EB96 theory to solve for $CAPE$, we use a zero-buoyancy theory of convection (Section 4.4.2; Romps, 2016) to constrain it and look for a breakdown in quasi-equilibrium, i.e. $M \neq M_{sc}$.

4.4.2 Theory 2: convection as a zero-buoyancy plume ensemble

In the zero-buoyancy theory of convection developed by Romps (2014, 2016), convection is conceived as vertical ascent of an ensemble of clouds in saturated regions and descent of clear air in the surrounding, sub-saturated environment. It was first demonstrated by Singh & O'Gorman (2013) that the vertical integral of cloud buoyancy relative to the clear-sky environment in cloud-resolving model simulations is close to zero. Based on this insight, they proposed a model of convection in which clouds are exactly neutrally-buoyant with respect to their environment. This assumption about typical cloud buoyancies is known as

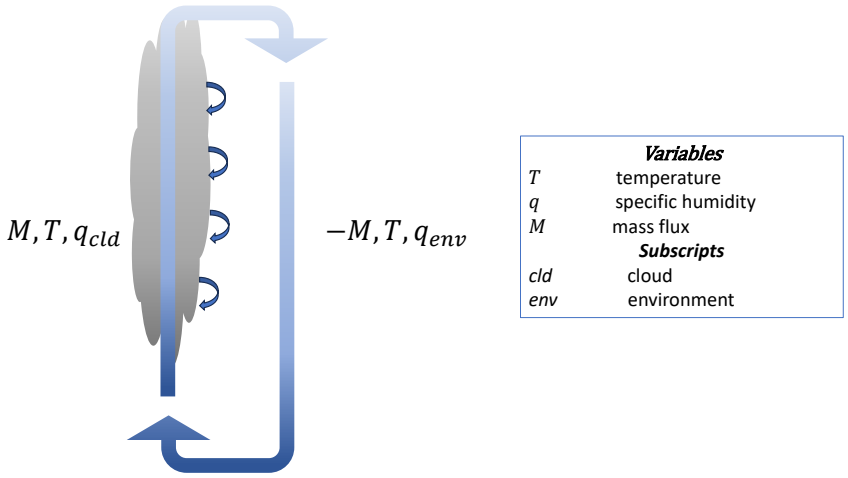

Figure 4.4: Illustration of the zero-buoyancy model of Romps (2016). Convection is conceived as a saturated plume ascending through a sub-saturated environment, entraining and detraining air as it does so. The plume and environment have the same temperature but different specific humidities. It is also assumed that the mass flux is constant with height.

the *zero-buoyancy approximation.*

A common misunderstanding of the zero-buoyancy approximation is that CAPE is also zero. This is, in fact, not true. CAPE is defined as

$$CAPE = \int_{z_s}^{z_{trp}} g\frac{\rho - \rho'}{\rho'}dz, \tag{4.18}$$

where ρ is the density of the sub-saturated environment, ρ' is the density of a saturated, pseudo-adiabatic parcel, g is gravity, and z_s and z_{trp} are the surface and tropopause elevation. What CAPE measures, therefore, is the maximum possible buoyancy of a hypothetical, non-entraining parcel that is displaced between the two heights (note that condensates are immediately removed from the ascending parcel). Equation 4.18 tells us that two variables are required to estimate CAPE: ρ' and ρ. Because parcel methods associated with pseudo-adiabatic displacement are so well defined, ρ' is easy to calculate given surface boundary conditions. What is needed to calculate CAPE, therefore, is a plausible environmental profile of ρ. Romps (2014) proposed a novel solution. They realized that the environmental ρ is equivalent to that of an entraining plume in the zero-buoyancy approximation. Their method of estimating ρ has merit because real clouds turbulently mix with their surroundings.

We now derive the zero-buoyancy model of convection in order to estimate CAPE and $\langle r \rangle$ (Singh & O'Gorman, 2013; Romps, 2016) as a function of increasing temperature and/or moisture. We start by introducing an artificial multiplier on the saturation vapor pressure (SVP) of water, ξ, following Spaulding-Astudillo & Mitchell (2023a) and McKinney et al. (2022).

$$e^*_\xi = \xi e^* \tag{4.19}$$

where e^*_ξ and e^* are the modified and true SVP of water, respectively. Moisture variables with a subscript of ξ should be understood to have an implicit ξ-dependence. The saturation specific humidity is

$$q^*_\xi = \frac{R_a}{R_v}\frac{e^*_\xi}{p}, \tag{4.20}$$

where R_a is the specific gas constant of environmental air (everywhere assumed to be that of dry air) and p is the total air pressure. Taking the vertical derivative of the natural log of e^*_ξ (and using the definition of the lapse rate $\Gamma = -\partial_z T$), we obtain

$$\begin{aligned} \partial_z e^*_\xi &= \partial_T e^*_\xi \partial_z T = -\frac{L e^*_\xi \Gamma}{R_v T^2}, \\ \partial_z \ln e^*_\xi &= -\frac{L\Gamma}{R_v T^2}. \end{aligned} \tag{4.21}$$

The vertical derivative of the natural log of p is obtained from hydrostatic balance and the ideal gas law:

$$\partial_z \ln p = -\frac{g}{R_a T}, \tag{4.22}$$

where g is gravity. Taking the vertical derivative of the natural log of q^*_ξ and plugging in Equations 4.21 and 4.22, we obtain

$$\begin{aligned} \partial_z \ln q^*_\xi &= \partial_z \ln e^*_\xi - \partial_z \ln p, \\ &= \frac{g}{R_a T} - \frac{L\Gamma}{R_v T^2} = -\gamma. \end{aligned} \tag{4.23}$$

where γ is the water vapor lapse rate.[2] The tropospheric water budget is obtained from the bulk-plume equations for convection:

$$\partial_z M = e - d - c, \text{ where } e = \varepsilon M \text{ and } d = \delta M, \tag{4.24}$$

$$\partial_z (M q^*_\xi) = e q_\xi - d q^*_\xi - c, \text{ and} \tag{4.25}$$

$$-\partial_z (M q_\xi) = d q^*_\xi - e q_\xi + \alpha c. \tag{4.26}$$

M is the convective mass flux (kg $\mathrm{m}^{-2}\mathrm{s}^{-1}$), e and d are the turbulent entrainment and detrainment rates (kg $\mathrm{m}^{-3}\mathrm{s}^{-1}$) in which ε and δ are fractional mixing efficiencies (m^{-1}), and c is the condensation rate ($\mathrm{kg}_{h2o}\mathrm{m}^{-3}\mathrm{s}^{-1}$). α is defined as the ratio of gross evaporation to gross condensation at each height, so the gross evaporation is $\alpha c/M$ and the condensation minus evaporation is $\mathrm{PE}c/M$, where $\mathrm{PE} = (1-\alpha)$ is the precipitation efficiency. We make

[2] γ^{-1} is the scale height of saturation specific humidity.

the following assumptions. The condensates not re-evaporated at each level (PE$c/M$) are immediately removed from the convective plume. The gross condensation represents a small fraction of the total updraft mass ($\partial_z M >> c$). Invoking the latter assumption in Equation 4.24 gives

$$\begin{aligned} \partial_z M &= e - d \\ &= (\varepsilon - \delta)M. \end{aligned} \tag{4.27}$$

Expanding Equation 4.25 with the chain-rule and solving for $\partial_z q_\xi^*$ (using Equation 4.27), we obtain

$$\partial_z q_\xi^* = \varepsilon(q_\xi - q_\xi^*) - \frac{c}{M}. \tag{4.28}$$

Doing the same to Equation 4.26 to find $\partial_z q$,

$$-\partial_z q_\xi = \delta(q_\xi^* - q_\xi) + \alpha\frac{c}{M}. \tag{4.29}$$

The relative humidity is $\mathrm{RH} = q_\xi / q_\xi^*$. Rearranging for q_ξ,

$$q_\xi = \mathrm{RH} q_\xi^*, \tag{4.30}$$

and taking the vertical derivative of both sides, we obtain

$$\partial_z q_\xi = q_\xi^* \partial_z \mathrm{RH} + \mathrm{RH}\partial_z q_\xi^*. \tag{4.31}$$

We assume that vertical variations in RH are much smaller than those in specific humidity ($\partial_z \mathrm{RH} << \partial_z q_\xi^*$), as is generally the case in Earth's troposphere. Invoking this assumption in Equation 4.31 gives

$$\partial_z q_\xi = \mathrm{RH}\partial_z q_\xi^*. \tag{4.32}$$

Using Equations 4.23, 4.30, and 4.32 to re-write Equations 4.25 and 4.26, we obtain

$$-\gamma q_\xi^* = \varepsilon(\mathrm{RH} - 1)q_\xi^* - \frac{c}{M} \text{ and} \tag{4.33}$$

$$\mathrm{RH}\gamma q_\xi^* = \delta(1 - RH)q_\xi^* + \alpha\frac{c}{M}. \tag{4.34}$$

To solve for RH, we substitute $\frac{c}{M}$ from Equation 4.33 into Equation 4.34.

$$\mathrm{RH} = \frac{\delta + \alpha\gamma - \alpha\varepsilon}{\delta + \gamma - \alpha\varepsilon} \tag{4.35}$$

To solve for $\frac{c}{M}$, we back-substitute Equation 4.35 into Equation 4.33.

$$c_z = \frac{c}{M} = \Big(\frac{\delta + \gamma - \varepsilon}{\delta + \gamma - \alpha\varepsilon}\Big)\gamma q_\xi^*. \tag{4.36}$$

c_z is the specific condensation per unit distance traveled by an entraining plume ($\mathrm{kg}_{h2o}\mathrm{kg}^{-1}\mathrm{m}^{-1}$). We invoke the zero-buoyancy assumption (ZBA; Singh & O'Gorman, 2013) to define the moist static energy (MSE) of the environment and the plume.

$$h_\xi = c_p T + gz + Lq_\xi \tag{4.37}$$

$$h_\xi^* = c_p T + gz + Lq_\xi^* \tag{4.38}$$

The ZBA is that convective plumes are neutrally buoyant with respect to their environment. Strictly speaking, this means that their *virtual* temperatures are the same. When virtual effects are neglected, as is done here, the plume and the environment possess the same temperature T such that their MSEs differ only by the differences in their specific humidities. c_p is the specific heat of the atmosphere (assumed to be dry air, $c_{p,d}$). Next, taking the vertical derivative of h_ξ^* (and using $\Gamma = -\partial_z T$, $\partial_z q_\xi^* = -\gamma q_\xi^*$, and Equation 4.23),

$$\begin{aligned} \partial_z h_\xi^* &= -c_p\Gamma + g - L\gamma q_\xi^* \\ &= g\Big(1 + \frac{Lq_\xi^*}{R_a T}\Big) - \Gamma\Big(c_p + \frac{L^2 q_\xi^*}{R_v T^2}\Big) \end{aligned} \tag{4.39}$$

It follows from Equation 4.24 that the vertical change in MSE flux with height for an entraining plume is

$$\partial_z(Mh_\xi^*) = (\varepsilon h_\xi - \delta h_\xi^*)M. \tag{4.40}$$

Using the chain rule to solve for $\partial_z h_\xi^*$ (and substituting Equations 4.27, 4.37, and 4.38):

$$\begin{aligned} \partial_z h_\xi^* &= \varepsilon(h_\xi - h_\xi^*) \\ &= \varepsilon(q_\xi - q_\xi^*)L \\ &= \varepsilon(\mathrm{RH} - 1)Lq_\xi^*. \end{aligned} \tag{4.41}$$

By convention (Romps, 2016; Seeley & Wordsworth, 2023), the "bulk-plume parameter" is defined:

$$a = \mathrm{PE}\frac{\varepsilon}{\gamma}. \tag{4.42}$$

We will assume that M, RH, and α are all constant with height. Note that the assumption of constant M will be used in both the zero-buoyancy model and the two-layer heat engine model. By these assumptions, $\varepsilon = \delta$ (Equation 4.27), $\varepsilon \propto \gamma$ (Equation 4.35), and a is constant with height. Equation 4.42 can be re-arranged to solve for ε, while RH (Equation 4.35) and c_z (Equation 4.36) simplify to

$$\varepsilon = \frac{\gamma a}{\mathrm{PE}}, \tag{4.43}$$

$$RH = \frac{1 + a - \mathrm{PE}}{1 + a}, \text{ and} \tag{4.44}$$

$$c_z = \frac{\gamma q_\xi^*}{1 + a}. \tag{4.45}$$

Substituting Equations 4.43 and 4.44 into Equation 4.41,

$$\partial_z h_\xi^* = -\frac{a}{1 + a}\gamma L q_\xi^*. \tag{4.46}$$

Equating Equations 4.39 and 4.46 and solving for Γ,

$$\Gamma = \frac{g}{c_p}\Big[\frac{1 + a + q_\xi^* L/(R_a T)}{1 + a + q_\xi^* L^2/(c_p R_v T^2)}\Big]. \tag{4.47}$$

Equation 4.47 is the temperature lapse rate set by entraining convection. In a real atmosphere ($\xi = 1$), Equation 4.47 reduces to Equation (18) in Seeley & Wordsworth (2023). Once again neglecting virtual effects, we quantify the atmospheric instability in steady-state as

$$\mathrm{CAPE} = \int_{z_s}^{z_{trp}} g\frac{T' - T}{T} dz, \tag{4.48}$$

where T is the environmental temperature and T' is the temperature of a parcel lifted moist pseudo-adiabatically from the surface (z_s) to the tropopause (z_{trp}). We obtain T' and T by integrating the analytical model with $a = 0$ and $a \geq 0$, respectively. PE and a are prescribed constants; by Equation 4.43, their ratio is a constant equal to γ/ε (γ and ε both increase with

height but do so in lock-step). a controls the dilution of convective plumes by environmental air (for an extended discussion, see Seeley & Wordsworth, 2023). For undiluted convection ($a = 0$) in a real atmosphere ($\xi = 1$), Γ equals the moist pseudo-adiabatic lapse rate, Γ_m. As a increases, the tighter coupling between the plume and the environment forces Γ apart from Γ_m, permitting more CAPE in steady-state. Following R16, we assume an invariant tropopause temperature of 200 K as surface temperatures are varied, as may be suggested by the fixed anvil temperature hypothesis (Hartmann & Larson, 2002). Note that when $\xi \neq 1$, the anvil temperature does not remain fixed and, in fact, decreases with increasing ξ (e.g., see Figure 3d from Spaulding-Astudillo & Mitchell, 2023a); however, our main results are not sensitive to the choice of tropopause temperature, so for simplicity we retain the aforementioned value of 200 K even when $\xi \neq 1$.

Finally, the release of latent energy per unit mass of an undiluted (i.e., pseudo-moist adiabatic) plume traveling from the surface to the tropopause is

$$\langle r \rangle = L\Big(q_\xi^*(T_s) - q_\xi^*(T_{trp})\Big). \tag{4.49}$$

$$\approx Lq_\xi^*(T_s) \tag{4.50}$$

Equation 4.49 clearly relates the moisture lost by a saturated plume during ascent, $q_\xi^*(T_s) - q_\xi^*(T_{trp})$ to the latent heat, L.

To summarize, the system of equations for a convecting RCE atmosphere under the zero-buoyancy approximation are q_ξ^*, γ, RH, Γ, $\langle r \rangle$, and CAPE. The final forms of the equations assume that the convective mass flux, the relative humidity of the environment, and precipitation efficiency (PE - defined as the fraction of condensates generated in updrafts at each height that are not re-evaporated) are constant with height. The thermodynamic constants and their units and values are given in Table 4.1 and are also assumed to be constant with height. q_ξ^* is saturation specific humidity ($kg_{h2o}\text{kg}^{-1}$), γ is the water vapor lapse rate ($\text{kg}_{h2o}\text{kg}^{-1}\text{m}^{-1}$), RH is the relative humidity, and Γ is the temperature lapse rate (Km^{-1}). Since $\langle r \rangle$ and CAPE share the same physical units (J kg^{-1}), we are equipped

mathematically to compare their magnitudes in steady-state as a function of SST in Section 4.4.2.1. The sensitivity of CAPE and $\langle r \rangle$ to ξ allow us to test the mechanism for the emergence of RO states in Section 4.4.4.

4.4.2.1 Why CAPE and $\langle r \rangle$ diverge with increasing temperature

How are CAPE and $\langle r \rangle$ related physically? CAPE (Equation 4.48) is proportional to the height-integrated temperature difference between an undiluted lifted parcel and its environment, ΔT, which can be approximated following R16 as

$$\text{CAPE} \propto \int_{z_s}^{z_{trp}} \Delta T dz \approx \int_{z_s}^{z_{trp}} \frac{\Delta h_\xi^*}{\beta} dz. \tag{4.51}$$

Δh_ξ^* is the saturated moist static energy (MSE) difference between the two air masses at height z and $\beta = c_{p,d} + L^2 q_\xi^* / (R_v T^2)$ is the atmospheric heat capacity at height z. β^{-1} gives the fraction of the saturated MSE difference that is expressed as a temperature anomaly or, equivalently, as CAPE. Δh_ξ^* can also be expressed as (R16)

$$\Delta h_\xi^* = \frac{a}{1+a} L \Big(q_\xi^*(z_s) - q_\xi^*(z) \Big). \tag{4.52}$$

This allows us to rewrite $\langle r \rangle$ (Equation 4.49) as

$$\langle r \rangle = \frac{1+a}{a} \Delta h_\xi^*(z_{trp}). \tag{4.53}$$

The ratio $(1+a)/a$ (a constant in this restricted model of RCE, but in practice varies in real atmospheres) is the fraction of the saturated MSE difference at a given height that is expressed as $\langle r \rangle$. Given Equations 4.51 and 4.53, it's clear that CAPE and $\langle r \rangle$ are both closely related to Δh_ξ^*.[3] At lower SSTs, both $\langle r \rangle$ and CAPE grow in proportion to q_ξ^* by Equation 4.52. Unlike $\langle r \rangle$, however, CAPE peaks at intermediate SSTs because of its dependence

[3]Technically, CAPE and $\langle r \rangle$ in our steady-state model are related to the saturated MSE difference subject to the assumption of zero buoyancy and entrainment/detrainment with a dilute atmosphere. The fact that these conditions are met in observations of the tropics and CRMs (Singh & O'Gorman, 2013) lends credence to the simple model of RCE.

on $1/\beta$, which decreases rapidly at high SSTs. CAPE begins this decrease with increasing SSTs where $\beta > 2c_{p,d}$ at the tropopause (see Figure 9 from R16), or in other words where the effective heat capacity of the *entire* troposphere becomes moisture-dominated. Thus, the magnitude of CAPE is set by a competition between the increase in Δh_ξ^* and decrease in $1/\beta$, the latter of which wins out in the warmest and/or wettest environments (Figure 4.6) . Further increasing the SST beyond the peak in CAPE result in a smaller fraction of Δh_ξ^* that is expressed as CAPE through ΔT and a constant fraction and therefore growing amount of Δh_ξ^* that is expressed as $\langle r \rangle$. Any SSTs for which $\eta \langle r \rangle \neq$ CAPE violate the equilibrium assumption of the heat engine model of convection that we derived in Section 4.4.1, inevitably pushing convection from the QE state into the RO state.

4.4.3 The breakdown of convective quasi-equilibrium

As we showed in Section 4.4.1.1, a condition of statistical equilibrium in the heat engine model of EB96 is that (latent) heat is converted into work (CAPE) at an efficiency η (Equation 4.17). We use a zero-buoyancy theory of convection (Section 4.4.2; Romps, 2016) to constrain these parameters as a function of temperature and/or moisture and look for a breakdown in quasi-equilibrium, i.e. $M \neq M_{sc}$.

Note that $M \propto 1/CAPE$ (Equation 4.13) and $M_{sc} \propto 1/\Delta h$ (Equation 4.16). Invoking the zero-buoyancy approximation of convection, $\Delta h \equiv L_v \Delta q \approx \langle r \rangle$, which can increase without bound as the temperature (or moisture) increases. This implies M_{sc} decreases monotonically with T_s (Figure 4.5b). However, the same zero buoyancy approximation predicts a peak in $CAPE$ at intermediate T_s, implying a lower bound on M but no upper bound (Figure 4.5b). Clearly, the two mass fluxes diverge at high surface temperatures (Figure 4.5b). We take this to mean that radiative-convective equilibrium cannot exist in this regime.

In Section 4.4.4, we test the theory that RO emergence is related to the divergence of CAPE and $\langle r \rangle$ with increasing temperature and/or moisture content. In order to do so, we require an estimate for the efficiency of the convective heat engine on Earth and Titan. In

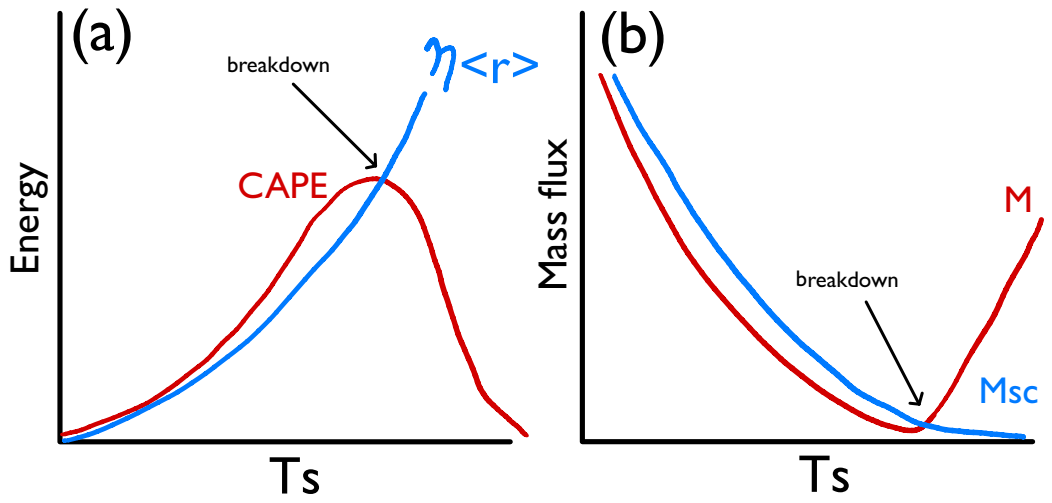

Figure 4.5: (a) Comparison of convective available potential energy (CAPE; Jkg^{-1}) and net energy released per unit mass of convecting atmosphere ($\langle r \rangle$; Jkg^{-1}) times the heat engine efficiency η as a function of surface temperature. (b) Comparison of $M \propto 1/CAPE$ and $M_{sc} \propto 1/\langle r \rangle$ as a function of surface temperature. The breakdown of the heat engine model of convection is predicted by $M \neq M_{sc}$ (black arrow).

the heat engine model,

$$\eta = -\overline{T}_{irr}\Big(\frac{1}{T_s} - \frac{1}{\overline{T}_{rad}}\Big) \tag{4.54}$$

where $\overline{T}_{irr}$ is the average temperature at which the irreversible dissipation of convective turbulence occurs, T_s is the surface temperature at which solar radiation is absorbed, and $\overline{T}_{rad}$ is the effective planetary emission temperature. We shall assume that most of the convective turbulence occurs between the surface and the radiating level such that $\overline{T}_{irr} = 0.5(T_s + \overline{T}_{rad})$. The effective emission temperature is 255 K on Earth (Pierrehumbert, 2010) and 79 K on Titan (Mitchell & Lora, 2016). For the relevant range of surface temperatures between modern Earth and the "hothouse Earth" of 290-360 K, $\eta \approx 0.25$. Similarly, over the expected range of surface temperatures on modern Titan of 90-94 K, $\eta \approx 0.15$. In what follows, we use η (Equation 4.54) to evaluate the combined zero-buoyancy, heat engine model of convection on Earth and Titan.

4.4.4 Testing the emergence mechanism for RO states

We first specify two external parameters for the zero-buoyancy model which are assumed to be constant with height: PE and a. PE is the fraction of condensates generated in ascending plumes that are re-evaporated in the environment. a quantifies the dilution of plumes by the environment, and represents the combined effect of entrainment and re-evaporation. The quantity PE/a may be estimated as the water vapor lapse rate, γ, divided by the convective entrainment rate, ε, over the troposphere. Typical values of ε and γ^{-1} in Earth's atmosphere at 300 K are $0.5 - 2 \times 10^{-3}$ km^{-1} (Romps, 2010) and 2-8 km (R16). Taking intermediate values gives an expected value for Earth of PE/$a = 0.25$. Plugging PE $= 0.25a$ into Equation 4.44 gives RH on Earth as a function of the bulk-plume parameter a only:

$$RH = \frac{1 + 0.75a}{1 + a} \tag{4.55}$$

Equation 4.55 tells us that the environmental relative humidity decreases as the bulk-plume parameter a increases. Figure 4.6a shows theoretical profiles of CAPE and $\eta\langle r\rangle$ evaluated

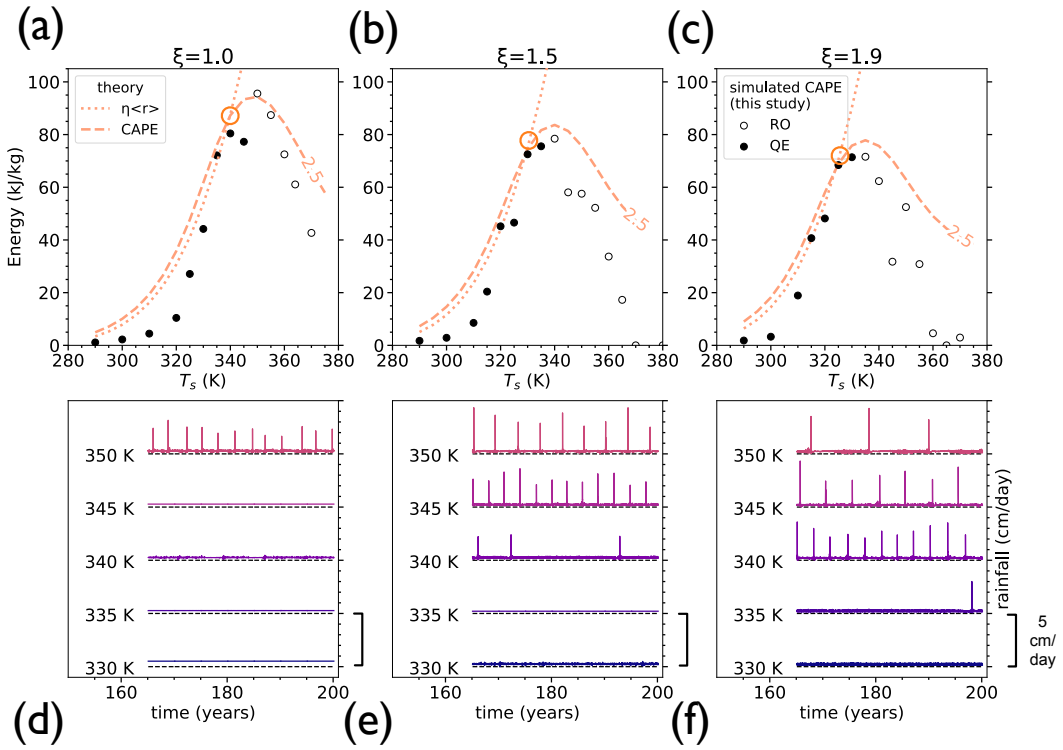

Figure 4.6: Comparison of zero-buoyancy heat engine theory and 1D-RCE simulations for Earth-like atmosphere with (a,d) $\xi = 1$, (b,e) $\xi = 1.5$, and (c,f) $\xi = 1.9$. (a-c) Analytical CAPE (dashed) and $\eta\langle r\rangle$ (dotted) with PE/a=0.25 and $a = 2.5$, as denoted by in-line labels. An open circle is placed at the theoritcal location of the QE-to-RO transition, i.e., where the dotted and dashed lines intersect. CAPE from our 1D-RCE simulations is given as black circles. Filled circles denote QE states and open circles denote RO states. (d-f) Time series of rainfall rate over a 30 year period for 1D-RCE simulations with fixed SSTs between 330-350 K. The profile from each simulation is vertically offset by 5 cm/day and a zero rainfall contour is given for reference as a dashed black line.

with the thermodynamic constants in Table 4.1 for $a = 2.5$ (by Equation 4.55, RH=0.82), which gives the best fit with the 1D-RCE simulations.

Regardless of the convective parameter values, $\eta\langle r\rangle$ *inevitably* exceeds CAPE at some SST, as shown in Section 4.4.2.1. The SST at which this first occurs can be found by identifying the intersection of the theoretical profiles of CAPE (dashed lines) and $\eta\langle r\rangle$ (dotted lines) that possess the same value (color) of a (Figure 4.6a). In the default experiment (Figure 4.6a), CAPE and $\eta\langle r\rangle$ diverge at $\sim$ 340K, which is within 10 K of where our simulations transition to the RO state.

The convection and re-evaporation schemes in our 1D-RCE model were not designed in a way that facilitates sensitivity tests using a or PE as independent control parameters. However, we introduce a multiplier on SVP (Spaulding-Astudillo & Mitchell, 2023b) into the analytical model of R16 whereby increasing it accomplishes a similar effect as to decreasing a (this part decreases the peak CAPE) while simultaneously increasing $\langle r\rangle$. The emergence temperature in our 1D-RCE simulations dropped from 350 K to 335 K for a doubling of ξ, in agreement with the 15 K change in the zero-buoyancy model (Figures 4.6a-c). Furthermore, the zero-buoyancy model predicts a decrease in the peak CAPE *and* a shift to lower SSTs with increasing ξ, which is borne out by our numerical experiments (Figures 4.6a-c). As predicted, $\langle r\rangle$ and CAPE both grow quasi-exponentially with increasing SSTs to a peak in CAPE, beyond which the latter falls off with increasing SSTs while $\langle r\rangle$ continues to grow. Thus, we find that our hypothesis that the emergence of RO states is sensitive to moisture concentration is supported by the quantitative agreement between the zero-buoyancy model prediction and numerical sensitivity experiments with varying SVP.

4.5 Discussion

We conclude that relaxation-oscillator (RO) convection is an emergent phenomenon in sufficiently warm and/or wet atmospheres. We obtained this result in a 1D-RCE model with

parameterized convection that clearly reproduces the RO states that develop in 3D-RCE with resolved convection (SW21). Switching off the radiative effects of water vapor in 1D-RCE, we demonstrated that lower-tropospheric radiative heating is non-essential for RO convection. Since RO states are clearly non-steady, we hypothesized that RO states should emerge in conditions where the energetics of moist convection violate steady-state quasi-equilibrium (QE) in a heat engine model of convection (EB96). QE is violated when the heat released by moist convection ($\langle r \rangle$) at an efficiency η is not in balance with the work performed by the heat engine (CAPE) in steady-state. That the RO mode of convection is preferred in these conditions is supported by two lines of evidence. First, the surface temperature of RO emergence in 1D- and 3D-RCE agrees with the prediction from an zero-buoyancy model evaluated with Earth-like convective parameters. Second, doubling the SVP of water at all temperatures ($\xi = 2$) causes the surface temperature of emergence to decrease by 15 K in 1D-RCE, once again in agreement with the zero-buoyancy model prediction. The agreement is reassuring, as the bulk plume equations of convection of the zero-buoyancy model are based on the parameterized convection scheme in our 1D-RCE model (see Methods). The consistency of the QE-to-RO convective regime transition across the modeling hierarchy explored here lends confidence to the robustness of this transition, and the insights gained from the simpler end of the modeling hierarchy developed here illustrates their power in the exploration of the sensitivity of these states to model parameters rooted in the physical world.

We note three reported commonalities between this and other studies of oscillatory radiative-convective states in both nitrogen- and hydrogen-rich atmospheres (e.g., SW21 and Sugiyama et al., 2014): (1) the slow erosion of a stable layer during the quiescent, storm-free period (SCP) followed by the descent of the cloud base (TP), (2) a significant temporal delay between the development of global tropospheric instability (TP) and the start of the next storm (RCP), and (3) an abrupt end to each storm when CAPE drops to zero (e.g., Figure 4.2d). We speculate that (2) and (3) could be explained by the requirement

that CAPE build well above its expected steady-state value in order to accommodate the energy released by deep convection, as represented by $\eta\langle r\rangle$. CAPE builds in time until it reaches values near $\eta\langle r\rangle$, at which point all of the CAPE would be converted to heat in a short period of time, and the CAPE would begin building again by the slower process of radiative cooling. In this sense and in analogy to an RO electric circuit, radiative cooling and virga act as the voltage source, CAPE acts as the capacitor, and $\eta\langle r\rangle$ acts as the threshold device.

There are at least two major differences between simulated RO states in our single column model and those in a 3D-CRM (SW21). The first difference is the SST above which RO states emerge, which is 30 K higher in this study than in SW21. This difference may be related to different model assumptions about the details of convective mixing and re-evaporation, and we demonstrated a case in which altering the SVP of water gave rise to 15 K differences in the SST of RO onset. Another possibility is that the efficiency of the convective heat engine in parameterized 1D-RCE is larger than in their convection-resolving model, which more carefully accounts for the irreversible entropy production in the atmosphere. A more detailed inter-comparison of these models is needed to reconcile the difference in emergence temperatures. The second difference is the recurrence interval (RI), or the typical duration of the quiescent period. In SW21, the RI is $O(1)$ day and here $O(100)$-$O(1000)$ days.[4] Of course, the time-dependent behavior of the RO state is beyond the scope of our steady-state theory, and the simulations are telling us that the RO regime is where convection is non-steady. We might better understand the relevant time scales, peak precipitation rates, etc. of the RO state by deriving linearized non-steady forms of the bulk-plume equations that appear in Section 4.4.2. These timescales, for instance, could then be compared to historical observations of giant storms on solar system planets. We leave this to future work.

In our derivation of the R16 model, we made several approximations and omissions

[4]We suspect this discrepancy is due to a model assumption of the convective parameterization that allows converted precipitation to "leak" from the updraft base near the surface and bypass re-evaporation.

(virtual effects being one of them) that introduce error in the limit of a moisture-dominated atmosphere. Revisiting these assumptions is a necessary next step, but is beyond the scope of this paper. Consistent with a recent study (Seeley & Wordsworth, 2023), the CAPE in our numerical simulations peaks at intermediate SSTs and falls to zero in the limits of a dry atmosphere or a moisture-dominated atmosphere. In Section 4.4.2.1, we discussed the "shape of CAPE", i.e., how the magnitude of CAPE changes with SST in the steady-state model (R16). Including virtual effects in Equation 4.48 causes the magnitude of the CAPE from our simulations to increase at each T_s (up to 50% at the peak), but does not significantly change the location of the peak nor the qualitative shape of CAPE vs. SST (not shown). We chose to omit virtual effects in the CAPE calculation because it allows us to directly compare our simulations to the zero-buoyancy model.

4.6 RO convection on Titan

While present-day Earth does not exhibit RO behavior, it is clear that episodic storms of potentially great magnitude occur on present-day Titan (Schneider et al., 2012; Turtle et al., 2011b; Faulk et al., 2017; Rafkin et al., 2022; Charnay et al., 2015; Mitchell & Lora, 2016). A plausible assumption is that the physics of moist convection should be similar on Titan and Earth. Given what we know about Titan, is RO-like moist (methane) convection predicted by the zero-buoyancy heat engine theory at Titan-like conditions (see Table 4.1)? Our theory of RO emergence requires the input parameters of our analytical model, which are difficult to estimate from the data, but insights can be gained by making reasonable estimates. We estimate the mean methane scale height from Equation 4.23, $\gamma^{-1} \approx 20$ km, which aligns with an earlier estimate (Lemmon et al., 2002). Following Griffith et al. (2000), we use an entrainment rate of $\varepsilon = 0.1$ km^{-1}. Centering our search around the expected PE/a value of 0.5 and $\eta \approx 0.15$ (Section 4.4.3), we look for analytical solutions for RCE on Titan (Figure 4.7a). The analytical model predicts that CAPE $< \eta\langle r \rangle$ at the present

day surface temperature of Titan of 90-95 K. This prediction is consistent with evidence of RO dynamics on Titan today. Indeed, global aquaplanet simulations of Titan by Faulk et al. (2020) with the Titan Atmospheric Model (Lora et al., 2015) depicted in Figure 4.7b resemble the 1D (Figure 4.1d) and 3D (see Figure 1 from SW21) simulated RO states on Earth, where brief periods of intense rainfall give way to extended periods of little to no rain. The largest deluges are capable of driving fluvial erosion and sediment transport, and influence the distribution of alluvial fans on Titan's surface (Faulk et al., 2017; Lewis-Merrill et al., 2022). Interestingly, the theory indicates that a transition from RO to QE dynamics would occur on Titan if it were 5-10 K cooler. A simple test of our theory for RO emergence would be to lower the surface temperature in a Titan GCM and look for this RO-to-QE transition.[5]

The example of Titan highlights the many potential applications of our theory for RO states. For instance, intermittent storms could be examined as a driver of surface morphological evolution on different planets in the solar system that have or may once have had active volatile cycles. The heat engine perspective of convection offers a robust point of comparison between the atmospheres of Earth and Titan based on the first and second laws of thermodynamics, which are system invariant. The heat engine model, in fact, is agnostic of the composition of the working fluid and is, arguably, the best framework to explain why dynamical similarities - the precipitation rate prominent among them - between the hothouse Earth and Titan exist. Further tests are needed to confirm our zero-buoyancy heat engine theory of convection. The advantage of our theory is that it is (1) general to any moist planetary atmosphere and (2) agnostic of the condensing component, and because of this generality, it will find wide application across the solar system and beyond.

Titan's episodic storms indicate RO-type convection, which may reflect the fact that

[5]Lowering Titan's temperature by 5-10 K would cause nitrogen to condense in much of the upper troposphere, which would need to be suppressed within the Titan climate model that tests our hypothesis.

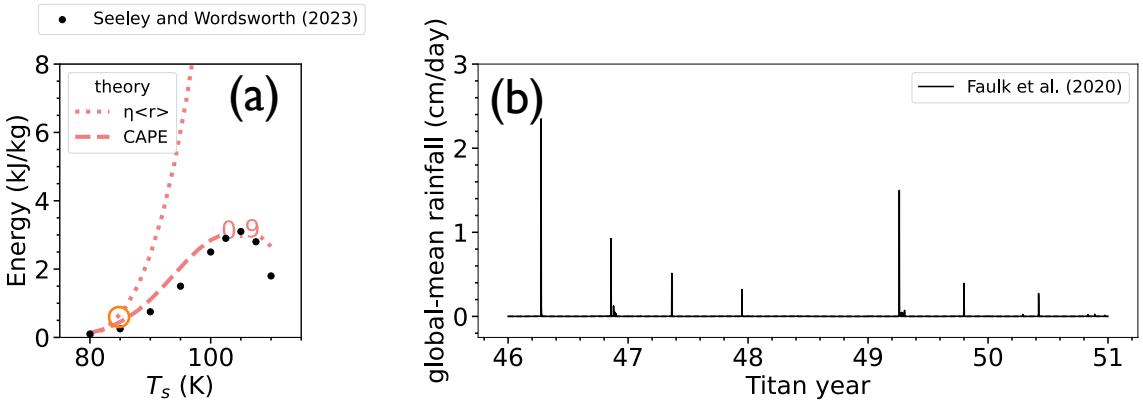

Figure 4.7: Comparison of zero-buoyancy heat engine theory and cloud-resolving model simulations from Seeley & Wordsworth (2023) for Titan-like atmosphere. (a) Theoretical CAPE (dashed) and $\eta\langle r\rangle$ (dotted) with PE/a=0.5 and $a = 0.9$, as denoted by in-line labels. An open circle is placed at the theoritcal location of the QE-to-RO transition, i.e., where the dotted and dashed lines intersect. CAPE from the Titan simulations of Seeley & Wordsworth (2023) is given as black circles. (b) Time series of global-mean rainfall rate in cm per Earth day over a period of 5 Titan years for TAM (Lora et al., 2015) aquaplanet simulations from Faulk et al. (2020).

methane volatility[6] on Titan greatly exceeds water volatility on Earth today. Our exploration with the water volatility parameter, ξ, suggests the underlying cause of the QE-to-RO state transition is the amount of water vapor rather than the surface temperature, and the latter may just be a proxy for the former (Figure 4.6). But what is it about water volatility (abundance) that causes this transition? The behavior of CAPE, $\langle r \rangle$, and the onset of the RO state are closely related to the parameter β, which is an effective heat capacity that takes into account how SVP shifts with changes in temperature. The thermodynamic quantities that β is comprised of – c_p, R_v, L, and q^* – are easily estimated for any conceivable atmospheric composition with a condensable gas. It seems that with these few thermodynamic ingredients, it might be possible to erect a very general regime diagram in β and the other convective parameters that could be used to classify all planetary atmospheres. Such a regime diagram could be tested (perhaps even calibrated) against moist convection throughout the solar system. If found to be predictive of the occurrence of QE- and RO-style convection, this convective regime diagram could be used to predict essentially any atmosphere one could concoct, and then tested against time-varying signals of moist convection on exoplanets that will soon be resolved by the James Webb Space Telescope. In taking this comparative approach, modifications to the analytical model may be required to generate solutions for atmospheres where the non-condensable background air is lighter than the condensable gases, which introduces competing latent and molecular weight effects on convection. We are carrying out this generalization in ongoing work.

[6]Volatility is here defined as the SVP of a condensable at typical surface conditions of a particular planet.

CHAPTER 5

Conclusions

The results of three studies have been presented, which address the questions posed in the Introduction (Chapter 1). In Chapter 2, we asked: How does the abundance of moisture in the atmosphere influence climate, clouds, and convection? This question was motivated by a side-by-side comparison of Earth and Saturn's moon Titan, which are similar in their atmospheric composition and hydrological cycles and yet their atmospheric dynamics and weather patterns are distinct. We speculated that the major differences in climate, clouds, and convection are attributable to the abundance of precipitable moisture in their atmospheres. We developed four testable hypotheses regarding the variation in cloud properties with varying moisture. Then, we ran a one-dimensional climate model in an Earth-like setup and tested the hypotheses by multiplying the saturation vapor pressure of water vapor within the climate model by a constant parameter ξ. There are several major takeaways from our investigation. The first is that high anvil clouds form at a fixed vapor pressure path (VPP). VPP is a vertical integral of the partial pressure of water vapor and its utility originates from basic principles of atmospheric radiative transfer. We followed up on our finding in Chapter 3, and showed that the tops of tropical congestus clouds also form at a fixed VPP. This demonstrated that our finding is robust at multiple levels of Earth's atmosphere, and could be applied in other planetary contexts. Another key takeaway from Chapter 2 is that the number of cloud layers in Earth's atmosphere is sensitive to moisture abundance. In vapor-poor atmospheres, the convective boundary layer expands until the entire troposphere is turbulently mixed by dry eddies. Under normal conditions, moist convection produces a "C"-shaped distribution of relative humidity, which leads to cloud formation at lower and

upper levels of the troposphere. In the driest conditions, mixing by boundary layer eddies homogenizes the tropospheric relative humidity, producing a single cloud layer. In the climatological average, high latitude clouds on Earth are also single-peaked (Figure 1.1b) between the surface and the tropopause. We speculate that the results of our vapor-poor simulations could be used to better understand the single peakedness of cloud fraction at high latitudes on Earth. In vapor-rich atmospheres, we found that the convective boundary layer inevitably drops below the lifting-condensation level (LCL). The implications are that low clouds cannot persist when their supply of surface moisture is cut off. It may be worthwhile considering the effects of moisture abundance on boundary layer and LCL height on Titan, where clouds at low levels are less common than those at middle and upper levels (Griffith et al., 2000) and, in general, the top of the boundary layer is below the LCL height of 3 km (Mitchell & Lora, 2016; Charnay & Lebonnois, 2012). The last takeaway is that the largest changes in climate, clouds, and convection occur at climate tipping points (Balaji et al., 2022), rather than in the stable "in-betweens". Earth's climate (referring here to surface temperature, cloud fraction, and relative humidity) was surprisingly resilient to changes in moisture abundance in the stable "in-betweens". In the Earth-like states with two-layer (low and high) clouds, we observed that changes to the radiative properties of clouds from increasing the moisture content offset the changes to the water vapor greenhouse effect, resulting in fixed surface temperatures across a wide range of water vapor concentrations. In the future, we intend to study the climate invariance to moisture concentration in cloud-resolving model simulations.

In Chapter 3, we asked: Why do tropical congestus clouds on Earth terminate at a height of 5-6 km? Our question was motivated by two key considerations. First, the driving mechanism is still debated in the scientific literature (e.g., Zuidema, 1998; Redelsperger et al., 2002; Mechem & Oberthaler, 2013). Second, it is well known that most climate models do not accurately represent this major cloud population (Miao et al., 2019). In fact, the ECHAM6 SCM used in Chapter 2 does not produce mid-level clouds likely because of

its reliance on a cloud parameterization that assumes a positive correlation between relative humidity and the diagnosed cloud fraction. Contrary to what is observed in nature, the dryness of the mid-troposphere produces a minimum in cloud fraction in the ECHAM6 SCM. Starting from basic assumptions of mass and energy conservation, we derived a clear-sky theory of cloud formation that has often been used in the Earth climate literature (e.g., Hartmann & Larson, 2002). In this "clear-sky convergence" (CSC) theory (e.g., Seeley et al., 2019b), decreases in clear-sky radiative cooling with height are linked to the formation of spreading cloud anvils through convective detrainment. We evaluated the CSC theory in different scenarios with a clear-sky radiative transfer model, and found that there is a strong peak in convective detrainment at 5-6 km due to the frequency dependence of strong absorption lines in the water vapor rotation band. Therefore, the first takeaway of Chapter 3 is that the tropical peak in mid-level cloud fraction (Figure 1.1b) is due to the spectroscopic properties of water vapor. The second takeaway is that climate model predictions of mid-level cloud fraction could be improved by taking into account the positive correlation between clear-sky convergence and cloudiness. Our simulations demonstrate that drier mid-tropospheric conditions should actually enhance congestus cloud tops at 5-6 km, consistent with observations and numerical simulations (e.g., Brown & Zhang, 1997; Sokol & Hartmann, 2022). The broader knowledge that we contribute in Chapter 3, therefore, is a radiative-convective mechanism of congestus cloud top formation. It is worth pointing out that the CSC theory correctly predicts the height at which tropical clouds form in the mid- and upper-troposphere. Given the apparent generality of the CSC theory, there is no reason to think that it could not applied at low levels to understand the formation height of boundary layer clouds, such as marine stratocumulus. We are carrying out this generalization of the CSC theory to low clouds in ongoing work.

In Chapter 4, we asked: Why do Earth and Titan have distinct patterns of precipitation? This question was motivated by an inter-comparison of the global-mean precipitation on Earth and Titan (Figure 1.2), which revealed that convective activity is steady on Earth

and non-steady on Titan. For this reason, we designate the state of Earth's present day climate as a quasi-equilibrium (QE; Emanuel, 2008) and that of Titan's present climate as a relaxation oscillator (RO) due to the bursty precipitation associated with Titan's semi-periodic storms. It was recently discovered that the Earth enters an RO state known as the "hothouse Earth" at sufficiently high surface temperatures (Seeley & Wordsworth, 2021). The dynamic similarity between the hothouse Earth and Titan points to a general, underlying physical mechanism that is agnostic of, for example, the atmospheric composition. Despite many quantitative differences, the climates of Earth and Titan share an important quality: the presence of a thermodynamically- and radiatively-important condensing atmospheric constituent. This condensable is, of course, water on Earth and methane on Titan. We hypothesized that the climates of present-day Earth and Titan are primarily differentiated by the quantity of condensable in their atmospheres, which is naturally a function of the surface temperature of a planet. Since RO states are, by definition, non-steady, we further hypothesized that the conditions leading to a breakdown of quasi-equilibrium must be predictive of the surface temperature and/or moisture content at which the QE-to-RO transition occurs. To test our hypotheses, we derived a zero-buoyancy heat engine theory of convection (Emanuel & Bister, 1996; Romps, 2016). The zero-buoyancy approximation allowed us to quantify the convective available potential energy (CAPE) and condensational heat released by convective motions ($\langle r \rangle$) in steady-state equilibrium. In the heat engine theory of convection, we derived an "equilibrium condition" from the requirement of no net vertical transport of mass in equilibrium, which states that the heat engine does work equal to CAPE in the process of transferring heat $\langle r \rangle$ from the warm surface to the cold upper atmosphere at an efficiency η. Importantly, $\langle r \rangle$ quantifies the latent energy that is released through condensation by the convective motions. It was then shown that CAPE and $\langle r \rangle$ inevitably diverge at high surface temperature and/or moisture content. This divergence implies a violation of the equilibrium condition. The advantage of the heat engine perspective of convection is that it offers a robust point of comparison between the atmospheres of Earth

and Titan based on the first and second laws of thermodynamics, which are system invariant. The heat engine model, in fact, is agnostic of the condensing substance in the working fluid and is, arguably, the best framework to explain why dynamical similarities - the precipitation rate prominent among them - between the hothouse Earth and Titan exist. The first takeaway of Chapter 4 is that a breakdown of quasi-equilibrium implied by the divergence of CAPE and $\eta\langle r\rangle$ is indeed predictive of the QE-to-RO transition on Earth. Furthermore, we find that our theory predicts RO behavior on present day Titan, consistent with simulation and observation. A general rule of RO states is that *the latent heat released by convective motions must exceed the work done by the convective heat engine.* The existence of QE dynamics on Earth and RO dynamics on Titan and on the hothouse Earth is consistent with this rule. On Titan, it would seem that the relatively slow process of radiative cooling builds CAPE that is then released all at once in a large convective event. The event is short lived because convection releases the potential energy stored in the atmosphere rapidly. CAPE then takes a long time to build up again to reach the threshold for another massive storm. In this picture, Earth represents a planetary environment in which convective heating and radiative cooling are nearly in balance at all times. This balance is well documented in the tropics over large spatial and temporal scales (Jakob et al., 2019), but becomes a worse approximation with increasing latitude (Miyawaki et al., 2022). Further comparison of Earth and Titan observations and simulations is needed to confirm this picture, but it appears to be a promising direction for further study.

The success of the Earth-to-Titan comparison suggests that we can extend these ideas about climate, clouds, and convection in several directions. We are especially interested in extending the CSC theory to methane clouds on Titan. This would, of course, require a in-depth analysis of the spectroscopic properties of nitrogen, methane, and hydrogen, which are all important greenhouse gases on Titan, and perhaps also the global haze layer, which is opaque at solar wavelengths and transparent at infrared wavelengths (McKay et al., 1991). Heights of cloud formation on the gas giants present another possible avenue of future ex-

ploration with the CSC theory. There, moist convection is inhibited by the high molecular weight of condensables relative to the light background gases of hydrogen and helium. Despite this complexity, appropriate statements of mass and energy conservation might be derived for such atmospheres. Descending through Jupiter's atmosphere, for instance, one encounters first ammonia clouds at 0.4 bar, then ammonium hydrosulfide clouds at 1.5 bar, and then water clouds at 3 bar (Young et al., 2019). One wonders what parallels, if any, exist between the trimodal nature of convection in Earth's tropics (Johnson et al., 1999) and the trimodality of Jupiter's cloud decks. Indeed, the examples of Titan and Jupiter remind us that much remains to be discovered about the physics of cloud formation across the solar system. To that point, a number of interesting open questions and potential applications of the CSC and zero-buoyancy heat engine (ZBHE) theories of convection spring to mind. The ZBHE perspective holds promise as a simple litmus test for steady vs. non-steady convective dynamics. We speculate that the ZBHE theory could inform our understanding of the past, present, and future climates of the solar system planets. In particular, the ZBHE theory predicts steady precipitation on past Titan if the surface was sufficiently cooler than the present day due to a dimmer sun (Tokano, 2017). Finding evidence in a Titan climate model of a transition from bursty to steady precipitation in colder conditions would reform our thinking about Titan's distant past. On present day Titan, large episodic deluges drive sedimentary erosion, producing surface features such as river channels and alluvial fans (Hörst, 2017; Faulk et al., 2017). One wonders how QE- vs. RO-type precipitation influence surface features over time, and the extent to which these features might be preserved and/or observed today on any number of solar system bodies. Along this vein, no general theory for the mean precipitation rate exists outside of the present day Earth tropics (Jeevanjee et al., 2017). It is therefore unclear how mean precipitation changes as a function of surface temperature and/or atmospheric moisture content. What impact might the change in convective dynamics at the QE-to-RO transition have on mean precipitation and/or precipitation intensity? Finally, we still lack a general theory for cloud radiative effects (CRE) on Earth. It is clear

that low clouds cool and high clouds warm the surface (Yuan & Oreopoulos, 2013), relative to a cloudless atmosphere, so where does the inflection point occur? Starting with a gray cloud model embedded in a clear column of atmosphere, it might be possible to derive a simple expression for CRE from the basic equations of radiative transfer. The free parameters of such a model would be the cloud height and the cloud opacity (as a function of condensate density). Since the amount of condensation is constrained by the clear-sky cooling rate, it is conceivable that the cloud opacity could be expressed in terms of the spectroscopic properties of the clear-sky greenhouse gases. This would reduce the number of number of free parameters to the cloud height alone, which we have already shown is constrained by the CSC theory. Recall that a mean theory of precipitation is simply the vertical integral of net condensation, whereas the cloud opacity is related to the vertically-resolved net condensation, which is constrained by the cooling rate of the troposphere. We speculate therefore that CRE might be derived entirely from the spectroscopic properties of the greenhouse gases in clear-sky regions. The theoretical CRE could then be compared to the observed CRE in Earth's tropics. A simple model of CRE could be used to draw insight about how clouds at any level respond to increasing temperature and/or carbon dioxide concentrations in the near future. The variation in CRE from the poles to the equator could be examined in this context as well. It is well known, for example, that clouds in the tropics are net cooling whereas at high latitudes they are net warming (Cotton et al., 2011). The prospect of a unified theory governing mean precipitation, cloud height, and CRE on Earth, all rooted in clear-sky spectroscopy, is a compelling one. If such a theory could be formulated, it might serve to refine the physical algorithms within climate models and aid in anticipating the global impacts of climate change.

Bibliography

Abbot, D. S. 2014, Journal of Climate, 27, 4391 , doi: https://doi.org/10.1175/JCLI-D-13-00738.1

Abbot, D. S., Voigt, A., Branson, M., et al. 2012, Geophysical Research Letters, 39, doi: https://doi.org/10.1029/2012GL052861

Abbot, D. S., Voigt, A., Li, D., et al. 2013, Journal of Geophysical Research Atmospheres, 118, 6017, doi: 10.1002/jgrd.50540

Albrecht, B., Ghate, V., Mohrmann, J., et al. 2019, Bulletin of the American Meteorological Society, 100, 93, doi: 10.1175/BAMS-D-17-0180.1

Arakawa, A., & Schubert, W. H. 1974, Journal of Atmospheric Sciences, 31, 674 , doi: https://doi.org/10.1175/1520-0469(1974)031<0674:IOACCE>2.0.CO;2

Arya, S. P. 1988in , 157–181, doi: 10.1016/S0074-6142(08)60426-X

Balaji, V., Couvreux, F., Deshayes, J., et al. 2022, Proceedings of the National Academy of Sciences, 119, e2202075119, doi: 10.1073/pnas.2202075119

Battalio, J. M., Lora, J. M., Rafkin, S., & Soto, A. 2022, Icarus, 373, 114623, doi: 10.1016/j.icarus.2021.114623

Bertrand, W., Kay, J. E., Haynes, J., & de Boer, G. 2023, Earth System Science Data Discussions, 2023, 1, doi: 10.5194/essd-2023-265

Beydoun, H., Caldwell, P. M., Hannah, W. M., & Donahue, A. S. 2021, Geophysical Research Letters, 48, e2021GL094049, doi: https://doi.org/10.1029/2021GL094049

Bodas-Salcedo, A., Webb, M. J., Brooks, M. E., et al. 2008, Journal of Geophysical Research: Atmospheres, 113, doi: https://doi.org/10.1029/2007JD009620

Bourgeois, Q., Ekman, A. M. L., Igel, M. R., & Ringer, M. A. 2016, Nature Communications, 7, doi: https://doi.org/10.1038/ncomms12432

Bretherton, C. S., Blossey, P. N., & Jones, C. R. 2013, Journal of Advances in Modeling Earth Systems, 5, 316, doi: https://doi.org/10.1002/jame.20019

Bretherton, C. S., & Wyant, M. C. 1997, Journal of the Atmospheric Sciences, 54, 148, doi: 10.1175/1520-0469(1997)054<0148:MTLTSA>2.0.CO;2

Brown, M. E., Bouchez, A. H., & Griffith, C. A. 2002, Nature, 420, 795, doi: 10.1038/nature01302

Brown, R. G., & Zhang, C. 1997, Journal of the Atmospheric Sciences, 54, 2760 , doi: https://doi.org/10.1175/1520-0469(1997)054<2760:VOMMAI>2.0.CO;2

Caballero, R., & Huber, M. 2010, Geophysical Research Letters, 37, doi: https://doi.org/10.1029/2010GL043468

Ceppi, P., & Nowack, P. 2021, Proceedings of the National Academy of Sciences, 118, e2026290118, doi: 10.1073/pnas.2026290118

Cesana, G., Del Genio, A. D., & Chepfer, H. 2019, Earth System Science Data, 11, 1745, doi: 10.5194/essd-11-1745-2019

Charnay, B., Barth, E., Rafkin, S., et al. 2015, Nature Geoscience, 8, 362, doi: 10.1038/ngeo2406

Charnay, B., & Lebonnois, S. 2012, Nature Geoscience, 5, 106, doi: 10.1038/ngeo1374

Christensen, H. M., Dawson, A., & Holloway, C. E. 2018, Journal of Advances in Modeling Earth Systems, 10, 1833, doi: https://doi.org/10.1029/2017MS001189

Colaprete, A., & Toon, O. B. 2003, Journal of Geophysical Research: Planets, 108, doi: https://doi.org/10.1029/2002JE001967

Cotton, W. R., Bryan, G., & van den Heever, S. C. 2011, in International Geophysics, Vol. 99, Storm and Cloud Dynamics, ed. W. Cotton, G. Bryan, & S. van den Heever (Academic Press), 527–672, doi: https://doi.org/10.1016/S0074-6142(10)09916-X

Coustenis, A., & Raulin, F. 2011, Titan, ed. M. Gargaud, R. Amils, J. C. Quintanilla, H. J. J. Cleaves, W. M. Irvine, D. L. Pinti, & M. Viso (Berlin, Heidelberg: Springer Berlin Heidelberg), 1676–1689, doi: 10.1007/978-3-642-11274-4_1594

Cuijpers, J. W. M., & Bechtold, P. 1995, Journal of the Atmospheric Sciences, 52, 2486

Cuijpers, J. W. M., & Duynkerke, P. G. 1993, Journal of Atmospheric Sciences, 50, 3894, doi: 10.1175/1520-0469(1993)050<3894:LESOTW>2.0.CO;2

Deardorff, J. W. 1972, Monthly Weather Review, 100, 93, doi: 10.1175/1520-0493(1972)100<0093:POTPBL>2.3.CO;2

Dhingra, R. D., Barnes, J. W., Brown, R. H., et al. 2019, Geophysical Research Letters, 46, 1205, doi: https://doi.org/10.1029/2018GL080943

Driedonks, A. G. M., & Tennekes, H. 1984, Boundary-Layer Meteorology, 30, 75, doi: 10.1007/BF00121950

Dudhia, A. 2017, Journal of Quantitative Spectroscopy and Radiative Transfer, 186, 243, doi: https://doi.org/10.1016/j.jqsrt.2016.06.018

Edwards, D. P. 1992, University Corporation for Atmospheric Research, (No. NCAR/TN-367+STR), doi: 10.5065/D6W37T86

Emanuel, K. 2008, Chapter 7 Quasi-Equilibrium Dynamics of the Tropical Atmosphere, ed. T. Schneider & A. H. Sobel (Princeton: Princeton University Press), 186–218, doi: doi:10.1515/9780691236919-009

Emanuel, K. A., & Bister, M. 1996, Journal of Atmospheric Sciences, 53, 3276 , doi: https://doi.org/10.1175/1520-0469(1996)053<3276:MCVABS>2.0.CO;2

Eyring, V., Bony, S., Meehl, G. A., et al. 2016, Geoscientific Model Development, 9, 1937, doi: 10.5194/gmd-9-1937-2016

Faulk, S. P., Lora, J. M., Mitchell, J. L., & Milly, P. C. D. 2020, Nature Astronomy, 4, 390, doi: 10.1038/s41550-019-0963-0

Faulk, S. P., Mitchell, J. L., Moon, S., & Lora, J. M. 2017, Nature Geoscience, 10, 827, doi: 10.1038/ngeo3043

Fischer, G., Kurth, W. S., Gurnett, D. A., et al. 2011, Nature, 475, 75, doi: 10.1038/nature10205

Frierson, D. M. W., Held, I. M., & Zurita-Gotor, P. 2006, Journal of the Atmospheric Sciences, 63, 2548, doi: 10.1175/JAS3753.1

—. 2007, Journal of the Atmospheric Sciences, 64, 1680, doi: 10.1175/JAS3913.1

Gelaro, R., McCarty, W., Suárez, M. J., et al. 2017, Journal of Climate, 30, 5419, doi: 10.1175/JCLI-D-16-0758.1

Gettelman, A., Truesdale, J. E., Bacmeister, J. T., et al. 2019, Journal of Advances in Modeling Earth Systems, 11, 1381, doi: https://doi.org/10.1029/2018MS001578

Giorgetta, M., Roeckner, E., Mauritsen, T., & Rast, S. 2013, Berichte zur Erdsystemforschung / Max-Planck-Institut für Meteorologie, 135

Gordon, I., Rothman, L., Hargreaves, R., et al. 2022, Journal of Quantitative Spectroscopy and Radiative Transfer, 277, 107949, doi: https://doi.org/10.1016/j.jqsrt.2021.107949

Griffith, C. A., Hall, J. L., & Geballe, T. R. 2000, Science, 290, 509, doi: 10.1126/science.290.5491.509

Griffith, C. A., McKay, C. P., & Ferri, F. 2008, The Astrophysical Journal, 687, L41, doi: 10.1086/593117

Griffith, C. A., Owen, T., Geballe, T. R., Rayner, J., & Rannou, P. 2003, Science, 300, 628, doi: 10.1126/science.1081897

Griffith, C. A., Owen, T., Miller, G. A., & Geballe, T. 1998, Nature, 395, 575, doi: https://doi.org/10.1038/26920

Grundner, A., Beucler, T., Gentine, P., et al. 2022, Journal of Advances in Modeling Earth Systems, 14, e2021MS002959, doi: https://doi.org/10.1029/2021MS002959

Guichard, F., & Couvreux, F. 2017, Tellus A: Dynamic Meteorology and Oceanography, 69, 1373578, doi: 10.1080/16000870.2017.1373578

Harrop, B. E., & Hartmann, D. L. 2012, Journal of Climate, 25, 5731, doi: 10.1175/JCLI-D-11-00445.1

Hartmann, D. L. 2016a, in Global Physical Climatology (Second Edition), second edition edn. (Boston: Elsevier), 131–157, 293–323, doi: https://doi.org/10.1016/B978-0-12-328531-7.00005-0

—. 2016b, Global Physical Climatology (Elsevier), 325–360, doi: 10.1016/C2009-0-00030-0

Hartmann, D. L., Dygert, B. D., Blossey, P. N., Fu, Q., & Sokol, A. B. 2022, Journal of Climate, 35, 6253 , doi: https://doi.org/10.1175/JCLI-D-21-0861.1

Hartmann, D. L., Gasparini, B., Berry, S. E., & Blossey, P. N. 2018, Journal of Advances in Modeling Earth Systems, 10, 3012, doi: https://doi.org/10.1029/2018MS001484

Hartmann, D. L., & Larson, K. 2002, Geophysical Research Letters, 29, 12, doi: 10.1029/2002GL015835

Hayes, A. G. 2016, Annual Review of Earth and Planetary Sciences, 44, 57, doi: 10.1146/annurev-earth-060115-012247

Held, I. M., & Soden, B. J. 2000, Annual Review of Energy and the Environment, 25, 441, doi: 10.1146/annurev.energy.25.1.441

—. 2006, Journal of Climate, 19, 5686 , doi: https://doi.org/10.1175/JCLI3990.1

Hörst, S. M. 2017, Journal of Geophysical Research: Planets, 122, 432, doi: https://doi.org/10.1002/2016JE005240

Iacono, M. J., Delamere, J. S., Mlawer, E. J., et al. 2008, Journal of Geophysical Research: Atmospheres, 113, doi: 10.1029/2008JD009944

Jakob, C., Singh, M. S., & Jungandreas, L. 2019, Journal of Geophysical Research: Atmospheres, 124, 5418, doi: https://doi.org/10.1029/2018JD030092

Jeevanjee, N., & Fueglistaler, S. 2020a, Journal of the Atmospheric Sciences, 77, 479 , doi: https://doi.org/10.1175/JAS-D-18-0347.1

—. 2020b, Journal of the Atmospheric Sciences, 77, 465 , doi: https://doi.org/10.1175/JAS-D-18-0352.1

Jeevanjee, N., Hassanzadeh, P., Hill, S., & Sheshadri, A. 2017, Journal of Advances in Modeling Earth Systems, 9, 1760, doi: https://doi.org/10.1002/2017MS001038

Jeevanjee, N., & Zhou, L. 2022, Journal of Advances in Modeling Earth Systems, 14, e2021MS002759, doi: https://doi.org/10.1029/2021MS002759

Jensen, M. P., & Genio, A. D. D. 2006, Journal of Climate, 19, 2105 , doi: https://doi.org/10.1175/JCLI3722.1

Johnson, R. H., Ciesielski, P. E., & Hart, K. A. 1996, Journal of Atmospheric Sciences, 53, 1838 , doi: https://doi.org/10.1175/1520-0469(1996)053<1838:TINTL>2.0.CO;2

Johnson, R. H., Rickenbach, T. M., Rutledge, S. A., Ciesielski, P. E., & Schubert, W. H. 1999, Journal of Climate, 12, 2397 , doi: https://doi.org/10.1175/1520-0442(1999)012<2397:TCOTC>2.0.CO;2

Kajishima, T., & Taira, K. 2017, Computational Fluid Dynamics (Springer International Publishing), doi: 10.1007/978-3-319-45304-0

Kay, J. E., & Gettelman, A. 2009, Journal of Geophysical Research: Atmospheres, 114, doi: https://doi.org/10.1029/2009JD011773

King, M. D., Platnick, S., Menzel, W. P., Ackerman, S. A., & Hubanks, P. A. 2013, IEEE Transactions on Geoscience and Remote Sensing, 51, 3826, doi: 10.1109/TGRS.2012.2227333

Kite, E. S., Steele, L. J., Mischna, M. A., & Richardson, M. I. 2021, Proceedings of the National Academy of Sciences, 118, e2101959118, doi: 10.1073/pnas.2101959118

Koll, D. D. B., & Cronin, T. W. 2018, Proceedings of the National Academy of Sciences, 115, 10293, doi: 10.1073/pnas.1809868115

Kuang, Z., & Hartmann, D. L. 2007, Journal of Climate, 20, 2051 , doi: https://doi.org/10.1175/JCLI4124.1

Kumar, V. V., Protat, A., Jakob, C., & May, P. T. 2014, Journal of the Atmospheric Sciences, 71, 1105 , doi: https://doi.org/10.1175/JAS-D-13-0231.1

Lambert, F. H., Challenor, P. G., Lewis, N. T., et al. 2020, Journal of Advances in Modeling Earth Systems, 12, e2020MS002085, doi: https://doi.org/10.1029/2020MS002085

Lang, T., Naumann, A. K., Stevens, B., & Buehler, S. A. 2021, Journal of Advances in Modeling Earth Systems, 13, e2021MS002514, doi: https://doi.org/10.1029/2021MS002514

Leconte, J., Forget, F., Charnay, B., Wordsworth, R., & Pottier, A. 2013, Nature, 504, 268, doi: 10.1038/nature12827

Lemmon, M. T., Smith, P. H., & Lorenz, R. D. 2002, Icarus, 160, 375, doi: 10.1006/icar.2002.6979

Lewis-Merrill, R. A., Moon, S., Mitchell, J. L., & Lora, J. M. 2022, The Planetary Science Journal, 3, 223, doi: 10.3847/PSJ/ac8d09

Li, C., & Ingersoll, A. P. 2015, Nature Geoscience, 8, 398, doi: 10.1038/ngeo2405

Li, Y., Yang, P., North, G. R., & Dessler, A. 2012, Journal of the Atmospheric Sciences, 69, 2317 , doi: https://doi.org/10.1175/JAS-D-11-0158.1

Lin, J., Qian, T., Bechtold, P., et al. 2022, Atmosphere-Ocean, 60, 422, doi: 10.1080/07055900.2022.2082915

Lora, J. M., Lunine, J. I., & Russell, J. L. 2015, Icarus, 250, 516, doi: 10.1016/j.icarus.2014.12.030

Lorenz, R. D. 2005, Geophysical Research Letters, 32, L01201, doi: 10.1029/2004GL021415

Malkus, J. S., & Riehl, H. 1964, Tellus, 16, 275, doi: https://doi.org/10.1111/j.2153-3490.1964.tb00167.x

Mauritsen, T., Stevens, B., Roeckner, E., et al. 2012, Journal of Advances in Modeling Earth Systems, 4, doi: https://doi.org/10.1029/2012MS000154

McKay, C. P., Pollack, J. B., & Courtin, R. 1991, Science, 253, 1118, doi: 10.1126/science.11538492

McKinney, M. M., Mitchell, J., & Thomson, S. I. 2022, Journal of the Atmospheric Sciences, 79, 2813 , doi: 10.1175/JAS-D-21-0295.1

Mechem, D. B., & Oberthaler, A. J. 2013, Journal of Advances in Modeling Earth Systems, 5, 623, doi: https://doi.org/10.1002/jame.20043

Meehl, G. A., Senior, C. A., Eyring, V., et al. 2020, Science Advances, 6, eaba1981, doi: 10.1126/sciadv.aba1981

Miao, H., Wang, X., Liu, Y., & Wu, G. 2019, Atmospheric Science Letters, 20, e906, doi: https://doi.org/10.1002/asl.906

Mitchell, J. L., Ádámkovics, M., Caballero, R., & Turtle, E. P. 2011, Nature Geoscience, 4, 589, doi: https://doi.org/10.1038/ngeo1219

Mitchell, J. L., & Lora, J. M. 2016, Annual Review of Earth and Planetary Sciences, 44, 353, doi: 10.1146/annurev-earth-060115-012428

Mitchell, J. L., Pierrehumbert, R. T., Frierson, D. M. W., & Caballero, R. 2006, Proceedings of the National Academy of Sciences, 103, 18421, doi: 10.1073/pnas.0605074103

Miyawaki, O., Shaw, T. A., & Jansen, M. F. 2022, Journal of Climate, 35, 1045 , doi: https://doi.org/10.1175/JCLI-D-21-0440.1

Mlawer, E. J., Payne, V. H., Payne, V. H., et al. 2012, Philos Trans A Math Phys Eng Sci, 370, 2520, doi: 10.1098/rsta.2011.0295

Möbis, B., & Stevens, B. 2012, Journal of Advances in Modeling Earth Systems, 4, 1, doi: 10.1029/2012MS000199

Moran, S. E., Hörst, S. M., Batalha, N. E., Lewis, N. K., & Wakeford, H. R. 2018, The Astronomical Journal, 156, 252, doi: 10.3847/1538-3881/aae83a

Neggers, R., Stevens, B., & Neelin, J. D. 2006, Theoretical and Computational Fluid Dynamics, 20, 305, doi: 10.1007/s00162-006-0030-1

Neggers, R. A. J., Stevens, B., & Neelin, J. D. 2007, Quarterly Journal of the Royal Meteorological Society, 133, 1629, doi: https://doi.org/10.1002/qj.105

Nuijens, L., & Emanuel, K. 2018, Quarterly Journal of the Royal Meteorological Society, 144, 2676, doi: https://doi.org/10.1002/qj.3385

O'Gorman, P. A., Allan, R. P., Byrne, M. P., & Previdi, M. 2012, Surveys in Geophysics, 33, 585, doi: 10.1007/s10712-011-9159-6

Pederson, D. O., & Mayaram, K. 2008, Relaxation and Voltage-Controlled Oscillators (Boston, MA: Springer US), 377–416, doi: 10.1007/978-0-387-68030-9_12

Pierrehumbert, R. T. 2010, Principles of Planetary Climate (Cambridge University Press), doi: 10.1017/CBO9780511780783

Pierrehumbert, R. T., & Ding, F. 2016, Proceedings of the Royal Society A: Mathematical, Physical and Engineering Sciences, 472, doi: 10.1098/rspa.2016.0107

Popp, M., Schmidt, H., & Marotzke, J. 2015, Journal of the Atmospheric Sciences, 72, 452, doi: 10.1175/JAS-D-13-047.1

—. 2016, Nature Communications, 7, 10627, doi: 10.1038/ncomms10627

Porco, C. C., Baker, E., Barbara, J., Beurle, K., et al. 2005, Nature, 438, 159, doi: 10.1038/nature03436

Rafkin, S. C., Lora, J. M., Soto, A., & Battalio, J. M. 2022, Icarus, 373, 114755, doi: 10.1016/j.icarus.2021.114755

Raju, K. S., & Kumar, D. N. 2020, Journal of Water and Climate Change, 11, 577, doi: 10.2166/wcc.2020.128

Ramanathan, V., Cess, R. D., Harrison, E. F., et al. 1989, Science, 243, 57, doi: 10.1126/science.243.4887.57

Rannou, P., Montmessin, F., Hourdin, F., & Lebonnois, S. 2006, Science, 311, 201, doi: 10.1126/science.1118424

Redelsperger, J.-L., Parsons, D. B., & Guichard, F. 2002, Journal of the Atmospheric Sciences, 59, 2438 , doi: https://doi.org/10.1175/1520-0469(2002)059<2438:RPAFLC>2.0.CO;2

Rieck, M., Nuijens, L., & Stevens, B. 2012, Journal of the Atmospheric Sciences, 69, 2538, doi: 10.1175/JAS-D-11-0203.1

Roe, H. G. 2012, Annual Review of Earth and Planetary Sciences, 40, 355, doi: 10.1146/annurev-earth-040809-152548

Romps, D. M. 2010, Journal of the Atmospheric Sciences, 67, 1908 , doi: 10.1175/2010JAS3371.1

—. 2014, Journal of Climate, 27, 7432, doi: 10.1175/JCLI-D-14-00255.1

—. 2016, Journal of the Atmospheric Sciences, 73, 3719 , doi: 10.1175/JAS-D-15-0327.1

—. 2017, Journal of the Atmospheric Sciences, 74, 3891, doi: 10.1175/JAS-D-17-0102.1

Rybicki, G. B., & Lightman, A. P. 1985, FUNDAMENTALS OF RADIATIVE TRANSFER (John Wiley Sons, Ltd), 1–50, doi: https://doi.org/10.1002/9783527618170.ch1

Salathé, E. P., Leung, L. R., Qian, Y., & Zhang, Y. 2010, Climatic Change, 102, 51, doi: 10.1007/s10584-010-9849-y

Sassen, K., & Wang, Z. 2008, Geophysical Research Letters, 35, doi: https://doi.org/10.1029/2007GL032591

Sassen, K., Wang, Z., & Liu, D. 2009, Journal of Geophysical Research: Atmospheres, 114, doi: https://doi.org/10.1029/2009JD011916

Satoh, M., Stevens, B., Judt, F., et al. 2019, Current Climate Change Reports, 5, 172, doi: 10.1007/s40641-019-00131-0

Schaller, E. L., Roe, H. G., Schneider, T., & Brown, M. E. 2009, Nature, 460, 873, doi: 10.1038/nature08193

Schneider, T., Graves, S. D. B., Schaller, E. L., & Brown, M. E. 2012, Nature, 481, 58, doi: 10.1038/nature10666

Schneider, T., Kaul, C. M., & Pressel, K. G. 2019, Nature Geoscience, 12, 164, doi: 10.1038/s41561-019-0310-1

Schneider, T., Teixeira, J., Bretherton, C. S., et al. 2017, Nature Climate Change, 7, 3, doi: 10.1038/nclimate3190

Schubert, W. H., Ciesielski, P. E., Lu, C., & Johnson, R. H. 1995, Journal of the Atmospheric Sciences, 52, 2941, doi: 10.1175/1520-0469(1995)052<2941:DAOTTW>2.0.CO;2

Seeley, J. T., Jeevanjee, N., Langhans, W., & Romps, D. M. 2019a, Geophysical Research Letters, 46, 492, doi: https://doi.org/10.1029/2018GL080747

Seeley, J. T., Jeevanjee, N., & Romps, D. M. 2019b, Geophysical Research Letters, 46, 1842, doi: https://doi.org/10.1029/2018GL080096

Seeley, J. T., & Wordsworth, R. D. 2021, Nature, 599, 74, doi: 10.1038/s41586-021-03919-z

—. 2023, The Planetary Science Journal, 4, 34, doi: 10.3847/PSJ/acb0cb

Seidel, S. D., & Yang, D. 2020, Science Advances, 6, eaba1951, doi: 10.1126/sciadv.aba1951

—. 2022, Journal of Climate, 35, 8065 , doi: https://doi.org/10.1175/JCLI-D-21-0962.1

Siebesma, A. P. 1998, Shallow Cumulus Convection, ed. E. J. Plate, E. E. Fedorovich, D. X. Viegas, & J. C. Wyngaard (Dordrecht: Springer Netherlands), 441–486, doi: 10.1007/978-94-011-5058-3_19

Singh, M. S., & O'Gorman, P. A. 2013, Geophysical Research Letters, 40, 4398, doi: 10.1002/grl.50796

Singh, M. S., & O'Neill, M. E. 2022, Rev. Mod. Phys., 94, 015001, doi: 10.1103/RevModPhys.94.015001

Singh, M. S., & O'Neill, M. E. 2022, Physics Today, 75, 30, doi: 10.1063/PT.3.5038

Slingo, J. M. 1980, Quarterly Journal of the Royal Meteorological Society, 106, 747, doi: https://doi.org/10.1002/qj.49710645008

Smith, R. N. B. 1990, Quarterly Journal of the Royal Meteorological Society, 116, 435, doi: https://doi.org/10.1002/qj.49711649210

Sokol, A. B., & Hartmann, D. L. 2020, Journal of Geophysical Research: Atmospheres, 125, e2020JD033107, doi: https://doi.org/10.1029/2020JD033107

—. 2022, Journal of Advances in Modeling Earth Systems, 14, e2022MS003045, doi: https://doi.org/10.1029/2022MS003045

Somerville, R., & Iacobellis, S. 1999, Physics and Chemistry of the Earth, Part B: Hydrology, Oceans and Atmosphere, 24, 733, doi: https://doi.org/10.1016/S1464-1909(99)00074-X

Spaulding-Astudillo, F. E., & Mitchell, J. L. 2023a, Journal of the Atmospheric Sciences, doi: 10.1175/JAS-D-22-0063.1

—. 2023b, Journal of the Atmospheric Sciences, doi: 10.1175/JAS-D-22-0063.1

Stauffer, C. L., & Wing, A. A. 2022, Journal of Advances in Modeling Earth Systems, 14, e2021MS002917, doi: https://doi.org/10.1029/2021MS002917

Stevens, B. 2006, Theoretical and Computational Fluid Dynamics, 20, 279, doi: 10.1007/s00162-006-0032-z

Stevens, B., Giorgetta, M., Esch, M., et al. 2013, Journal of Advances in Modeling Earth Systems, 5, 146, doi: 10.1002/jame.20015

Stull, R. B. 1988, An Introduction to Boundary Layer Meteorology, Atmospheric and Oceanographic Sciences Library (Springer Netherlands)

Stute, M., Clement, A., & Lohmann, G. 2001, Proceedings of the National Academy of Sciences, 98, 10529, doi: 10.1073/pnas.191366098

Sugiyama, K., Nakajima, K., Odaka, M., Kuramoto, K., & Hayashi, Y.-Y. 2014, Icarus, 229, 71, doi: https://doi.org/10.1016/j.icarus.2013.10.016

Sundqvist, H. 1988, Parameterization of Condensation and Associated Clouds in Models for Weather Prediction and General Circulation Simulation, ed. M. E. Schlesinger (Dordrecht: Springer Netherlands), 433–461, doi: 10.1007/978-94-009-3041-4_10

Sundqvist, H., Berge, E., & Kristjánsson, J. E. 1989, Monthly Weather Review, 117, 1641, doi: 10.1175/1520-0493(1989)117<1641:CACPSW>2.0.CO;2

Takemi, T., Hirayama, O., & Liu, C. 2004, Geophysical Research Letters, 31, doi: https://doi.org/10.1029/2004GL020225

Tan, Z., Schneider, T., Teixeira, J., & Pressel, K. G. 2017, Journal of Advances in Modeling Earth Systems, 9, 19, doi: 10.1002/2016MS000804

Tiedtke, M. 1989, Monthly Weather Review, 117, 1779, doi: 10.1175/1520-0493(1989)117<1779:ACMFSF>2.0.CO;2

—. 1993, 121:11, doi: 10.1175/1520-0493(1993)121<3040:ROCILS>2.0.CO;2

Tokano, T. 2017, Icarus, 289, 120, doi: https://doi.org/10.1016/j.icarus.2017.02.005

Tokano, T., McKay, C. P., Neubauer, F. M., et al. 2006, Nature, 442, 432, doi: 10.1038/nature04948

Tompkins, A. 2005, The parametrization of cloud cover, ECMWF Moist Processes Lecture Note Series

Turtle, E. P., Del Genio, A. D., Barbara, J. M., et al. 2011a, Geophysical Research Letters, 38, doi: https://doi.org/10.1029/2010GL046266

Turtle, E. P., Perry, J. E., Hayes, A. G., et al. 2011b, Science, 331, 1414, doi: 10.1126/science.1201063

Wall, C., Liu, C., & Zipser, E. 2013, Journal of Geophysical Research: Atmospheres, 118, 6478, doi: https://doi.org/10.1002/jgrd.50455

Wallace, J. M., & Hobbs, P. V. 2006, in Atmospheric Science (Second Edition), second edition edn., ed. J. M. Wallace & P. V. Hobbs (San Diego: Academic Press), 25–61, doi: https://doi.org/10.1016/B978-0-12-732951-2.50007-7

Wolf, E. T., & Toon, O. B. 2015, Journal of Geophysical Research: Atmospheres, 120, 5775, doi: 10.1002/2015JD023302

Wood, R. 2012, Monthly Weather Review, 140, 2373, doi: 10.1175/MWR-D-11-00121.1

Wood, R., & Bretherton, C. S. 2006, Journal of Climate, 19, 6425, doi: 10.1175/JCLI3988.1

Wordsworth, R. D., & Pierrehumbert, R. T. 2013, Astrophysical Journal, 778, doi: 10.1088/0004-637X/778/2/154

Yang, D., & Seidel, S. D. 2020, Journal of Climate, 33, 2841 , doi: https://doi.org/10.1175/JCLI-D-19-0260.1

Young, R. M., Read, P. L., & Wang, Y. 2019, Icarus, 326, 253, doi: https://doi.org/10.1016/j.icarus.2018.12.002

Yuan, T., & Oreopoulos, L. 2013, Geophysical Research Letters, 40, 5320, doi: https://doi.org/10.1002/grl.50871

Zelinka, M. D., & Hartmann, D. L. 2010, Journal of Geophysical Research: Atmospheres, 115, doi: https://doi.org/10.1029/2010JD013817

Zuidema, P. 1998, Journal of the Atmospheric Sciences, 55, 2220 , doi: https://doi.org/10.1175/1520-0469(1998)055<2220:TMMITC>2.0.CO;2

Zuidema, P., Mapes, B., Lin, J., Fairall, C., & Wick, G. 2006, Journal of Climate, 19, 4531 , doi: https://doi.org/10.1175/JCLI3836.1